

Universidad Nacional Autónoma de México



**Doctorado en Ciencias (Astrofísica)
Instituto de Radioastronomía y Astrofísica**

PhD project updates

Environment and obscuration of the Active Galactic Nuclei

Author:

Donaji Catalina Alejandra Esparza Arredondo

Advisor:

Dra. Omaira González Martín

IRyA, UNAM

&

Dra. Deborah Dultzin Kessler

IA, UNAM



July 31, 2018

Contents

1	Introduction	1
1.1	AGN-host galaxy coevolution	2
1.1.1	Optical wavelengths	2
1.1.2	Mid-Infrared wavelengths	3
1.1.3	Background	3
1.2	AGN torus	5
1.2.1	X-ray wavelengths	5
1.2.2	Mid-infrared wavelengths	5
2	The coevolution between AGN and star-formation.	8
2.1	Current status of the project	8
2.2	Alternative project: A comparison between [SIV] and [OIII] lines through diagnostic diagrams. .	11
2.3	Working plan	12
3	The properties of the torus through simultaneous fitting of mid-IR and X-ray spectra.	13
3.1	Current status of the project	13
3.2	Working plan for next semesters	13
4	Summary and Time table	15
5	Appendix A: The properties of the torus through simultaneous setting of mid-IR and X-ray spectra.	16
6	Appendix B: Circumnuclear star-formation and AGN activity: Clues from surface brightness radial profile of PAHs and [SIV].	20
7	Appendix C: Physical parameters of the torus for the type 1.5 Seyfert NGC 3516 from the mid-infrared and X-ray simultaneous spectral fitting.	53
8	Appendix D: PhD project	62
	Bibliografía	76

Introduction

Black holes (BHs) are objects with high densities whose large gravitational field does not even let the light escape. The existence of these objects was proposed since the XVIII century by Laplace (“invisible bodies”) and it was confirmed by Einstein at the beginning of the last century. However, it was not until 1969 that they were given the name of “Black hole” for the first time. In the following years was found the observational proof of their existence have been discovered. Recently, BHs of different sizes that include large mass ranges from $3 - 30 M_{\odot}$, remains of a stellar nuclei merger in a type II supernova, and even Supermassive Black holes (SMBH) with masses of the order of $10^6 - 10^9 M_{\odot}$ and are located in the central part of galaxies have been discovered. The SMBHs that have a disc around them accreting material to it are known as “Active Galactic Nuclei” (AGN). In the local universe ($z < 0.1$), about one in 50 galaxies is host to a SMBH with efficient accretion, while one in every three has an SMBH with inefficient accretion. The energy released by AGN is in the range of $10^{38} - 10^{48}$ erg s $^{-1}$ and it emits in all wavelengths.

The study of AGNs is complex because they are compact unresolved sources (~ 1 kpc) and in many cases variable. According to the unified model [Antonucci, 1993; Urry & Padovani, 1995] the structure of these sources is the following: A SMBH with a mass of the order of $10^6 - 10^9 M_{\odot}$ in the center of the source, which is surrounded by an *accretion disc* and that is responsible for feeding it. Around this disc, we find the *broad line region (BLR)*, which is formed by several clouds with high dispersion velocities of the order of thousands of kilometers per second. Then, we find a dusty axisymmetric structure with a radii between $\sim 0.1 - 10$ pc that it is called *dusty torus*. In the external parts, the *Narrow line region (NLR)* can be found which contains ionization gas clouds with low density ($\sim 10^4$ cm $^{-3}$) and dispersion velocities of hundreds of kilometers per second. In some AGNs, we see a *jet* through which material from the central parts blowing away.

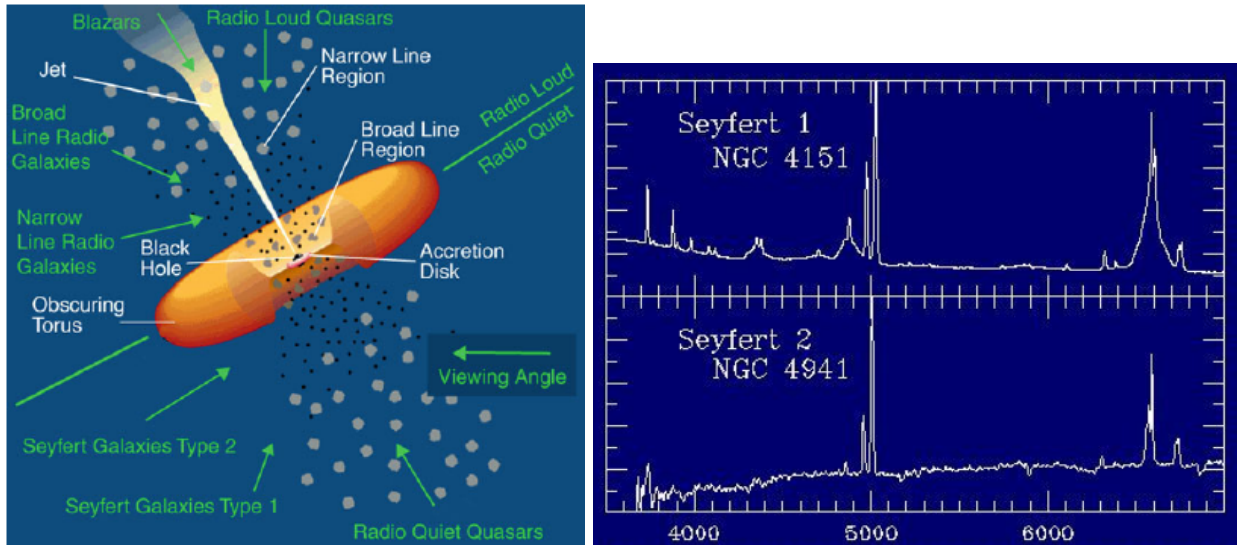


Figure 1.1: Left: Unification model presented by Urry & Padovani [1995]. The key to unification between type I and II is the existence of optically thick dust torus obscuring the inner parts for some line of sights; the BLR is blocked up by dust torus for these viewing angles, and therefore, the spectrum only shows narrow lines from the NLR (type II). Right: Spectra of the Seyfert galaxies. Credit: NASA.

According to the unified model, AGNs are the same object but the observational differences depend only on some physical parameters, such as: 1) the torus position relative to the observed line of sight observed, 2) the luminosity of the source, and 3) the presence of relativistic jets (see Figure 1.1). Nonetheless, the unification model is not capable of explaining all the observations. Other models propose a connection between different

AGNs through an evolution induced by the perturbations of the near environment due to the fall of gas to the nucleus [e.g. Krongold et al., 2003; Koulouridis, 2014]. Other authors propose that AGN components could be modified. For example, the accretion disc may not exist and it is replaced by an inefficient corona. Another case is the disappearance of the dust torus in AGNs of low luminosity, both from theoretical [e.g. Elitzur & Netzer, 2016] and observational [González-Martín et al., 2017] facts.

Currently, it is well known that there are various types of AGNs, but in this work only two types are considered:

- **Seyfert type I (Sy1):** These sources show broad permitted and semi-forbidden emission lines ($1,000 - 20,000 \text{ km s}^{-1}$). Almost all low and intermediate luminosity AGNs ($< 10^4 \text{ ergs}^{-1}$), show stronger narrow emission lines ($300 - 1,000 \text{ km s}^{-1}$) of high ionization, many of which are forbidden.
- **Seyfert type II (Sy2):** These sources only contain strong narrow forbidden emission lines ($300 - 1,000 \text{ km s}^{-1}$) in the near-IR, optical, and UV.

Among the vast number of open questions about AGN ingredients and evolution, the main aim of this thesis is to study the torus and how AGN and star-formation (SF) could co-evolve over time.

1.1 AGN-host galaxy coevolution

In the last decades, researches have found the scale relations between AGNs and host galaxies [Magorrian et al., 1998; Ferrarese & Merritt, 2000; Kormendy & Ho, 2013]. An example is the relation between SMBH mass and stellar velocity dispersion of the bulge. Various scenarios have been proposed to explain these relations. Some authors propose that the gas in the center of the galaxy is responsible for SMBH growth and the enrichment of the stellar formation [Sanders & Mirabel, 1996]. Also, it has been suggested that the quenching of SF could be related to feedback from SMBH through the accretion disc [Silk & Rees, 1998]. Numerical simulations propose a scenario where the larger-scales processes can be related to small-scale phenomena near the nucleus [Hopkins and Quataert , 2010; Netzer, 2013]. According to these studies, major mergers or tidal tails could produce perturbation which might push the material toward the center, increasing the SF and, at the same time, switching on the AGN activity. Another possibility is a scenario where the radiation field of the central source is capable of stopping the SF, imposing a balance between both [the so-called AGN feedback, e.g. Wu et al. , 2009].

1.1.1 Optical wavelengths

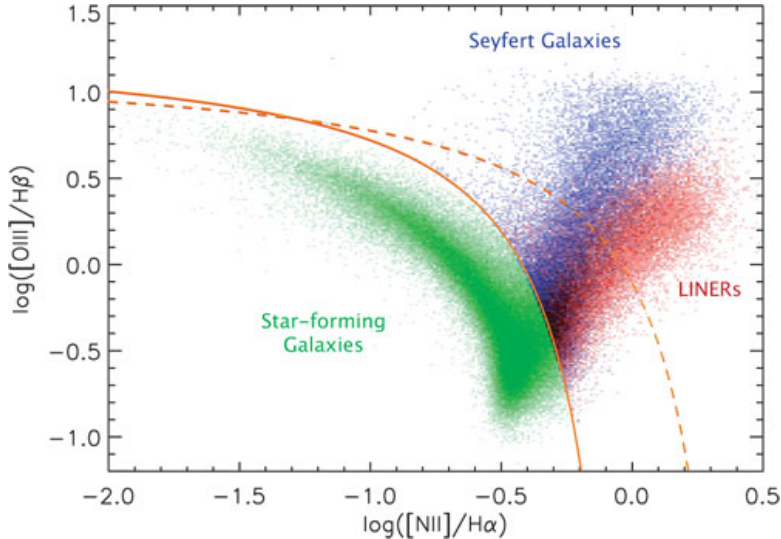


Figure 1.2: The BPT diagram used to classify the emission-line galaxies as: Seyfert, LINER, Composite and Star-forming galaxies. The curves indicate empirical (solid) and theoretical (dashed) dividing lines between active galactic nuclei (AGN) and star-forming galaxies, based upon the SDSS observations [Kauffmann et al., 2003] and MAPPINGS III photoionization models [Kewley & Dopita, 2002].

Differentiating between the SF regions and AGN photoionization is a hard task. Optical wavelengths offer a good opportunity to disentangle both using emission line diagnostic diagrams. Baldwin et al. [1981] first

proposed the diagnostic diagrams (now known as the BPT diagram, see Figure 1.2) to separate normal HII regions, planetary nebula, and AGNs. The BPT diagram most used consists in combined $[\text{NII}]6584/\text{H}_\alpha$ and $[\text{OIII}]5007/\text{H}_\beta$. The next commonly-used BPT diagnostic diagrams are $[\text{SII}]6717, 6731/\text{H}_\alpha$ versus $[\text{OIII}]5007/\text{H}_\beta$ (BPT-SII) and $[\text{OI}]6300/\text{H}_\alpha$ versus $[\text{OIII}]5007/\text{H}_\beta$ (BPT-OI). This BPT diagram has been extended and refined in diverse works through theoretical photoionization models and/or observations [e.g. Veilleux & Osterbrock, 1987; Kewley et al., 2001; Kauffmann et al., 2003; Kewley et al., 2006, 2013]. The theoretical photoionization models explore the shape of the classification line between SF and AGN galaxies.

1.1.2 Mid-Infrared wavelengths

The infrared wavelengths are also good tools to study SF in the close proximity of the AGN. The advantage of using SF tracers, in this range, is that they are not contaminated by AGN emission. We will study good traces of the SF in the proximity of the AGN radiation field, to use them to understand the plausible coevolution between AGNs and their host galaxies.

In the mid-IR wavelengths, we can analyze emission lines which are produced by different components of AGNs and/or nuclear SF in the host galaxy. Particularly, we can observe the emission of the Polycyclic Aromatic Hydrocarbons (PAHs) that trace SF [e.g. Peeters et al., 2004; Esquej et al., 2014]. The PAHs are molecules in space that contain 20-100 carbon and hydrogen atoms, which are heated at high temperatures due to younger B stars [Peeters et al., 2004]. The PAHs emission has been observed in the nuclear region close to the AGN [González-Martín et al., 2013; Alonso-Herrero et al., 2014]. Diamond-Stanic et al. [2010] found a strong correlation between nuclear SF at scales of kilo-parsecs using the $11.3\mu\text{m}$ PAH and $24\mu\text{m}$ continuum emission in Seyfert galaxies. Other authors have found that PAHs emission is weak or lacking in Sy1 [e.g. Mason et al., 2007]. This lack of PAHs could be related to the destruction of the molecules responsible of their emission by the radiation field of the AGN.

These works are based on a comparison of nuclear and circumnuclear SF, using the nuclear spectrum of ground-based telescopes (i.e., with the best spatial resolution available) and the circumnuclear spectra from satellites [i.e., with low spatial resolution, e.g. Esquej et al., 2014]. Only, some studies do a detailed analysis of circumnuclear emission using different radial apertures centered in the AGN [e.g. Alonso-Herrero et al., 2014].

At the same range of wavelengths, we can study the $[\text{SIV}]$ line emission at $10.5\mu\text{m}$. This line arises from ions with an ionization potential of 35 eV. It has been observed in different objects, such as planetary nebulae, HII galactic regions, and ULIRGS [Rank et al., 1970; Holtz et al., 1971; Gillett et al., 1972]. In the case of AGNs, the origin of this line is controversial. Some works suggest that this line is produced in the SF regions and/or NLR [Pereira-Santalla et al., 2010; Groves et al., 2008].

1.1.3 Background

In Esparza-Arredondo et al. [2018] (see Appendix B), we explored the relationship between circumnuclear SF and AGN activity. For this we used a sample of 19 local AGNs with high resolution spectra using T-ReCS (Gemini) and CanariCam (GTC), together with IRS (*Spitzer*) observations. We measured the flux and EW for $11.3\mu\text{m}$ PAH feature and the $[\text{SIV}]$ emission line at different distances from the nucleus. We found that the $[\text{SIV}]$ line could be used to trace the AGN radiation field within a few thousand times the sublimation radius (R_{subl}), but it often peaks at distances greater than $1000 R_{\text{subl}}$. One possibility is that the SF is contributing to the $[\text{SIV}]$ total flux. For the $11.3\mu\text{m}$ PAH emission, we found a deficit within the inner few tens of parsecs from the AGN. This deficit might be due to the destruction of the molecules responsible for this feature or the lack of SF at these distances. We found a sensible agreement in the expected shift of the relation of the AGN bolometric luminosity and the star-formation rate (SFR). This indicates that numerical models attributing the link between AGN activity and host galaxy growth to mergers are in agreement with our data.

Objectives

This part of the thesis follows our previous study about the coevolution between SF and nuclear activity, which is based on the analyses of long slit spectra. In this work, we propose to explore the SF regions and nuclear photoionization using high spatial resolution images and models at different wavelengths.

- **The radiation field of AGN.** In our previous work [Esparza-Arredondo et al., 2018], we found that the [SIV] line emission could be used as a tracer of AGN photoionization within a few thousand times the sublimation radius, but it is contaminated by SF at distances greater than 1000 sublimation radius. Our goal is to study the behavior of the [SIV] line together with other nuclear photoionization tracers (e.g., [O_{III}] and soft X-ray).
- **Star-formation in the environment of the AGN.** In our previous work [Esparza-Arredondo et al., 2018], we studied a relation between AGN and circumnuclear SFR through the 11.3 μm PAH emission. However, we cannot clarify if PAHs are good tracers near of the AGN ($< 50\text{ pc}$). Therefore, our goal is to explore the 11.3 μm PAH emission in the presence of an AGN together with other SF tracers (e.g. H _{α} and UV) at scales less than 100 pc.

1.2 AGN torus

In the mid-IR and X-ray we can find the best clues about the dust torus.

1.2.1 X-ray wavelengths

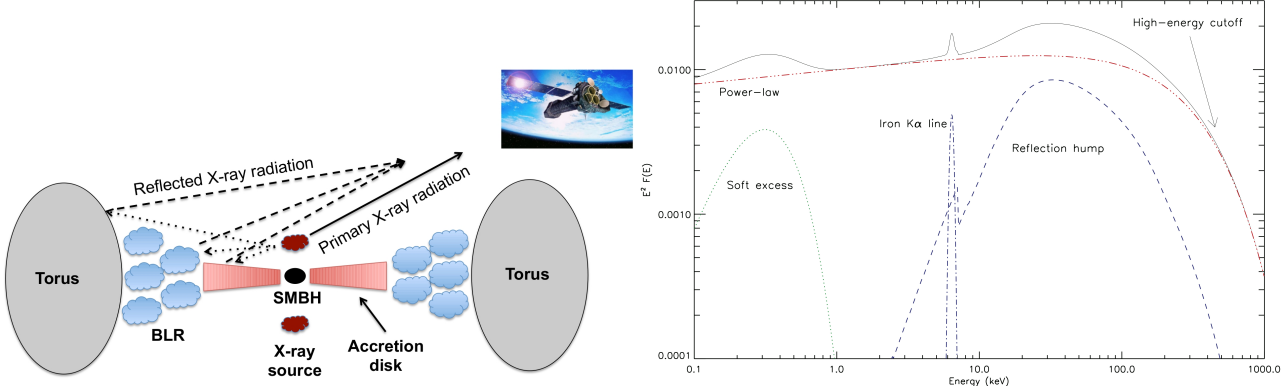


Figure 1.3: Left: Schematic representation of X-ray emission in AGN from website: http://www.isdc.unige.ch/~ricci/Website/AGN_in_the_X-ray_band.html. Right: Spectrum of the unabsorbed AGN from Ricci et al. 2011, PhD thesis.

The majority of the X-ray emission in AGN is produced by a corona of a plasma of hot electrons close to the accretion disk that scatters the energy due to inverse Compton (primary X-ray radiation). This Comptonization produces one of three main components of X-ray spectra which is known as the intrinsic continuum. This component is modeled through a power-law with a photon index (Γ) and it dominates the spectral emission above 2 keV. This emission is a function of the high energy cutoff [Haardt & Maraschi, 1991; Marinucci et al., 2015]. One part of this emission is reprocessed by the inner parts (accretion disk, BLR, and/or dust torus) to produce the two other components that depend on the density of material: 1) The Compton hump that peaks at 30 keV and 2) the iron K α emission line at 6.4 keV (Fe K α , see Figure 1.3). The Compton hump depends on the geometry of the reflecting medium (covering factor of the torus, Cf, and the average column density, NH) and chemical composition of the reflector [Ghisellini et al., 1994]. The shape of Fe K α line depends on its origin: 1) if it is produced in the surface of the accretion disc, the line is broad, while 2) if the origin is the cold gas in the torus then the line is narrow. Where the X-ray continuum is unobscured the equivalent width (EW) of Fe K α narrow line depend on the number of photons absorbed. Therefore, the EW of this feature is a clear signal of the torus in AGNs [Guainazzi et al., 2005]. In obscuring sources large EW are expected, because most of the radiation of the intrinsic continuum is blocked by obscuring clouds [Ghisellini et al., 1994].

Therefore, the X-ray reflected emission is a good tool for the diagnostic of the torus properties [Bassani et al., 1999; Panessa et al., 2006; González-Martín et al., 2009]. Currently, there are different models whose objective is to reproduce the X-ray reprocessing spectrum from a torus-shape medium, such as: Mytorus [Murphy & Yaqoob, 2009], etorus [Ikeda et al., 2009], BNtorus [Brightman & Nandra, 2011], and cotorus [Liu & Li, 2015]. These models use a Monte-Carlo method to derive approximations to green functions for a toroidal reprocessor. The main difference between them is the geometry of the torus considered and the treatment of different components [Brightman et al., 2015]. This work uses a recent model proposed by Baloković et al. [2018] which uses a grid of X-ray spectral templates (borus02, see Figure 1.4) based on a radiative transfer code BORUS (M. Baloković et al. 2018 in preparation). The advantage of this model is that it is capable of constraining geometric parameters of the torus: the average column density (NH), view angle (i), and half opening angle. These parameters can be compared directly with mid-IR models (see below).

1.2.2 Mid-infrared wavelengths

The continuum emission at mid-IR is dominated by the heating of dust due to the AGN [Prieto et al., 2001]. Therefore, we can study the properties of the toroidal dust of AGNs through modeling this continuum with radiative transfer codes [Nenkova et al., 2008a; Höning, 2008; Ramos Almeida et al., 2009, 2014]. The dust torus has been the subject of several kinds of models at mid-infrared wavelengths that aimed to extract physical properties from SED and, in some cases, interferometric observations. We can divide them into four kinds: smooth [Fritz et al., 2006; Feltre et al., 2012], clumpy [Nenkova et al., 2008a,b; Höning et al., 2010; Höning &

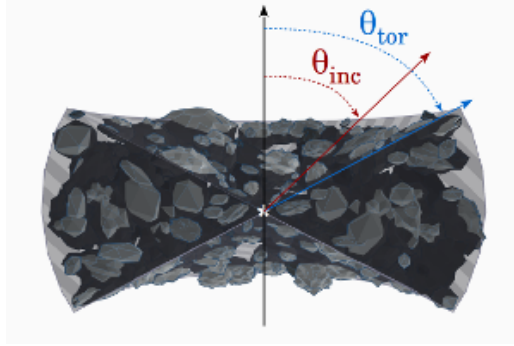


Figure 1.4: Cross-section of the approximately toroidal geometry adopted by boros02. Figure from Baloković et al. [2018].

Kishimoto, 2010], smooth + clumpy [Stalevski et al., 2012; Siebenmorgen et al., 2015], and windy [Hönig & Kishimoto, 2017]. Among them the most extensively used one is the Clumpy model by Nenkova et al. [2008b] due to their large number of SEDs and probed ability to explain the mid-infrared emission of low luminosity [González-Martín et al., 2017], intermediate luminosity [Ramos Almeida et al., 2009], and high luminosity [Martínez-Paredes et al., 2017] AGNs. It is a radiative transfer code that models the AGN clumpy dust torus emission¹ [see Figure 1.5 Nenkova et al., 2008a,b], developed based on those proposed by Nenkova et al. [2002]; Elitzur et al. [2004]; Elitzur & Shlosman [2006]. They developed a formalism that takes proper account of the concentration of dust in clumps or clouds, referred to as clumpy, nature of the AGN torus. The models assume a clumpy nature of the dusty torus (i.e. not homogeneous) whose parameters are the inclination angle (θ_{inc}), the number of clouds in the equatorial plane of the torus (N_0), the width of the angular distribution (σ), the relation between inner and outer radius ($Y = R_{\text{out}}/R_{\text{in}}$), index for a power law (q), and the optical depth of each cloud (τ). This models include 1,247,400 SEDs in the 0.001-1,000 μm wavelength range. These models are capable of explaining some observed features in the IR spectra of AGNs as the observed behavior of the 10 μm silicate feature in any type.

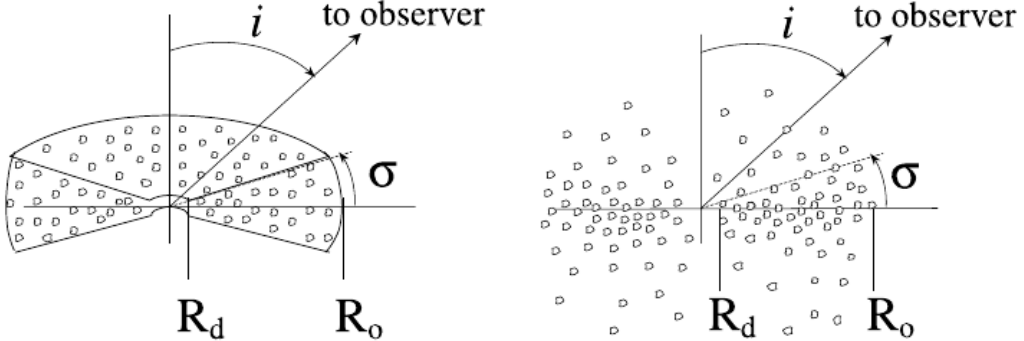


Figure 1.5: CLUMPY torus model. Dust clouds, each with an optical depth τ_ν , occupy a toroidal volume from inner radius R_d , determined by dust sublimation, to outer radius $R_o = YR_d$. The radial distribution is a power law r^{-q} , and the total number of clouds along a radial equatorial ray is N_0 . The parameter σ is the width for various angular distributions. Figure from Nenkova et al. [2008a].

¹All data are available on the website: <https://www.clumpy.org/>

Objective

In previous works, torus models using radiative transfer to estimate the mid-IR properties [Nenkova et al., 2008a; Höning & Kishimoto, 2010] and X-ray [e.g. mytorus^a Murphy & Yaqoob, 2009] have been presented. However, the parameters have not been properly estimated using only either mid-infrared or X-ray spectra. Our goal is to properly estimate the torus parameter using simultaneously mid-infrared and X-ray spectra of AGN. This will allow us to study if the toroidal properties change with the kind of AGN activity (e.g. bolometric luminosity, accretion rate, or BH mass).

^a<http://mytorus.com/>

The coevolution between AGN and star-formation.

2.1 Current status of the project

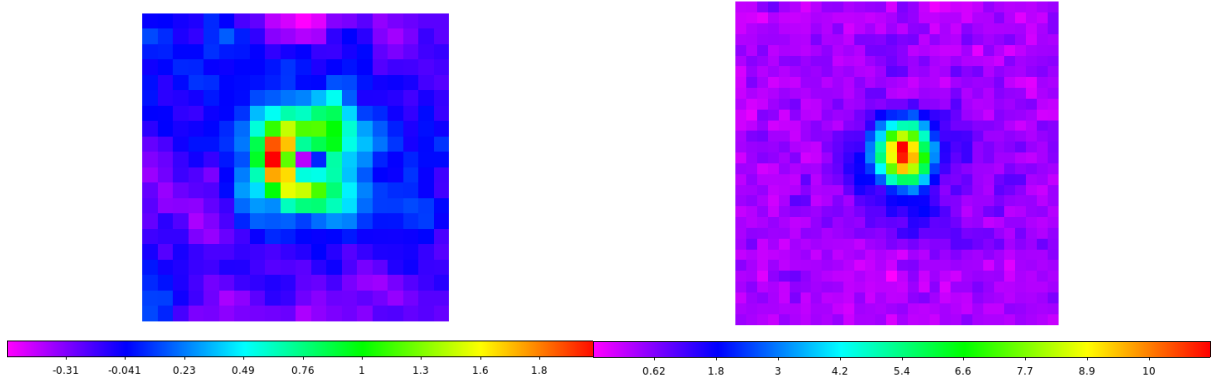


Figure 2.1: Resulting images using the two methods to extracted the PSF to case of Centaurus A in [SIV] filter. Left: If subtracted the PSF using the amplitude value derived from nuclear gaussian. Right: If subtracted the PSF using scale value where the final image is positive.

Our aim is to study if PAH molecules survive to the radiation field of the AGN. Several authors have claimed that the PAH molecules are destroyed by the radiation field of the AGN [e.g. Wu et al. , 2009], although it might survive [Alonso-Herrero et al., 2014] and even be induced by the AGN [Jensen et al., 2017]. If this PAH molecules are destroyed we expect SF regions (see at optical wavelengths) around the AGN that are not coincident with PAH emission. These scenarios could help us discern the convenience of PAHs as tracers of SF in AGNs.

Therefore, our purposes are two. Firstly to study the decrement of PAH emission at the inner 100 pc found by Esparza-Arredondo et al. [2018] and already argued by Alonso-Herrero et al. [2014] as a clue of the destruction of PAH emission under the presence of the AGN radiation field. Secondly, to study the origin of the [SIV] emission.

Our methodology along the last three semesters was the following. We created an atlas of [SIV] and PAH images for nearby AGN. For this we used available observations from CanariCam/GTC, T-ReCS/Gemini and VISIR/VLT from Asmus et al. [2014] catalog. Our first step was to check if these sources could be classified as extended. We created a method capable of isolating the emission using continuum images. For this purpose we subtracted the point spread function (PSF) and the continuum images. We fitted each image to two Gaussians to try to isolate nuclear from extended emission. We used the amplitude value derived from the nuclear gaussian to scale the PSF image and be able to do the subtraction of this in the source image. In figure 2.1 (left), we show an example of the resulting image using this procedure. Note that this procedure is not ideal because we obtained suspicious rings in most sources. These rings are due to the high variation of the sky at mid-IR. For this reason we scaled the final continuum subtraction to avoid negative numbers in the background (see Figure 2.1 right). We used the same procedure to extract the PSF in continuum images for each source. In the case of the [SIV], we only found three sources with continuum images available. We subtracted the continuum image at each of these sources using a scaling value to take into account the steepness of the continuum emission (see Figure 2.2). To calculate the scaling value, we used the *Spitzer* spectrum to know the flux ratios of wavelengths

centered on the line and the continuum. The flux values were calculated through most a linear fit using bands around the wavelength of each filter ([SIV] at $10.5\text{ }\mu\text{m}$ and continuum at $10.78\text{ }\mu\text{m}$, see Figure 2.2). In figure 2.3, we show the final figures for three cases of [SIV]. Note that only in the case of NGC 4579 we can see emission not associated to the nuclear component. Nevertheless, in the case of $11.3\text{ }\mu\text{m}$ PAH emission we had more continuum images available. We constructed a sample of 16 sources (see Figure 2.4). In this sample, 14 sources show an emission not associated with the nuclear component, indicating extended PAH emission around AGN. Our plan was then to compare this PAH emission with star-forming tracers at other wavelengths.

We downloaded the *HST* images from archive¹ in narrow filter (e.g. [SII] (F673N), H_β (F225N), and [OIII] (F502N)). Figure 2.5 shows the case of Centaurus A as an example. Note that we have a photometric problem when locating the center of this source and matching it in both wavelengths, due to poor astrometry of *HST* images. The *HST* images have a lot of extinction by dust in the nuclear part. Therefore, we concluded that it is not possible to isolate the nuclear emission in optical images.

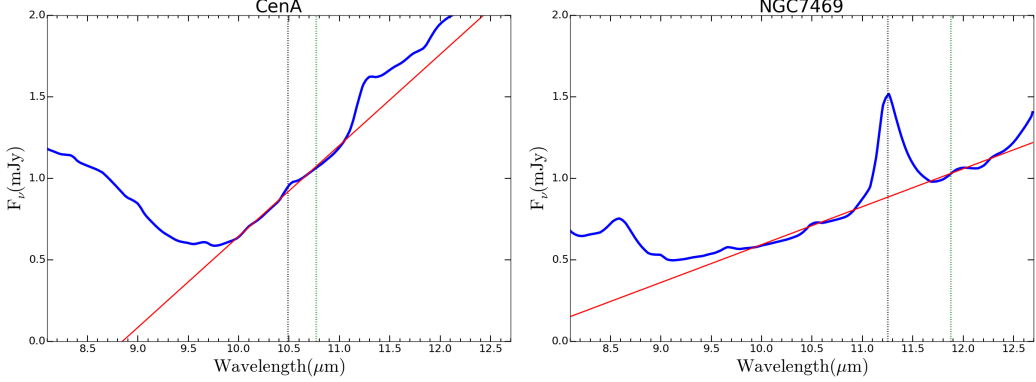


Figure 2.2: Centaurus A (right) and NGC 7469 (left) spectra. The red line represents the fit to [SIV] and $11.3\text{ }\mu\text{m}$ PAH emissions, respectively. The dotted lines show the wavelength of where are located the line/feature and continuum filters.

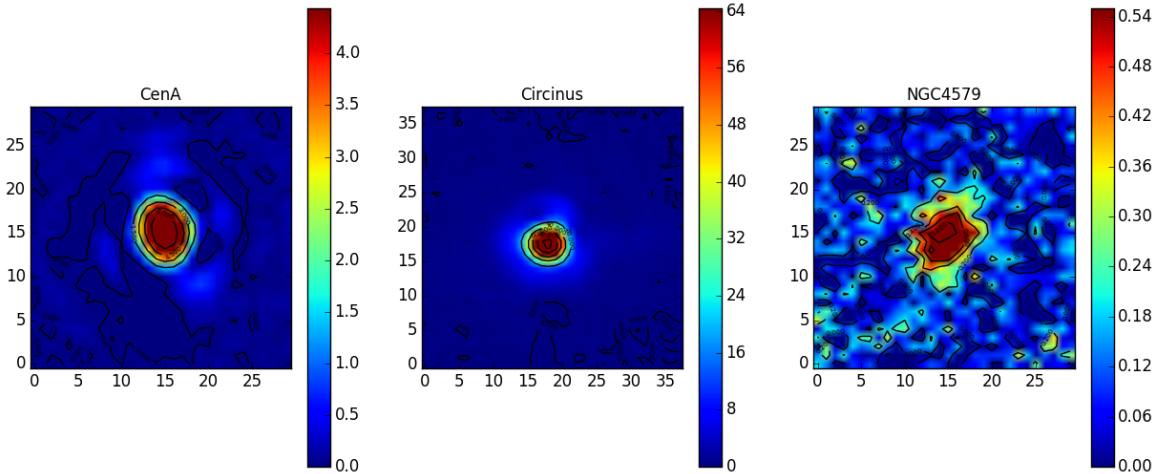


Figure 2.3: Resulting image to three sources where we extracted the continuum images for the case of [SIV] at $10.5\text{ }\mu\text{m}$. Each source shows six contours levels and on the right side is show the colors bars to each source.

¹<http://archive.stsci.edu/>

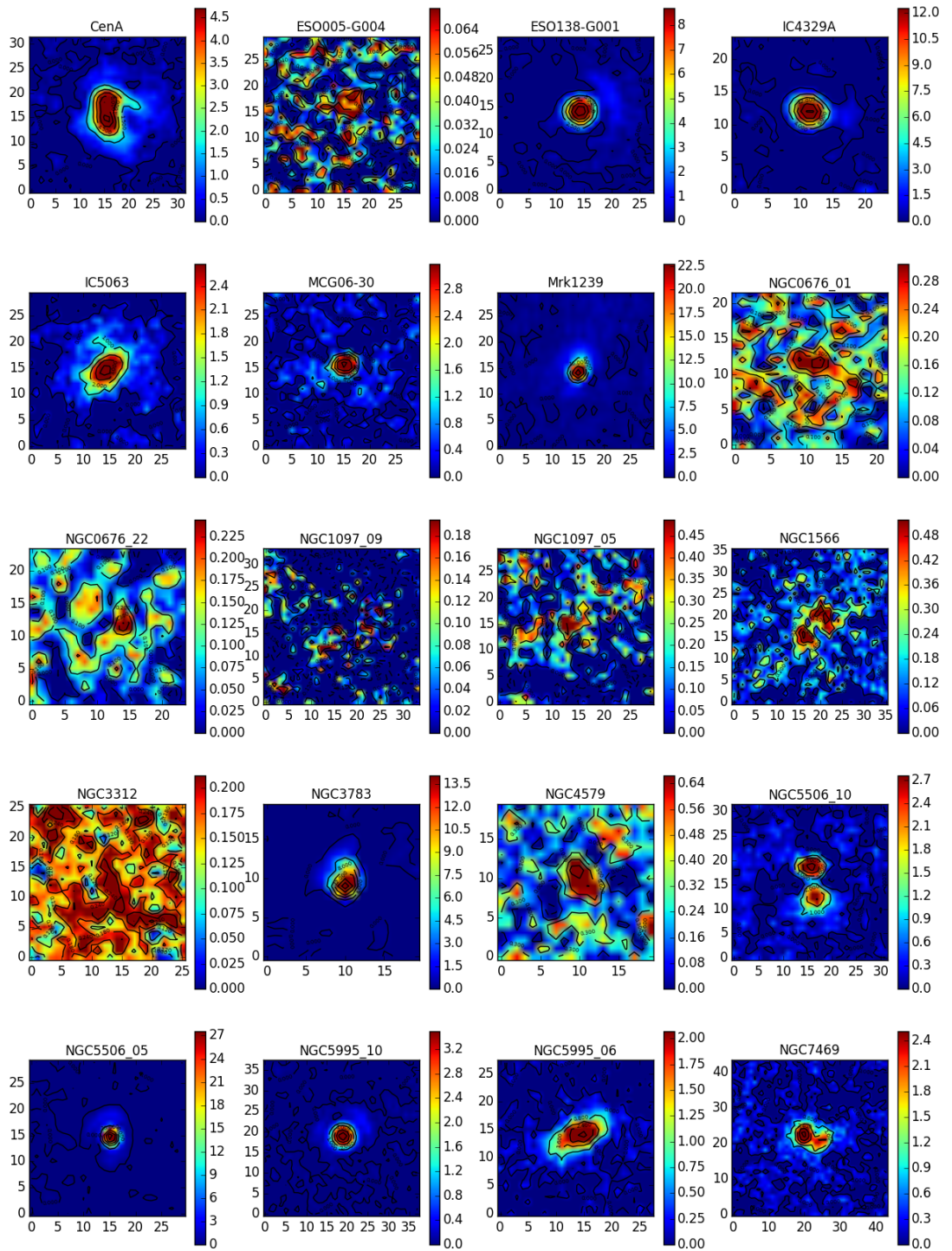


Figure 2.4: Images catalogue for case of $11.3\mu\text{m}$ PAH. Each source shows six contours levels and on the right side is show the colors bars to each source.

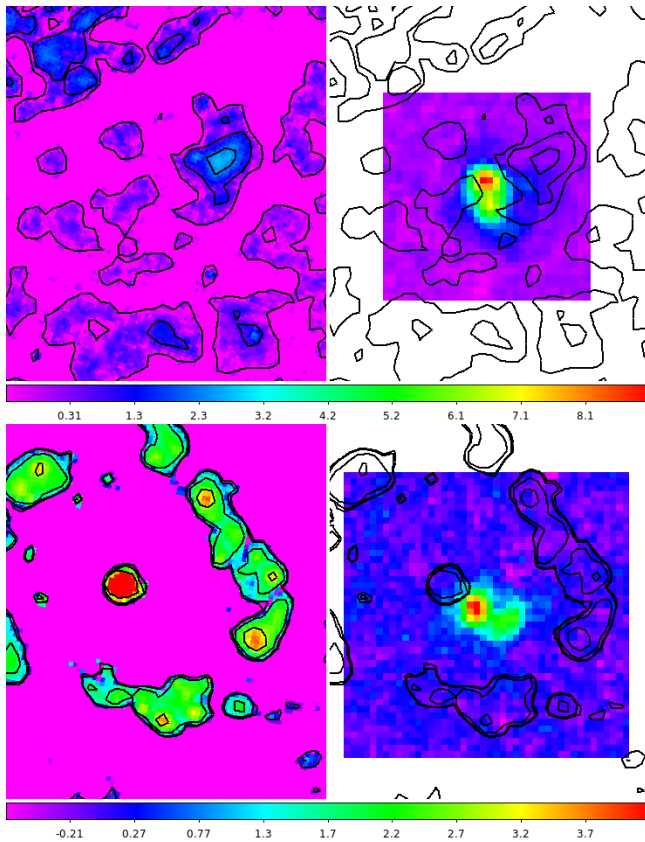


Figure 2.5: Top: Images in F673N (left) and $11.3\mu\text{m}$ PAH (right) filters to Centaurus A. Bottom: Images in FR656N (left) and $11.3\mu\text{m}$ PAH (right) filters to NGC 7469.

2.2 Alternative project: A comparison between [SIV] and [OIII] lines through diagnostic diagrams.

At the end of the third semester I made a stay with Dr. Brent Groves in the Research School of Astronomy and Astrophysics (RSAA) at the Australian National University (ANU). In this stay, I presented our work about the coevolution of star-formation and AGN activity in a meeting group. During this stay, I learned about photoionization tracers in optical wavelength. Also, I worked with Dr. Brent Groves to develop a project where we could link the mid-IR and optical tracers of SF and radiation field. We defined that the goal of our project is to show that [SIV] is as good a tracer as [OIII] of the radiation field in AGNs. Our specific objectives are: 1) To compare the $[\text{OIII}]/\text{H}_\beta$ and $[\text{SIV}]/[\text{NeII}]$ ratios for a sample of Seyfert galaxies, and 2) to compare the observations in both wavelengths on the diagnostic diagram with photoionization models (Mapping models²). Our first step was to create a sample of Seyfert galaxies with optical and mid-IR spectra available. We considered the sources of *Siding Spring Southern Seyfert Spectroscopic Snapshot Survey* (S7) presented by Dopita et al. [2015]; Thomas et al. [2017]. The S7 uses the Wide Field Spectrograph mounted on the ANU 2.3 m telescope located at the Siding Spring Observatory to deliver an integral field of 38×25 arcsec at a spectral resolution of $R = 7000$ in the red and $R = 3000$ in the blue. We found that 50 Seyfert sources from S7 have *Spitzer* spectra available in the CASSIS³ catalog. We did a quick test to review the viability of our plan using the $[\text{OIII}]$ and H_β nuclear measurements reported in Dopita et al. [2015]; Thomas et al. [2017]. We downloaded the reduced mid-IR spectra from CASSIS and measured the $[\text{SIV}]/[\text{NeII}]$ ratio for 11 sources. Only in these sources, the aperture size used to extract the mid-IR spectra matches that used in optical wavelength. In the case of the *Spitzer* spectra, we developed a script that followed the procedure described in section 3.1 of Esparza-Arredondo et al. [2018] to measure the flux and EW. These results are shown in figures 2.6. In the left figure, we show the relationship between mid-IR and optical ratios. Note that there seems to be a linear relationship between both wavelengths. On the right side, we show the location of this sources in BPT diagram.

²<https://miocene.anu.edu.au/mappings/>

³<http://cassis.astro.cornell.edu/atlas/>

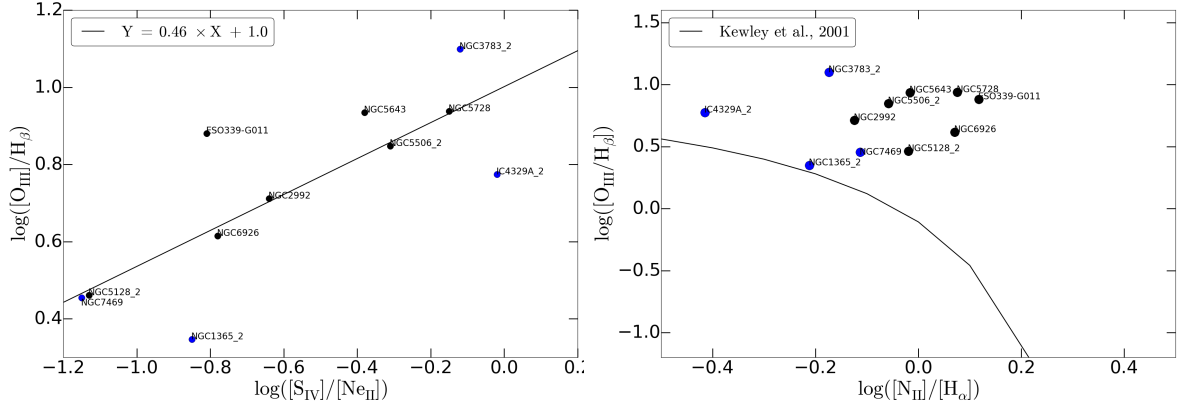


Figure 2.6: Left:Relationship between $[\text{S}_{\text{IV}}]/[\text{Ne}_{\text{II}}]$ and $[\text{O}_{\text{III}}]/\text{H}_{\beta}$. Right:Optical diagnostic diagram for nuclear spectra for the selected S7 data.

2.3 Working plan

Based on the current state of this part of the project, in this section, we describe the plan that we will follow for the remaining time of the PhD thesis.

In the case of the PAHs, we will compare with radio images, where we could find other tracers of star-formation as CO emission. Also, we will compare with X-ray, where we will study if PAHs emission could survive to the radiation field of the AGN.

In the case of $[\text{S}_{\text{IV}}]$, we will send an observational proposal to GTC (CanariCam) or VLT (VISIR). This depends on the availability of instruments. Once we have the mid-IR data, we will compare with images in other wavelengths. We are aware that the $[\text{S}_{\text{IV}}]$ part of the project has become complicated by postgraduate timing. Therefore, we will focus in developing the alternative plan with the working group lead by Dr. Brent Groves of the (RSAA, ANU). For this, we will work in complementing Figures 2.6. We have more *Spitzer* spectra available in the S7 sample, but we need to reduce them in order to match the aperture slit used for the optical observations. Next semester we will start to work on this. Once that we have reduced all spectra, we will measure the $[\text{S}_{\text{IV}}]$, $[\text{Ne}_{\text{II}}]$, $[\text{O}_{\text{III}}]$, and $[\text{Ne}_{\text{II}}]$ lines using the script developed. We will complement the diagnostic diagram using mid-IR and optical ratio at different apertures. The next step will consist of adding the photoionization models to our diagnostic diagram (mid-IR vs optical). This will allow us to study the $[\text{S}_{\text{IV}}]$ contamination due to SF. Our idea is to analyze the results and write a paper in collaboration with the RSAA research team.

The properties of the torus through simultaneous fitting of mid-IR and X-ray spectra.

3.1 Current status of the project

The third objective of our project is to explore the possibility that a simultaneous fitting of mid-IR and X-ray can better restrict the dust torus parameters. For this purpose, we used the nearby type-1.5 NGC 3516 as a test object. This object is ideal for the wealth of archival data, the closeness, and the relatively high AGN luminosity that seems to dominate both X-ray and mid-infrared frequencies. In particular, we included the high resolution IRS/*Spitzer* spectra for mid-infrared observations and *NuSTAR* observations for X-rays. We used the Clumpy models described by Nenkova et al. [2008a,b] for mid-infrared spectra and the radiative transfer code borus02 described by Baloković et al. [2018] for X-ray spectra. Borus model can be fitted within the X-ray spectral fitting software XSPEC. We developed a code capable of converting Clumpy models and IRS/*Spitzer* spectra into XSPEC format to simultaneously fit mid-infrared and X-ray data. We explored the resulting models to vary each parameter in the CLUMPY model adapted to Xspec (see Appendix A).

We fitted the mid-IR and X-ray spectra separately and later simultaneously. First, we fitted the *Spitzer* spectrum using the CLUMPY model. Then, we fitted the *NuStar* data using the X-ray model borus02. From these settings, we were able to constrain the N_0 , σ , Y , τ , Γ , $\log\text{NH}$, θ_{tor} , θ_i , parameters. Regarding the obtained parameters, we found that the inclination angle is consistent with an AGN type 1, as it is the case of NGC 3516. For the case of the simultaneous fit we linked the following parameters: τ (CLUMPY) with $\log\text{NH}$ (Borus02) and σ (Clumpy) with θ_{tor} (Borus02). The simultaneous fit is capable of better constraining Γ , τ ($\log\text{NH}$), θ_{inc} , σ (θ_{tor}), and q parameters, as demonstrated by the test performed on the degeneration of the parameters. We have finished this work and are tweaking details for publication.

3.2 Working plan for next semesters

Our simultaneous fit works correctly and the first results are promising; torus parameters are much better recovered by using both X-ray and mid-infrared wavelengths. Therefore, our plan is to finish writing and submit the paper for publication by the end of the fourth semester, where we will explain how this code works and the results of the first test (see Appendix C).

Our next step will be to construct a sample of nearby AGN with the propose of analyzing the torus. This sample will be based in the available data of mid-IR (e.g. IRS, CanariCam, and T-ReCS) and X-ray (e.g. *XMM-Newton*, *NuStar*, *Chandra*). We will use this sample to make an estimate of the parameters to model the dust torus components through simultaneous fitting. Finally, we will study if the torus changes with AGN parameters, such as the accretion rate, the SMBH mass, or the bolometric luminosity. We plan to publish these results in at least a peer reviewed paper (perhaps two depending on the quality and novelty of the results).

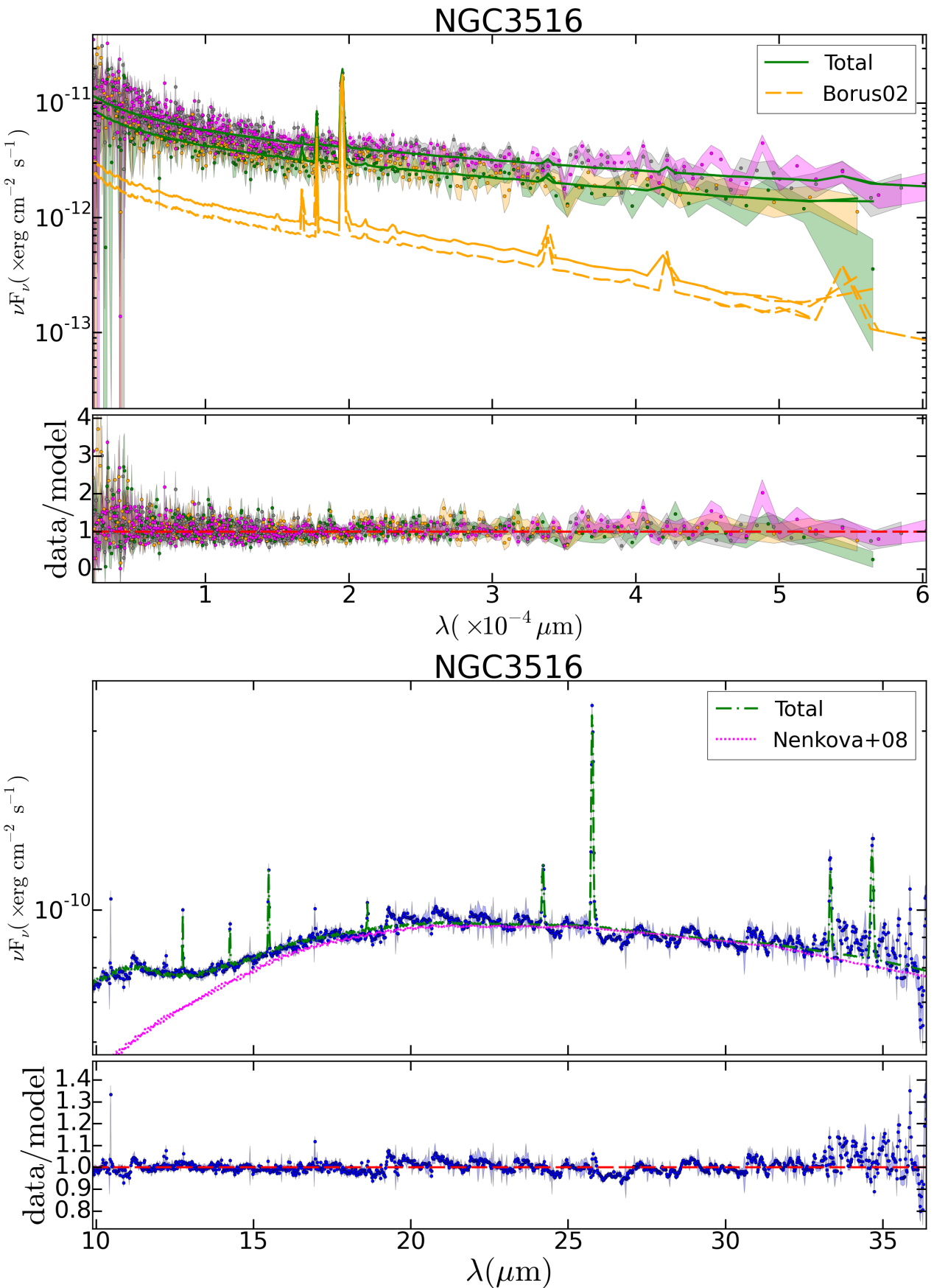


Figure 3.1: Top: Fit of the X-ray spectra using both models (NenkovaA08 and Borus02). Bottom: Fit of the *Spitzer* spectrum using both models.

Summary and Time table

In summary, in this document we have presented the advances up to date of each of the three objectives in the Phd project: 1) to study the [SIV] line as a tracer of the radiation field, 2) to study the $11.3 \mu m$ PAH feature as a tracer of star-formation in the environment of the AGN, and 3) to constrain the torus parameters using mid-infrared and X-ray simultaneous spectral fit.

As already mentioned, we are working on solving several difficulties to finish the first to objective. In the case of the [SIV] line, we will submit an observational proposal next semester to continue with the original plan: To compare high resolution images of the [SIV] filter with that also tracer the radiation field of the AGN. However, we will focus mainly on developing the alternative project, which has the same objective, but it uses optical and mid-IR spectra (see Section 2.2). In the case of the $11.3 \mu m$ PAH feature, we discard the idea of comparing the mid-IR with optical images. But, we will compare mid-IR with radio and X-ray images. We think that it is a good idea, because the radio images have better resolution than the optical and X-ray images will give us a counterpart of the AGN photoionization emission (see Chapter 2). Finally, the third objective, related with good estimation of torus parameters, has not presented large difficulties to be developed. The first part of this objective is finished and we are preparing a paper. We continue to develop this objective and we expect to produce one or two more publications.

The Table 4.1 shows a update time guide dedicated to the proposed objectives. The order of the objectives in the table is shown at the beginning of this section. The row called “others” is the time considered to prepare congress or meeting works, answer referee reports, write the thesis, bureaucratic procedures, etc. Each star represent one month. The orange stars are the time dedicated to prepare the phd project (first semester), this document (third semester), and the red stars are the dedicated time to prepared and present the thesis. As it can be seen in this table, our plan is to pursue these objectives mostly in parallel. This might seem to be less efficient but it has been probed to work so far. However, since objective 2 (PAH as tracer of SF) is close to be finished, we plan to have it finished within two semesters. In Appendix D we attach the PhD project presented to the academic committee at the end of the first semester.

	S1	S2	S3	S4	S5	S6	S7	S8
Objective 1	**	**	*	**	**	**		
Objective 2	*	**	*	**	*			
Objective 3		*	**	**	**	**	***	
Others	**	*	* *		*	**	**	*****

Table 4.1: Currently time guide of the project.

Appendix A: The properties of the torus through simultaneous setting of mid-IR and X-ray spectra.

The properties of the torus through simultaneous setting of mid-IR and X-ray spectra.

We explored the resulting models to vary each parameter in the CLUMPY model adapted to Xspec. Figures 5.2, 5.3, and 5.4 show the resulting SEDs to vary one parameter of the model and consider the minimum, medium, and maximum values for the rest of the parameters, respectively. The colored lines in each panel represent the results where the minimum (green), medium (black), and maximum (red) values vary for the selected parameter in each case. This exercise helped us to get familiarized with the parameters used to make a fitting in mid-IR and know the dependence of models regarding each parameter. For example, in the case of the inclination parameter (i), we found that this parameter does not influence in the model if we considered minimum values. However, the model changes this parameter at wavelengths of $10\ \mu\text{m}$ if we consider maximum values for the rest of parameters. In case of half opening angle, we found a difference in all resulting models.

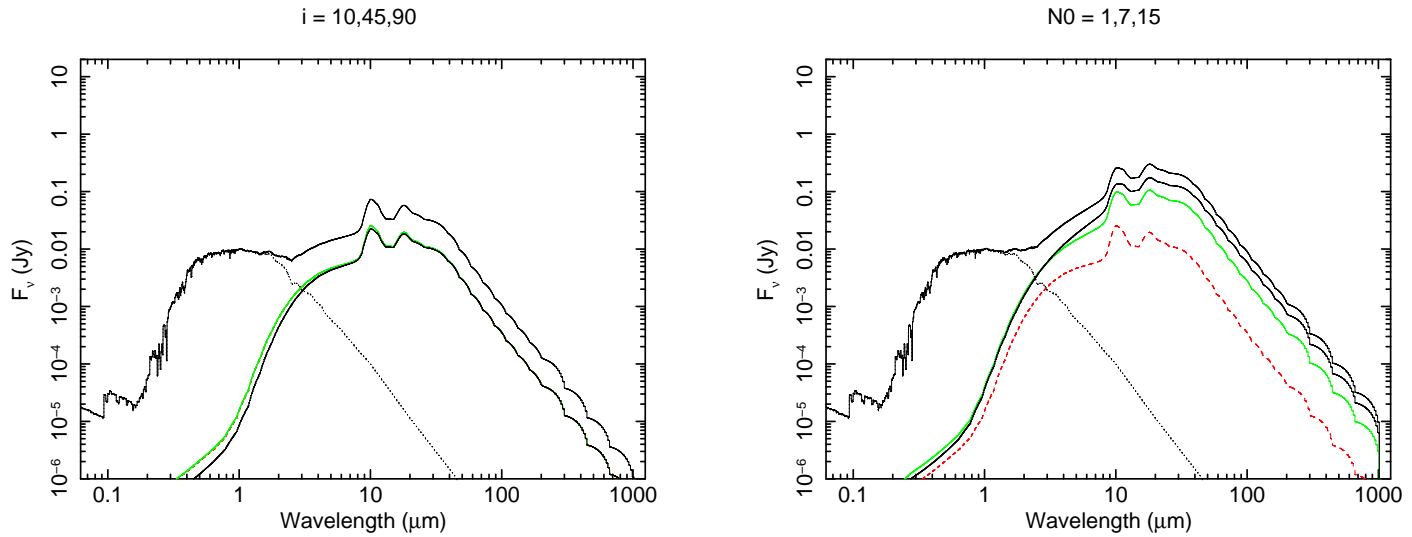


Figure 5.1: Obtained SEDs using the minimum value to CLUMPY parameters.

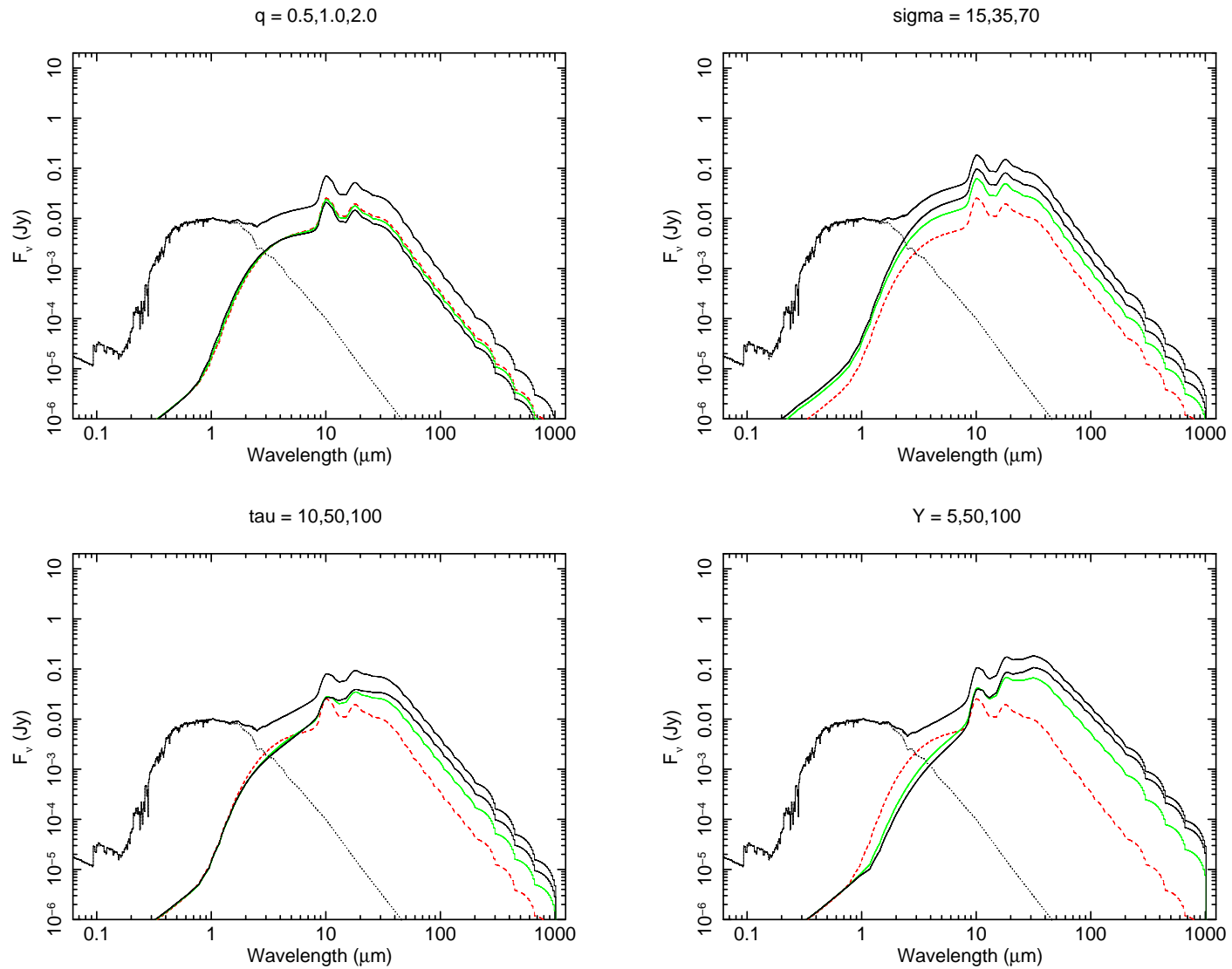


Figure 5.2: Continued: Obtained SEDs using the minimum value to CLUMPY parameters.

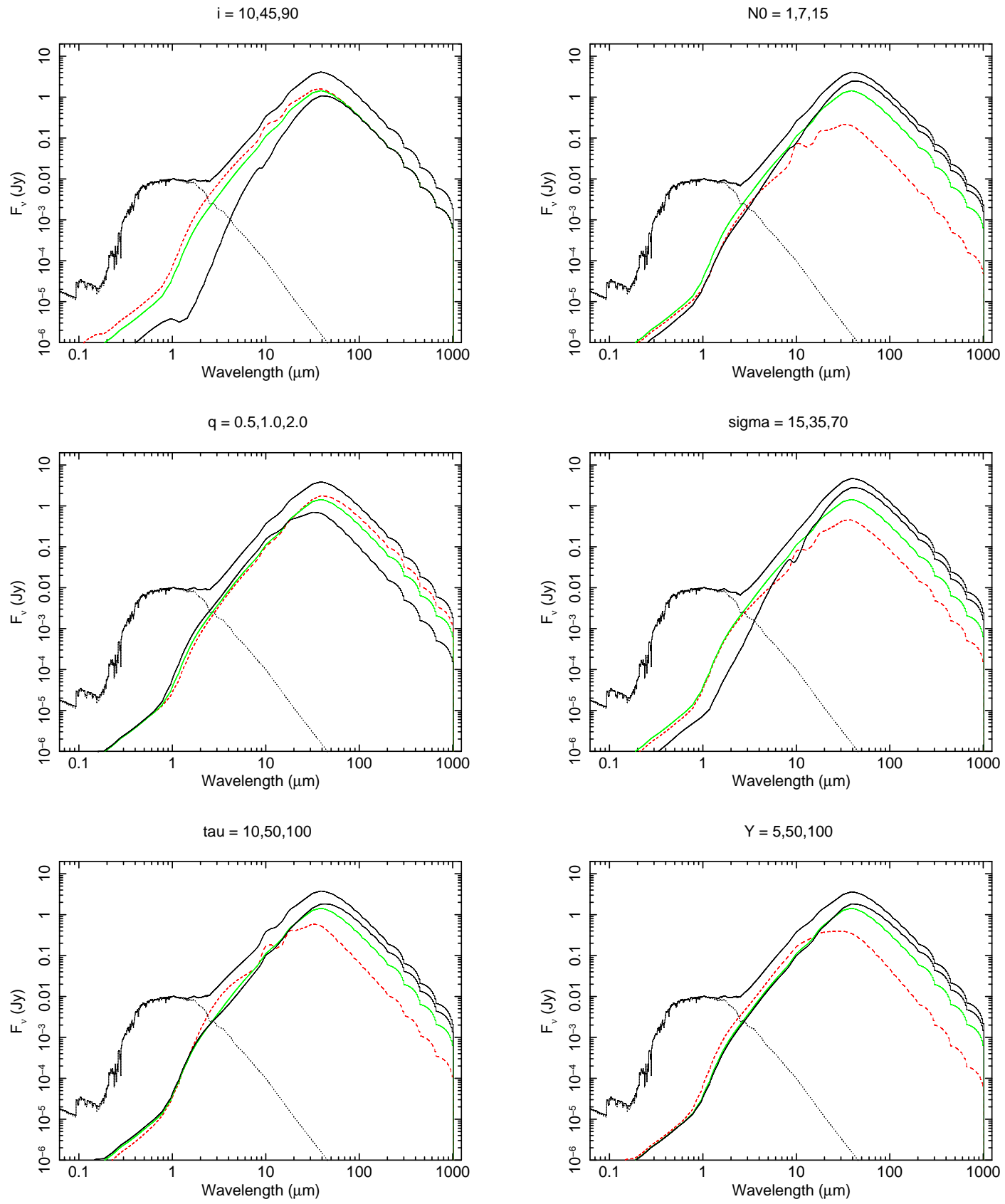


Figure 5.3: Obtained SEDs using the medium value to CLUMPY parameters.

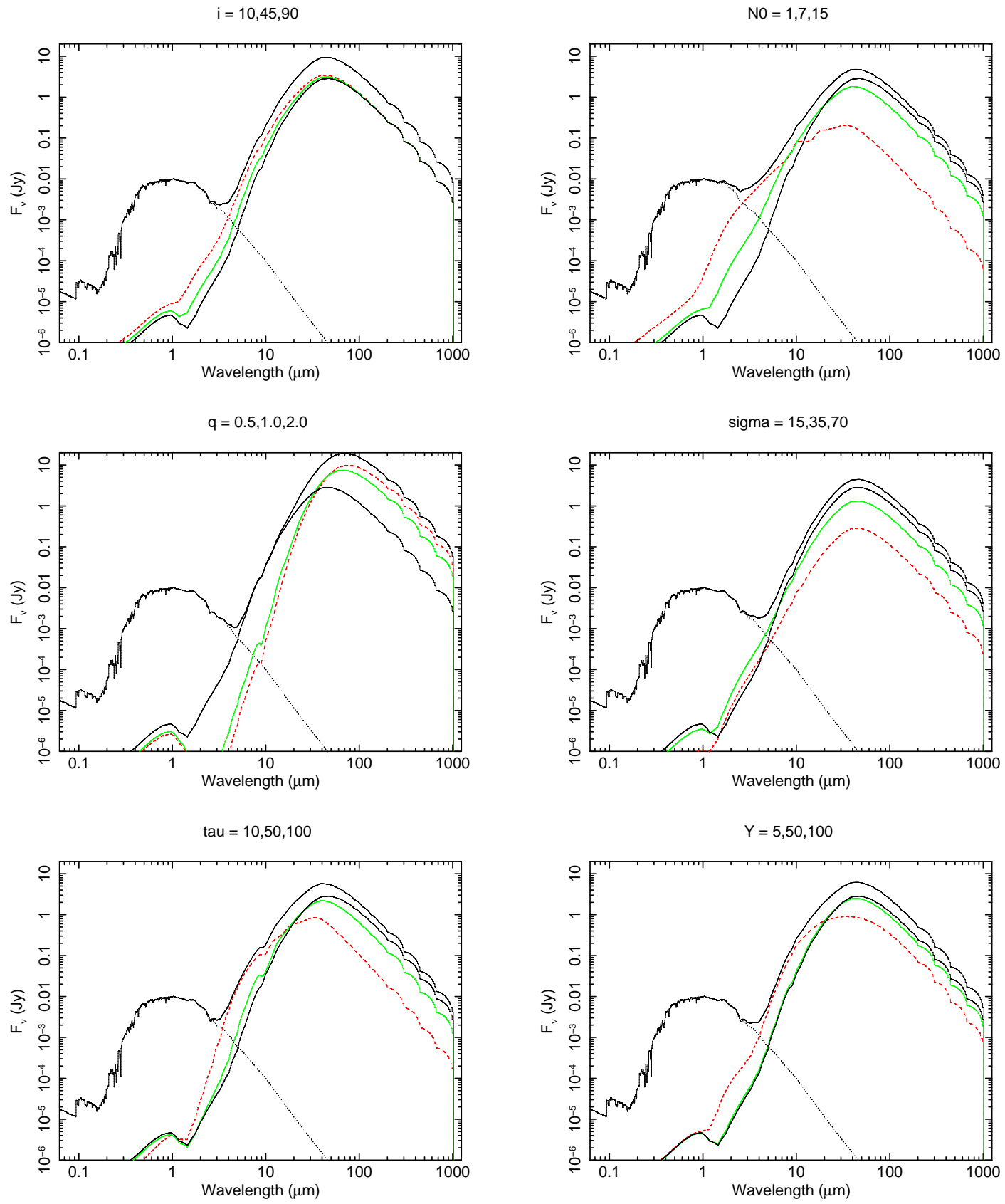


Figure 5.4: Obtained SEDs using the maximum value to CLUMPY parameters.

Appendix B: Circumnuclear star-formation and AGN activity: Clues from surface brightness radial pro- file of PAHs and [SIV].

**PAPER: Circumnuclear star-formation and AGN activity:
Clues from surface brightness radial profile of PAHs and [SIV].**



Circumnuclear Star Formation and AGN Activity: Clues from Surface Brightness Radial Profile of PAHs and [S IV]

Donaji Esparza-Arredondo¹ , Omaira González-Martín¹ , Deborah Dultzin², Almudena Alonso-Herrero^{3,4,5} , Cristina Ramos Almeida^{6,7} , Tanio Díaz-Santos⁸ , Ismael García-Bernete⁶, Mariela Martínez-Paredes¹, and Jose Miguel Rodríguez-Espinoza^{6,7}

¹ Instituto de Radioastronomía y Astrofísica, Universidad Nacional Autónoma de México, Campus Morelia, Apartado Postal 3-72, 58090, Morelia, Michoacán, México; d.esparza@crya.unam.mx

² Instituto de Astronomía, Universidad Nacional Autónoma de México, Apartado Postal 70-264, 04510, CDMX, México
³ Centro de Astrobiología (CAB, CSIC-INTA), ESAC Campus, E-28692 Villanueva de la Cañada, Madrid, Spain

⁴ Department of Physics, University of Oxford, Oxford OX1 3RH, UK

⁵ Department of Physics and Astronomy, University of Texas at San Antonio, San Antonio, TX 78249, USA

⁶ Instituto de Astrofísica de Canarias (IAC), C/Vía Láctea, s/n, E-38205 La Laguna, Spain

⁷ Departamento de Astrofísica, Universidad de La Laguna, E-38206 La Laguna, Tenerife, Spain

⁸ Núcleo de Astronomía de la Facultad de Ingeniería, Universidad Diego Portales, Av. Ejército Libertador 441, Santiago, Chile
Received 2017 June 16; revised 2018 April 4; accepted 2018 April 5; published 2018 May 30

Abstract

We studied the circumnuclear mid-IR emission in a sample of 19 local active galactic nuclei (AGNs) with high spatial resolution spectra using T-ReCS (Gemini) and CanariCam (GTC), together with *Spitzer*/IRS observations. We measured the flux and the equivalent width for the 11.3 μm PAH feature and the [S IV] line emission as a function of galactocentric distance. This allowed us to study the star formation (SF) at subkiloparsec scales from the nucleus for a large sample of nearby AGNs. The [S IV] line emission could be tracing the AGN radiation field within a few thousand times the sublimation radius (R_{sub}), but it often peaks at distances greater than 1000 R_{sub} . One possibility is that the SF is contributing to the [S IV] total flux. We found an 11.3 μm PAH emission deficit within the inner few tens of parsecs from the AGN. This deficit might be due to the destruction of the molecules responsible for this feature or the lack of SF at these distances. We found a sensible agreement in the expected shift of the relation of the AGN bolometric luminosity and the SF rate. This indicates that numerical models attributing the link between AGN activity and host galaxy growth to mergers are in agreement with our data, for most inner galaxy parts.

Key words: galaxies: active – galaxies: evolution – galaxies: nuclei

1. Introduction

The understanding of the coevolution of active galactic nuclei (AGNs) and the host galaxy has been one of the greatest challenges in astronomy in the past decades. Several studies have discovered correlations between the mass of the supermassive black hole (SMBH), the mass of the bulge (Magorrian et al. 1998; Tremaine et al. 2002; Marconi & Hunt 2003; McConnell & Ma 2013), and the bulge velocity dispersion (Kormendy & Richstone 1995; Ferrarese & Merritt 2000). However, the physical connection between these observational properties is still unclear. The study of SMBH accretion and circumnuclear⁹ star formation (SF) can be the key. Some authors propose that the gas that moves toward the center is responsible for both the growth of the SMBH and the enhancement of SF (Sanders et al. 1988; Barnes & Hernquist 1991; Storchi-Bergmann et al. 2001). Other works suggest that quenching of SF is due to AGN feedback (Silk & Rees 1998; Vollmer & Davies 2013, and references therein).

Numerical simulations propose a scenario where large-scale processes can be related to small-scale phenomena close to the nucleus (e.g., Kawakatu & Wada 2008; Hopkins & Quataert 2010; Neistein & Netzer 2014; Gutcke et al. 2015; Volonteri et al. 2015). According to these studies, major mergers and even tidal interactions produce perturbations that can be correlated with the accretion of the SMBH and SF (Krongold

et al. 2002). Other authors propose a scenario in which the radiation field of the SMBH is able to stop the SF, imposing a balance between the two (e.g., Wu et al. 2009).

The study of the neighborhood of AGNs is very complex because the classic indicators of SF such as the ultraviolet (UV) continuum, Pa α , and H α emission line are easily contaminated by the powerful AGN emission (Alonso-Herrero et al. 2014, and references therein). However, the mid-infrared (MIR) wavebands are a powerful tool to disentangle SF and AGN contributions (e.g., Dultzin-Hacyan et al. 1990; González-Martín et al. 2013; Alonso-Herrero et al. 2014). Recently, new MIR spectroscopic data have provided opportunities to quantify the SF close (<1 kpc) to the AGN (e.g., Esquej et al. 2014; Ruschel-Dutra et al. 2017). The polycyclic aromatic hydrocarbon (PAH) emission features at 3.3, 6.2, 7.7, 8.6, and 11.3 μm contribute to MIR flux. The PAHs are composed of 20–100 atoms of carbon and hydrogen (Millar & Williams 1993). These features are powerful tools to study SF on the vicinity of AGNs. These molecules have been studied in different objects associated with dust and gas including evolved stars, reflection nebulae, Orion bars, and star-forming regions (Gillett et al. 1973; Cohen et al. 1986; Aitken & Roche 1984). It is known that the PAH emissions are good tracers of young and massive stars (i.e., recent circumnuclear SF activity). In particular, starburst galaxies show a good correlation between the strength of the PAH and the IR luminosity, indicating that they are good tracers of SF (Brandl et al. 2006).

⁹ We considered circumnuclear scales at distances less than 1 kpc.

Among these PAH features, the $11.3\text{ }\mu\text{m}$ PAH feature has the advantage of being isolated (i.e., not blended) from others and is observable with ground-based telescopes (i.e., with enough spatial resolution to disentangle the contribution of the few tenths of parsecs from the nucleus in nearby galaxies). Indeed, the $11.3\text{ }\mu\text{m}$ PAH emission feature has been used in several works to study the SF in the vicinity of AGNs (e.g., Diaz-Santos et al. 2010). Recently, Esquej et al. (2014) computed the SF rate (SFR) from this feature and compared it with the AGN accretion rate. They confronted this relation with coevolution models elaborated by Hopkins & Quataert (2010). They found a good agreement between observations and theoretical models for physical scales of ~ 100 pc. Recently, Ruschel-Dutra et al. (2017) have analyzed the circumnuclear SF in a sample of 15 AGNs in order to investigate the validity of the same relation. They found that SF luminosities are correlated with the bolometric luminosity of the AGN (for objects with $L_{\text{bol,AGN}} \geq 10^{42}\text{ erg s}^{-1}$).

The PAH features have been studied in the vicinity of the AGNs of many galaxies. Some authors claim that these molecules are destroyed by the strong AGN radiation field (Voit 1992; Wu et al. 2009; Diaz-Santos et al. 2010). Siebenmorgen et al. (2004) and Ruschel-Dutra et al. (2014) have found evidence in favor of this destruction of PAHs in AGNs. Supporting this, the correlation between the strength of the PAH features and the IR luminosity appears to be absent or weak in AGNs (Weedman et al. 2005). If this were the case, the PAH emission feature could not be used as a tracer of SF in AGNs. In a more recent paper, it has been suggested that PAH emission might not be a good tracer of the SF within 1 kpc around an AGN (Jensen et al. 2017).

Against it, Alonso-Herrero et al. (2014) concluded that at least those molecules responsible for the $11.3\text{ }\mu\text{m}$ PAH feature survive in the nuclear environment as close as 10 pc from the nucleus for their sample of six local AGNs (see also Esquej et al. 2014; Ramos Almeida et al. 2014). They propose that material in the dusty tori, nuclear gas disk, and/or host galaxies of AGNs is likely providing the column density necessary to protect the PAH molecules from the AGN radiation field.

Here we investigate whether the $11.3\text{ }\mu\text{m}$ PAH can be used (and at which scales) as a tracer of SF, and we use it to get some clues about the coevolution between the AGN and its host galaxy. For that purpose we have compiled a sample of high spatial resolution spectra ($8\text{--}13\text{ }\mu\text{m}$) of local AGNs observed with T-ReCS in the Gemini South Observatory and CanariCam on the 10.4 m Gran Telescopio CANARIAS (GTC). This allowed us to study the SF at different scales from the nucleus for a large sample of sources. The coverage of these spectra will also allow us to analyze the origin of the [S IV] line emission at $10.5\text{ }\mu\text{m}$. The [S IV] line arises from ions with an ionization potential of 35 eV. It has been proposed as an indicator of the AGN isotropic luminosity since it might come from the narrow-line region (NLR; Dasyra et al. 2011). However, high spatial resolution MIR spectra indicate that this emission is not resolved at 100 pc scales, against its NLR origin (Hönig et al. 2008). The [S IV] line emission at $10.5\text{ }\mu\text{m}$ could also be related to star-forming regions (Pereira-Santalla et al. 2010). Our high spatial resolution spectra are very well suited to understand the origin of the [S IV] line emission.

The main goal of this work is to address three questions: (1) the origin of [S IV] line emission, (2) the goodness of the $11.3\text{ }\mu\text{m}$ PAH feature as a tracer of SF in the vicinity of AGNs,

and (3) the connection between SF and AGN activity. The paper is organized as follows: Section 2 presents our sample and the data reduction. Section 3 presents the analysis of the spectra. Sections 4 and 5 provide a discussion of the main results in the framework of our goals. Finally, a brief summary is given in Section 6. Throughout this work, we assumed a ΛCDM cosmology with $\Omega_\Lambda = 0.73$, $\Omega_M = 0.27$, and $H_0 = 70\text{ km s}^{-1}\text{ Mpc}^{-1}$.

2. Sample Selection and Data Reduction

2.1. Sample

Our sample consists of 19 local AGNs with ground-based N -band (i.e., $8\text{--}13\text{ }\mu\text{m}$) spectra available. All spectra have been observed with ground-based telescopes. These sources are taken from the samples of González-Martín et al. (2013) and Alonso-Herrero et al. (2016), which contain 22 and 45 local AGNs, respectively. We have only included AGNs showing extended emission. We considered the source as extended if we can detect emission of the $11.3\text{ }\mu\text{m}$ PAH feature or [S IV] line in more than three circumnuclear apertures (see Section 3 for a detailed explanation on the aperture extraction procedure).

This sample is the largest reported where high-resolution studies have been done in the vicinity of AGNs. However, note that this sample is not complete in any sense. Table 1 shows the main observational details of the sample. Fifteen objects are type 2 Seyferts (Sy2), and four are type 1 Seyferts (Sy1). Our sample covers a range of X-ray luminosity (absorption corrected) of $L(2\text{--}10\text{ keV}) \sim 5 \times 10^{39}\text{--}4 \times 10^{43}\text{ erg s}^{-1}$. The range of X-ray luminosity covers classical Seyfert galaxies and low-luminosity AGNs ($< 10^{42}\text{ erg s}^{-1}$). The Appendix contains a short review of the published information on star-forming regions around these objects, when available.

Eleven objects were observed with the Thermal-Region Camera Spectrograph (T-ReCS; Telesco et al. 1998; De Buizer & Fisher 2005) located in the 8.1 m Gemini South Telescope and published by González-Martín et al. (2013) (and references therein). The slit width used for the spectroscopy results in a spatial resolution in the range of $\sim 20\text{--}250$ pc (see Column (9) in Table 1). The rest of the sources in our sample were obtained with CanariCam (Telesco et al. 2003) in the 10.4 m Gran Telescopio CANARIAS (GTC) and were published by Alonso-Herrero et al. (2016). For these eight sources the slit width used for the spectroscopy results in a spatial resolution in the range of $\sim 50\text{--}160$ pc. The angular and spectral resolutions for both instruments (T-ReCS and CanariCam) are within an average of $\text{FWHM} \sim 0.3\text{ arcsec}$ and $R \sim 100$, respectively. Note that these spectral resolutions are not high enough to examined the width of the [S IV] line. Indeed, all the [S IV] emission lines reported here have a width compatible with the instrumental spectral resolution.

We have included the *Spitzer*/IRS spectral data downloaded from the CASSIS¹⁰ catalog (the Cornell AtlaS of *Spitzer*/IRS Sources; Lebouteiller et al. 2011) to study larger regions in each galaxy. Note that the spectral resolution of *Spitzer*/IRS ($R \sim 60\text{--}130$) is similar to that obtained by our ground-based observations. CASSIS provides flux-calibrated nuclear spectra associated with each observation. The *Spitzer* spectra are not available for four of the sources in our sample (NGC 931, NGC 1320, NGC 4569, and NGC 7465). In four additional

¹⁰ <http://cassis.astro.cornell.edu/atlas/>

Table 1
General Properties of Sample

Object	Type	D (Mpc)	L_x^A $\log(L(2\text{--}10 \text{ keV}))$	M_{BH}^B $\log(M/M_\odot)$	Instrument	P.A. (deg)	Scale Factor (8)	Slit Width (Nuclear) (arcsec/pc)	$Spitzer$ Slit Width (arcsec/pc)	Radius (in/out) (pc/pc)	R_{subl} (pc)	$\log d_{25}$ $\log(0.1 \text{ arcmin})$	Ref. (14)
(1)	(2)	(3)	(4)	(5)	(6)	(7)		(9)	(10)	(11)	(12)	(13)	
NGC 931	Sy1	49.4	43.3 (c)	8.3 (I)	CanariCam	80	—	0.52/124.5	—	93.4/242.8	0.24	1.39	2
Mrk 1066	Sy2	51.7	42.9 (a)	7.0 (I)	CanariCam	315	1.23	0.52/130.3	3.7/927.3	87.9/440.3	0.09	1.08	2,4
NGC 1320	Sy2	37.7	42.5 (c)	7.2 (I)	CanariCam	315	—	0.52/95.0	—	149.7/406.4	0.03	1.27	2
NGC 1386	Sy2	16.2	41.6 (a)	7.4 (I)	T-ReCS	0	1.17	0.31/24.4	3.7/291.1	31.8/88.3	0.02	1.55	1
NGC 1808	Sy2	11.5	39.7 (a)	6.7 (II)	T-ReCS	45	1.35	0.35/19.6	3.7/207.2	27.6/62.8	0.002	1.73	1
NGC 2992	Sy1.8	31.6	41.9 (c)	7.7 (I)	CanariCam	30	0.4	0.52/79.7	3.7/566.8	59.7/741.2	0.03	1.47	2
NGC 3081	Sy2	32.5	42.5 (b)	7.1 (II)	T-ReCS	0	0.96	0.65/102.4	3.7/582.9	63.6/205.0	0.06	1.43	1
"	"	"	"	"		350	0.92	"	"	91.9/205.1	"	"	
NGC 3227	Sy1.5	21.8	42.1 (c)	7.6 (I)	CanariCam	0	0.64	0.52/54.9	3.7/391.0	74.2/205.6	0.04	1.60	2
NGC 3281	Sy2	21.8	43.2 (a)	7.9 (II)	T-ReCS	315	0.61	0.35/77.6	3.7/820.0	109.4/248.6	0.14	1.49	1,4
NGC 4253 ^a	Sy1	55.4	42.5 (c)	6.8 (III)	CanariCam	285	0.75	0.52/139.6	—	94.2/408.3	0.06	0.95	2
NGC 4569	Sy2	12.6	39.4 (e)	7.8 (IV)	CanariCam	30	—	0.52/31.7	—	19.1/285.9	0.004	1.96	2
NGC 5135 ^a	Sy2	58.6	43.1 (b)	7.3 (II)	T-ReCS	30	1.33	0.70/199.0	—	89.3/1033.5	0.13	1.38	1,3
NGC 5643	Sy2	16.9	42.6 (b)	7.4 (II)	T-ReCS	80	0.68	0.35/28.7	3.7/303.1	55.2/106.6	0.07	1.72	1
IC 4518W [*]	Sy2	69.6	42.6 (b)	7.5 (V)	T-ReCS	5	1.22	0.70/236.3	—	166.7/560.6	0.07	1.10	1,3
IC 5063 ^a	Sy2	48.6	42.9 (c)	7.7 (I)	T-ReCS	303	1.33	0.65/153.1	—	95.2/306.7	0.09	1.43	1,5
NGC 7130	Sy2	69.2	42.9 (a)	7.6 (II)	T-ReCS	348	1.35	0.70/234.7	3.7/1240.7	135.4/496.6	0.09	1.19	1,3
NGC 7172	Sy2	33.9	42.7 (a)	7.7 (II)	T-ReCS	60	0.57	0.35/57.5	3.7/608.0	95.8/228.6	0.08	1.44	1,6
NGC 7465	Sy2	27.2	41.4 (d)	7.6 (VI)	CanariCam	330	—	0.52/68.6	—	46.3/200.6	0.03	1.03	2
NGC 7582	Sy2	22.5	42.6 (b)	7.1 (II)	T-ReCS	0	0.39	0.70/76.4	3.7/403.6	53.8/396.6	0.07	1.84	1

Notes. Column (1): source name. Column (2): type of sources according to González-Martín et al. (2013) or Alonso-Herrero et al. (2016). Column (3): distances calculated from redshift obtained from observations for $\Omega_\Lambda = 0.73$, $\Omega_M = 0.27$, and $H_0 = 70 \text{ km s}^{-1} \text{ Mpc}^{-1}$. Column (4): X-ray luminosity. Column (5): BH mass. Column (6): instrument used by each object. Column (7): position angle. Column (8): scale factor between T-ReCS/CanariCam and $Spitzer$ spectra. The mark “*” is used to identify the sources where we do not use the $Spitzer$ spectra. Column (9): Slit width for nuclear spectra. Column (10): slit width for $Spitzer$ spectra. Column (11): minimum and maximum radius used for the extended profiles (T-ReCS or CanariCam). Column (12): sublimation radius. Column (13): isophotal diameter. Column (14): references where the observations were originally published: (1) González-Martín et al. 2013; (2) Alonso-Herrero et al. 2016; (3) Diaz-Santos et al. 2010; (4) Sales et al. 2011; (5) Young et al. 2007; (6) Roche et al. 2007.

^a The references for the X-ray results are (a) González-Martín (2018), (b) González-Martín et al. (2013), (c) Liu et al. (2014), (d) O’Sullivan et al. (2001), (e) Ho et al. (2001).

^b The BH mass is calculated using the relation with the stellar velocity dispersion. References: (I) Woo & Urry (2002), (II) Esquej et al. (2014), (III) Woo et al. (2015), (IV) Mason et al. (2015), (V) Alonso-Herrero et al. (2013), (VI) Dudik et al. (2005).

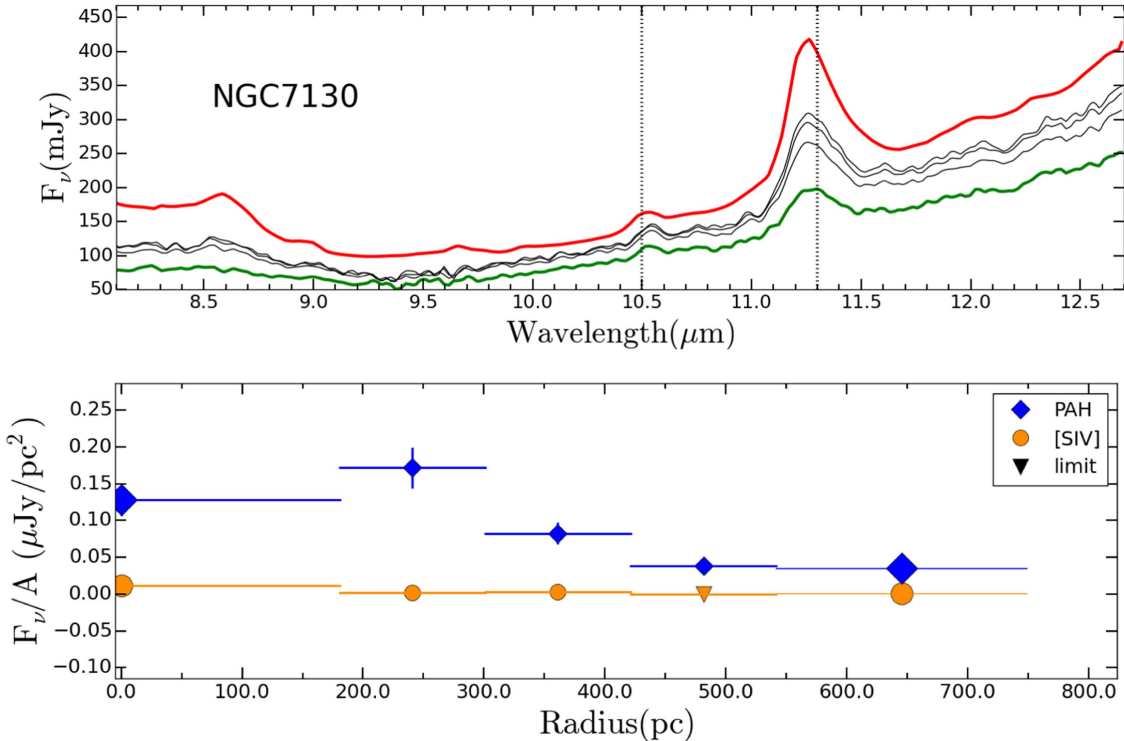


Figure 1. Top: extracted spectra at different scales for NGC 7130. The red line is the spectrum obtained by *Spitzer*, and the green and black lines correspond to the nuclear spectrum and extended-aperture spectra, respectively. The dotted lines show the PAH feature and [S IV] line emissions. Bottom: surface brightness radial profiles in units of $\mu\text{Jy}/\text{pc}^2$ for NGC 7130. We first extracted the flux at the radius of each aperture, and then we subtracted that of all inner apertures to get the flux of a ring. The radial profile for 11.3 μm PAH emission is presented with blue diamonds, while the radial profile for [S IV] line emission is shown with orange circles (the triangles are limit values). The larger symbols (diamonds or circles) correspond to the nuclear and *Spitzer* spectra, respectively. The rest of the symbols represent the measurements for the extended apertures.

sources we did not use the *Spitzer* data because the emission of the ground-based data extends up to the spatial resolution of *Spitzer* data. Therefore, these observations do not add extra information to our ground-based data. Thus, we included *Spitzer*/IRS spectra for 11 of the objects; Column (10) in Table 1 shows the *Spitzer* radius spectra when we used them in the analysis.

González-Martín et al. (2013) and Alonso-Herrero et al. (2016) focused their analyses on the nuclear emission. Also focusing on the central region, four sources have been observed with VISIR/VLT and reported by Hönig & Kishimoto (2010). Furthermore, the MIR extended emission of some of our sources has been studied individually before. Three of our sources (NGC 5135, IC 4518W, and NGC 7130) were studied by Diaz-Santos et al. (2010). They studied the extended emission of different features, including the 11.3 μm and the [S IV] line, and they compared it with the *Spitzer* spectra. Mrk 1066 was analyzed by Ramos Almeida et al. (2014) and Alonso-Herrero et al. (2014) to study the survival of the responsible molecules for the 11.3 μm PAH feature in the close vicinity of an AGN. García-Bernete et al. (2015) studied the extended emission of NGC 2992 up to ~ 3 kpc, finding that PAH features might indicate that the bulk of this extended emission is dust heated by SF. Esquej et al. (2014) compared nuclear with larger apertures (using *Spitzer* spectra) in 12 of our sources to study the correlation between SFR through the 11.3 μm PAH feature and AGN accretion. These works will be compared with our results throughout this paper.

2.2. Data Reduction

The data have been reduced using the RedCan pipeline (González-Martín et al. 2013). RedCan is a fully automated pipeline that was designed to efficiently exploit CanariCam data. Due to the similarities between CanariCam and T-ReCS low spectral resolution data, this pipeline can analyze successfully both sets of observations considered in this paper. RedCan is able to produce flux-calibrated images and 1D spectra. The main input is an ASCII file, which contains an observation list. The reduction process basically consists of eight steps: (1) identification of files, (2) flat-fielding, (3) stacking, (4) image flux calibration, (5) wavelength calibration, (6) trace determination, (7) spectral extraction, and (8) spectral flux calibration and the combination of spectra. Within these steps, the subtraction of the sky background and rejection of bad images are also included. Flux calibration is performed by observing standard stars taken immediately before or after the target.

Spitzer/IRS spectra provided by CASSIS are already reduced. However, observations using data from both short-low and long-low spectra modules suffer from mismatches due to telescope pointing inaccuracy or due to a different spatial resolution of the IRS orders. This is not corrected in the final products given by CASSIS. Still, in this work it is not necessary to correct these mismatches, because we only considered one spectrum (SL1). This spectrum only covers a range between 7.5 and 15 μm . Finally, the spectra are shifted to the rest frame according to the distances of the objects (see Column (3) in Table 1).

Table 2
Integrated Fluxes and EWs for the Nuclear and *Spitzer* Spectra

Object	Fluxes (10^{-13} erg s $^{-1}$ cm $^{-2}$)				EW (10^{-3} μ m)			
	PAH $_{11.3}$ μ m		[S IV] $_{10.5}$ μ m		PAH $_{11.3}$ μ m		[S IV] $_{10.5}$ μ m	
	Nuclear	Spitzer	Nuclear	Spitzer	Nuclear	Spitzer	Nuclear	Spitzer
NGC 931	<2	–	13 ± 2	–	<1	–	10 ± 2	–
Mrk 1066	82 ± 12	264 ± 40	<0.1	11 ± 2	118 ± 18	158 ± 25	<0.2	19 ± 3
NGC 1320	7 ± 2	–	6 ± 1	–	9 ± 3	–	7 ± 1	–
NGC 1386	<0.3	16 ± 2	17 ± 3	23 ± 4	<1	14 ± 2	28 ± 5	26 ± 4
NGC 1808	154 ± 24	1176 ± 178	<0.1	<7	107 ± 16	167 ± 26	<0.3	<2
NGC 2992	<6	160 ± 25	4 ± 1	10 ± 2	<22	149 ± 25	17 ± 3	19 ± 4
NGC 3081	<0.2	6 ± 2	10 ± 4	29 ± 12	<1	9 ± 2	23 ± 12	39 ± 6
NGC 3081	<0.1	6 ± 1	12 ± 4	29 ± 10	<0.1	9 ± 3	26 ± 8	38 ± 14
NGC 3227	32 ± 5	176 ± 29	10 ± 2	9 ± 3	41 ± 6	119 ± 21	13 ± 2	11 ± 3
NGC 3281	<0.3	<12	10 ± 2	18 ± 5	<0.4	<13	15 ± 2	30 ± 6
NGC 4253	22 ± 3	–	5 ± 1	–	37 ± 6	–	9 ± 1	–
NGC 4569	32 ± 5	–	<0.02	–	115 ± 18	–	<0.1	–
NGC 5135	14 ± 2	–	9 ± 1	–	40 ± 6	–	28 ± 5	–
NGC 5643	5 ± 1	74 ± 11	10 ± 2	15 ± 2	12 ± 2	110 ± 17	29 ± 5	37 ± 6
IC 4518W	<0.1	–	<0.1	–	<0.3	–	<0.2	–
IC 5063	<7	–	9 ± 1	–	<3	–	5 ± 1	–
NGC 7130	39 ± 6	145 ± 22	4 ± 1	6 ± 1	74 ± 11	132 ± 20	12 ± 2	14 ± 2
NGC 7172	<0.5	33 ± 5	2.1 ± 0.4	5 ± 1	<1	70 ± 11	25 ± 4	24 ± 4
NGC 7465	14 ± 2	–	<0.1	–	54 ± 9	–	<0.3	–
NGC 7582	8 ± 1	182 ± 28	<0.1	6 ± 1	27 ± 4	177 ± 28	<0.1	23 ± 4

Note. The symbol “–” indicates that *Spitzer* spectra were not available.

Table 3
PAH and [S IV] Fluxes

Object	Fluxes (10^{-13} erg s $^{-1}$ cm $^{-2}$)							
	PAH $_{11.3}$ μ m				[S IV] $_{10.5}$ μ m			
	100 pc	200 pc	500 pc	700 pc	100 pc	200 pc	500 pc	700 pc
NGC 931	–	–	–	–	21 ± 3	35 ± 6	40 ± 6	–
Mrk 1066	–	160 ± 25	267 ± 41	273 ± 42	–	9 ± 1	12 ± 2	13 ± 2
NGC 1320	–	–	–	–	7 ± 1	8 ± 1	11 ± 2	–
NGC 1386	–	–	–	–	24 ± 4	24 ± 4	–	–
NGC 1808	486 ± 74	1065 ± 161	–	–	–	–	–	–
NGC 2992	–	–	–	–	11 ± 2	13 ± 2	20 ± 3	–
NGC 3081	–	–	–	–	17 ± 3	28 ± 6	–	–
NGC 3081	–	–	–	–	16 ± 3	27 ± 5	–	–
NGC 3227	80 ± 12	121 ± 18	–	–	9 ± 2	12 ± 2	–	–
NGC 3281	–	–	–	–	–	14 ± 2	–	–
NGC 4253	43 ± 7	60 ± 9	64 ± 10	–	6 ± 1	9 ± 1	13 ± 2	–
NGC 4569	307 ± 47	396 ± 61	–	–	–	–	–	–
NGC 5135	4 ± 1	17 ± 3	60 ± 9	88 ± 13	13 ± 2	21 ± 3	32 ± 5	34 ± 5
NGC 5643	26 ± 4	74 ± 11	–	–	13 ± 2	15 ± 2	–	–
IC 4518W	–	–	–	–	–	7 ± 1	10 ± 2	10 ± 2
IC 5063	–	–	–	–	–	15 ± 2	–	–
NGC 7130	–	65 ± 10	90 ± 14	145 ± 22	–	5 ± 1	6 ± 1	6 ± 1
NGC 7172	5 ± 1	11 ± 2	33 ± 5	–	5 ± 1	5 ± 1	5 ± 1	–
NGC 7465	35 ± 5	44 ± 7	–	–	–	–	–	–
NGC 7582	26 ± 4	56 ± 9	179 ± 27	181 ± 28	–	–	–	–

Note. These measurements have been obtained from interpolation at different distances from the nucleus (see text). Note that the symbol “–” indicates that we do not consider the measurement because the interpolated value is within nuclear radii or at larger radii than our outer radius for the sources.

3. Spectral Analysis

Nuclear spectra were first extracted as point-like sources using RedCan pipeline. These spectra show photometric errors typically of 11% in flux for all objects (Alonso-Herrero et al. 2016). We used these spectra as the nuclear component of our radial profile.

Then, in order to analyze the change in the spectrum at different distances from the nucleus and to study the circum-nuclear emission, we have divided the spatial axis of the spectra into apertures at different radii. Thus, each aperture gives the spectrum of the extended emission within this radius, together with the nuclear component. The maximum radius is determined as the largest one where extended emission can be

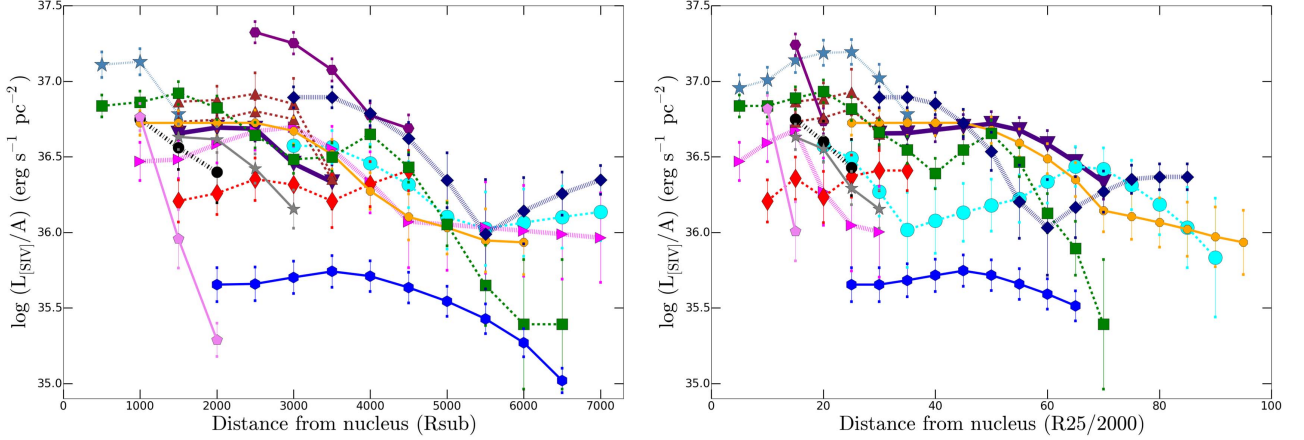


Figure 2. Left: luminosity of the [S IV] line as a function of distance from the nucleus in units of the sublimation radius. Right: luminosity of the [S IV] line as a function of the distance from the nucleus in units of the isophotal radius divided by 2000 for each galaxy. In both figures, the symbols are measurements at fixed distances. The different lines link all the measurements for each object: (1) NGC 931 (steel blue stars), (2) Mrk 1066 (indigo triangles pointing down), (3) NGC 1320 (cyan circles), (4) NGC 1386 (purple hexagons), (5) NGC 2992 (magenta triangles pointing right), (6) NGC 3081 (brown triangles pointing down), (7) NGC 3227 (red thin diamonds), (8) NGC 3281 (black circles), (9) NGC 4253 (orange octagons), (10) NGC 5135 (green squares), (11) NGC 5643 (violet pentagons), (12) IC 4518W (navy blue diamonds), and (13) IC 5963 (gray stars), and NGC 7130 (blue hexagons).

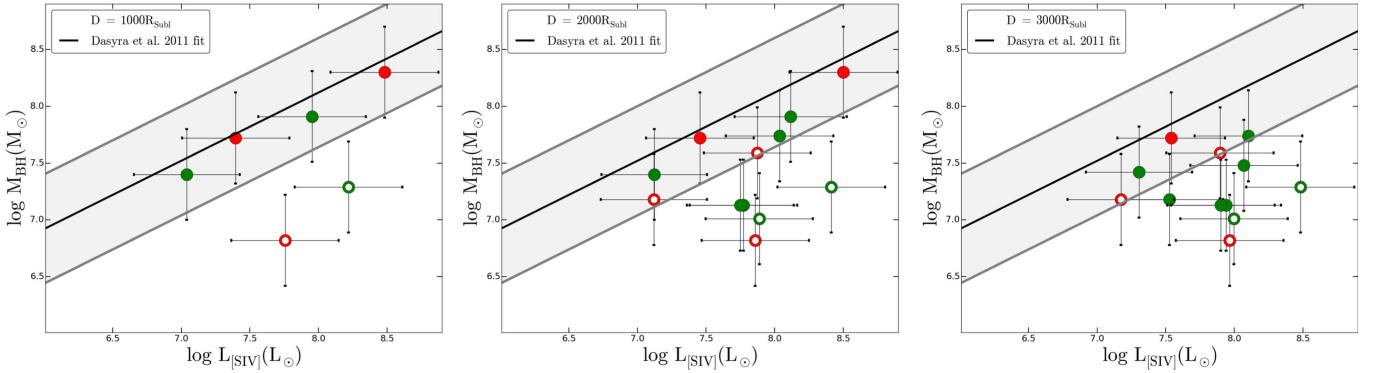


Figure 3. [S IV] line emission luminosity vs. M_{BH} at $1000R_{\text{sub}}$, $2000R_{\text{sub}}$, and $3000R_{\text{sub}}$. The white circles are sources where SF regions were previously reported at these spatial scales. The Sy1 and Sy2 are shown as red and green circles, respectively. The relation found by Dasyra et al. (2011) is shown as a black solid line in all panels.

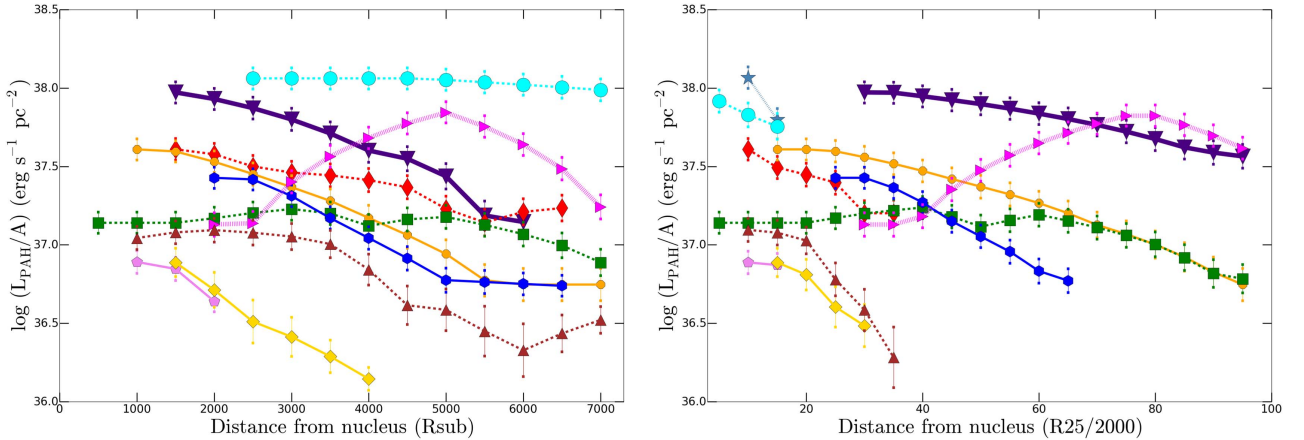


Figure 4. Left: luminosity of the $11.3 \mu\text{m}$ PAH as a function of distance from the nucleus in units of the sublimation radius. Right: luminosity of the $11.3 \mu\text{m}$ PAH as a function of the distance from the nucleus in units of the isophotal radius divided by 2000 for each galaxy. In both figures, the symbols are measurements at fixed distances. The different lines link all the measurements for each object: (1) Mrk 1066 (indigo triangles pointing down), (2) NGC 1808 (steel blue stars), (3) NGC 3227 (red thin diamonds), (4) NGC 4253 (orange octagons), (5) NGC 4569 (cyan circles), (6) NGC 5135 (green squares), (7) NGC 5643 (violet pentagons), (8) NGC 7130 (blue hexagons), (9) NGC 7172 (gold diamonds), (10) NGC 7465 (magenta triangles pointing right), and (11) NGC 7582 (brown triangles pointing up).

seen in the 2D spectra. The aperture increments are fixed to 4 pixels because this matches the FWHM of the average point-spread function in our observations. The extraction has been

done using the extended source mode provided by RedCan. The minimum radius of the apertures is calculated as the first aperture where the $12 \mu\text{m}$ continuum flux is greater (or equal)

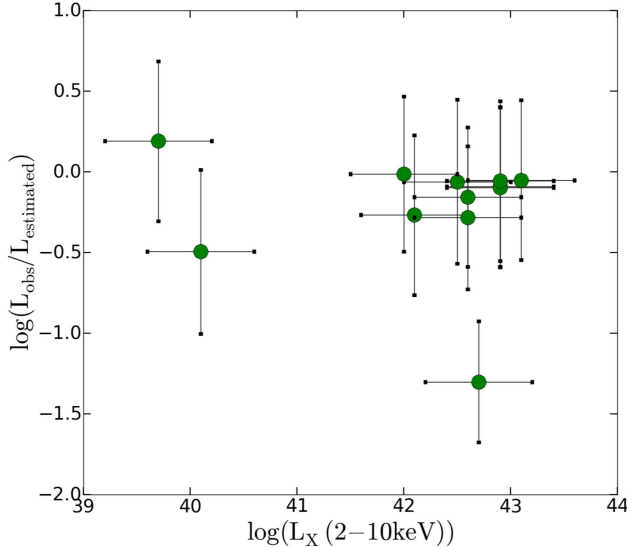


Figure 5. X-ray luminosity vs. PAH luminosity deficit (see text). This deficit is measured as the ratio between the observed and the expected one. The expected PAH luminosity expected is estimated as the linear extrapolation to the center of the radial profile within 200 pc.

than the nuclear continuum flux.¹¹ Table 1 (Column (11)) reports the minimum (i.e., nuclear component extracted as point-like source) and maximum radius used for the extended profiles in units of pc. We are tracing minimum (maximum) extensions of ~ 20 pc (~ 1 kpc) in the spatial direction of the 2D spectra.

Since we use T-ReCS/CanariCam and *Spitzer*/IRS spectra together, we have studied the flux cross-calibration from both instruments, for which we have measured the 12 μm continuum flux. We computed a 12 μm radial continuum profile including both T-ReCS/CanariCam and *Spitzer* fluxes (see Section 3.2 for more details about radial profiles). Then, we investigated whether the *Spitzer* flux follows the extrapolation of the T-ReCS/CanariCam radial profile. We found that *Spitzer* spectra (in the sources where it was used) do not extrapolate naturally from the radial distribution observed in high spatial resolution spectra. In five cases, the 12 μm continuum flux for *Spitzer* data is higher than that of ground-based spectra, and in the other six cases, it is lower. A larger integrated *Spitzer* flux than that predicted by the extrapolation of the ground-based spectra is expected because they cover a different area although mapping the same aperture (3.7×3.7 arcsec 2 and slit width $\times 3.7$ arcsec 2 for *Spitzer* and ground-based data, respectively). Lower integrated *Spitzer* flux is most certainly due to flux calibration uses in the ground-based spectra due to the highly variable sky. In order to correct this cross-calibration problem, we implemented a recalibration of the T-ReCS/CanariCam data for each source. This calibration was implemented as a scaled value for each source as the difference between the extrapolation of the fluxes given in the T-ReCS/CanariCam radial profiles and the *Spitzer* flux at 12 μm . We then multiply the T-ReCS/CanariCam fluxes by this value (see Column (8) in Table 1). Note that the scaled value is not within the reported error range for the *Spitzer* or T-ReCS/CanariCam

¹¹ The nuclear continuum is extracted as a point source using the trace of the standard star (see González-Martín et al. 2013, for more details).

data. However, the correction applied is in general very small ($|F_{12\ \mu\text{m}}(T - \text{ReCS}/\text{CanariCam})/F_{12\ \mu\text{m}}(\text{Spitzer})| \sim 1.3$).

In Figure 1 (bottom) we show NGC 7130 as an example of the data presented in this paper. This example clearly shows the PAH feature at 11.3 μm and the [S IV] line in 10.5 μm . A similar figure for each object in our sample is included in the Appendix.

3.1. PAH Feature and [S IV] Line Measurements

There are several methods to measure the fluxes of the PAH features. The best approach depends on the spectrum characteristics. For instance, PAHFIT (Smith et al. 2007) and DecomIR (Mullaney et al. 2011) are able to measure the PAH features and are very useful when the spectra are highly contaminated by their host galaxy emission. However, they require a wide spectral coverage in order to produce satisfactory results—larger than that of the T-ReCS or CanariCam spectra presented here (see Esquej et al. 2014). Instead, we followed the procedure described by Alonso-Herrero et al. (2014) and Esquej et al. (2014) to measure the flux and the equivalent width (EW). They use the method described by Hernán-Caballero & Hatziminaoglou (2011), which is well suited for limited wavelengths (case of [S IV] line) or weak PAHs. Their method sets a local continuum by interpolating from two narrow bands (i.e., 10.7–10.9 μm and 11.7–11.9 μm) at both sides of the PAH feature or at both sides of the [S IV] line emission (i.e., 10.35–10.40 μm and 10.65–10.75 μm). Note that we selected these continuum ranges individually according to the particularities of each spectrum. This was done to optimize the measurement of the bands according to the natural width of the PAH feature. After subtracting the underlying continuum, residual data were fitted using a Gaussian profile. We compared the fluxes obtained from the Gaussian fit and the direct integration in the case of the nuclear spectra. The discrepancy in the flux between the two methods for the nuclear spectrum is on average less than 3% and 7% for the PAH feature and the [S IV] line, respectively.

Then, the EW of the lines is measured by dividing the integrated flux by the interpolated continuum flux at the center. The uncertainties are obtained by Monte Carlo simulation using the calculated dispersion around the flux measurements. We have applied a smoothing to the high spatial resolution spectra to improve the signal-to-noise ratio of the features. This smoothing was applied to the data using the average of three near spectral bins. The smoothing causes a peak dilution, which could dilute the emission lines if they are less than three points. Nevertheless, the lines that we studied are broad; therefore, we do not expect to have any significant effect on the results (see Alonso-Herrero et al. 2014, for more details on the smoothing technique). Table 2 shows integrated fluxes and EW measurements from each emission obtained with the nuclear and *Spitzer*/IRS spectra.

3.2. Surface Brightness Radial Profiles

We create surface brightness and EW radial profiles¹² for each object. We first extracted the flux at the radius of each aperture, and then we subtracted that of all inner apertures to get the flux of a ring. When the subtracted measurement was

¹² We use the term “radial profile” for referring to the surface brightness radial profiles.

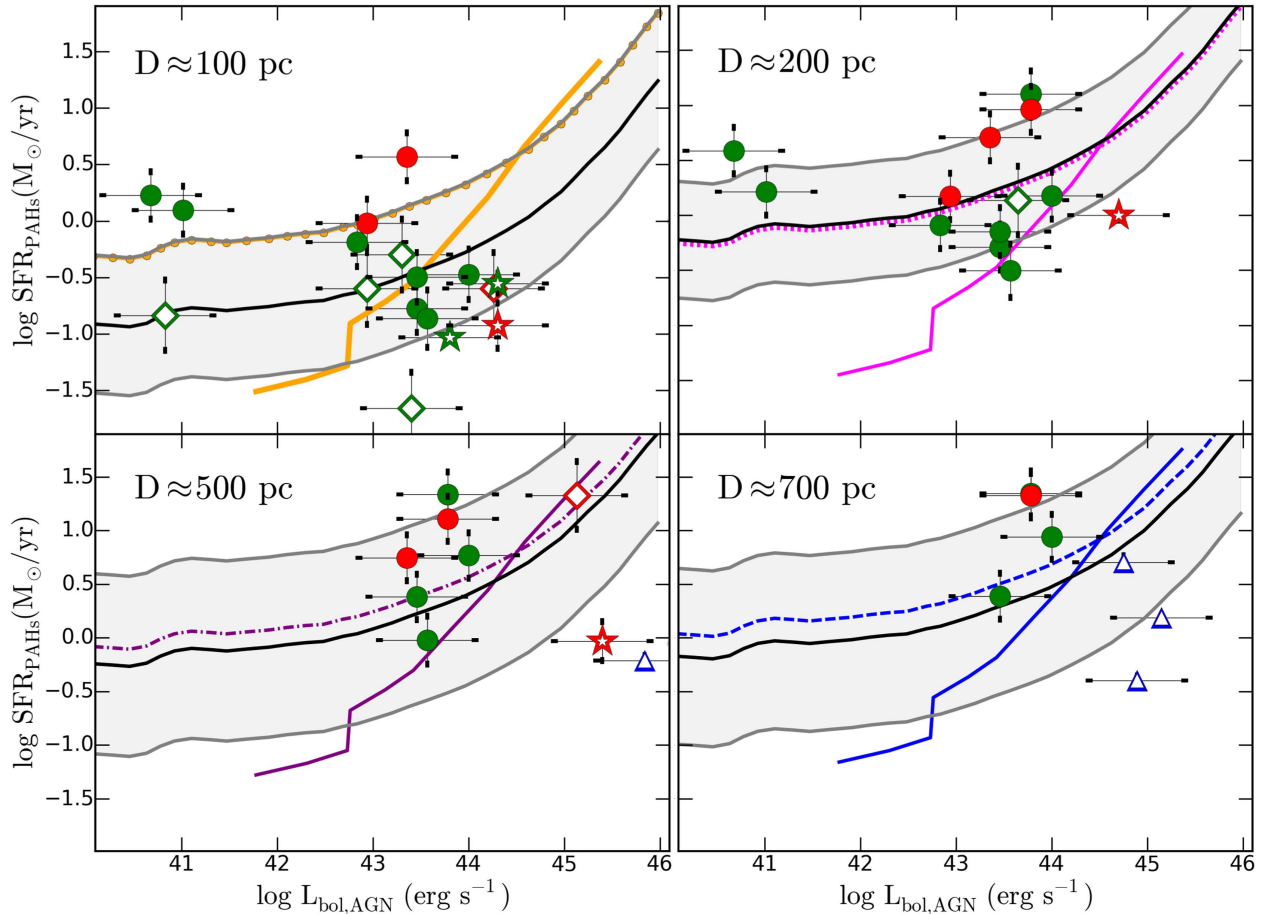


Figure 6. SFR vs. bolometric AGN luminosity at different distances. Each panel corresponds to the integrated SFR_{PAHs} for the 100, 200, 500, and 700 pc apertures, respectively. The QSO observations from Martinez-Paredes et al. (submitted) are shown as blue triangles. The Seyfert galaxies from Esquej et al. (2014), Ruschel-Dutra et al. (2017), and our work are shown as stars, diamonds, and circles, respectively. The Sy1 and Sy2 are shown as red and green circles, respectively. The dashed and solid lines in all panels correspond with the correlations proposed by Neistein & Netzer (2014) as a function of radius shifted using the predictions given by Hopkins & Quataert (2010) (see text). The dashed line is the simulated SFR value for a given $L_{bol,AGN}$, and the solid line corresponds to the average $L_{bol,AGN}$ for a given value of SFR according to Neistein & Netzer (2014). The black solid line and the shaded area in each panel show the average and standard deviation of the best shift to the relation predicted by Neistein & Netzer (2014), respectively.

Table 4
Comparison with Models by 11.3 μm PAH

Distance	Theory	Measurement	
		Mean	σ
100 pc	1.00	1.09	0.60
200 pc	1.06	0.88	0.70
500 pc	1.23	0.91	0.75
700 pc	1.35	0.95	0.80

Note. For the PAH feature, we have computed the observed shift for the relation as the average and standard deviation of the relation predicted by Neistein & Netzer (2014). For more information see Section 5.2.

lower than 3σ , we considered it as a limit. We then divided each value by its respective area to correct for different aperture radii. In the case of the nucleus, the area is computed with the radius of the unresolved emission times the slit width. For the rest of the apertures, the area is calculated as the slit width times increment radius for the aperture (i.e., 2 pixels; see Table 1, Column (7)).

Figure 1 (bottom) shows the radial profile for the PAH feature at 11.3 μm (blue diamonds) and [S IV] line emission at

10.5 μm (orange circles). The Appendix includes the radial profiles for the full sample (see Figures 7–26).

In order to analyze the behavior of the two emission features across the full sample, we calculated the integrated flux at fixed physical scales: 100, 200, 500, and 700 pc. The measurements were calculated from a linear interpolation between the nearest points. Notice that we do not take into account the nuclear measurement to compute these values at a fixed distance. These measurements are reported in Table 3. We report measurements only when our radial profile includes these distances.

4. The Origin of the [S IV] Line Emission

The [S IV] is an emission line typically observed in the planetary nebula, H II regions, and ULIRGs (Rank et al. 1970; Holtz et al. 1971; Gillett et al. 1972), as well as AGNs. The origin of the nuclear [S IV] line emission is controversial in the case of AGNs. It can be produced in the NLR and therefore can be a good tracer of gas ionized by the AGNs (Dasyra et al. 2011). However, it can also be related to star-forming regions owing to its relatively low excitation potential (Diaz-Santos et al. 2010; Pereira-Santaella et al. 2010).

Diaz-Santos et al. (2010) studied four LIRG-type objects, finding that half of the [S IV] line emission flux comes from the nucleus. Our sample has three objects in common with theirs (NGC 5135, IC 4518W, and NGC 7130). For NGC 5135 they found that $\sim 40\%$ of [S IV] line emission integrated flux comes from the nuclear spectrum. Fairly consistent with that, we find that the nuclear spectrum contributes $\sim 35\%$ to the integrated flux of this emission line. They found that the [S IV] nuclear flux in IC 4518W is smaller than the emission in the integrated spectrum by $\sim 22\%$. We also agree that there is an excess of [S IV] emission at 0.5 arcsec (~ 200 pc), which is unrelated to the excess of $11.3 \mu\text{m}$ PAH emission. Diaz-Santos et al. (2010) suggested that this emission is associated with the central AGN. In NGC 7130 we found that 70% of the [S IV] flux comes from the nuclear spectrum, while Diaz-Santos et al. (2010) found that the [S IV] nuclear emission corresponds to 50% of the total flux. In both IC 4518W and NGC 7130, star-forming regions near the nucleus have been found (see the Appendix). Based on the *Spitzer* observations, Pereira-Santaella et al. (2010) could not conclude whether the [S IV] line emission is related to star-forming regions for this object owing to poor data quality. However, they found that extended emission of the [S IV] line can be attributed to star-forming regions, using $\text{Pa}\alpha$ and $\text{H}\alpha$ images for the other three objects of their sample.

We explored the luminosity of the [S IV] emission line ($L_{[\text{S IV}]}$) in the AGN environment by studying the radial profiles of $L_{[\text{S IV}]} / L_{\text{Edd}}$ as a function of the sublimation radius (R_{sub} ; Nenkova et al. 2008). The latter was computed as

$$R_{\text{sub}} \simeq 0.4 \left(\frac{L}{10^{45} \text{ erg s}^{-1}} \right)^{1/2} \left(\frac{1500 \text{ K}}{T_{\text{sub}}} \right)^{2.6} \text{ pc}, \quad (1)$$

where is assumed to be $T_{\text{sub}} = 1400 \text{ K}$.

We interpolated the given values of $L_{[\text{S IV}]}$ to obtain measurements at the following distances from the nucleus: (1000, 2000, 3000, 4000, 5000, 6000, 7000) R_{sub} . This allowed us to compare the $L_{[\text{S IV}]}$ at the same spatial scales. Figure 2 (left) shows the radial profiles of the $L_{[\text{S IV}]}$ as a function of R_{sub} using the new measurements for the 13 AGNs in our sample where we detected the [S IV] emission line in more than two apertures. The number of values included in the radial profiles varies owing to the minimum and maximum distances from the nucleus that we can trace. In general, the radial profiles in Figure 2 (left) show a chaotic behavior. It might be plausible that these profiles strongly depend on the gas suppliers around each AGN, adding scatter to the expected behavior. The proper comparison between available gas around AGNs and the [S IV] emission needs to be studied prior to any further conclusions. Figure 2 (right) shows the radial profiles of the [S IV] line as a function of isophotal radius (R_{25}) of the galaxy.¹³ We found a similar chaotic behavior.

Dasyra et al. (2011) used the [Ne V], [O IV], [Ne III], and [S IV] line emissions to study the kinematics of the NLR. They concluded that the M_{BH} and the gas velocity dispersion are related to the luminosity of these emission lines originating in the NLR. We studied the relationship between M_{BH} and the luminosity of the [S IV] line emission ($L_{[\text{S IV}]}$) to interpret the origin of the line. Figure 3 shows this relation at $1000R_{\text{sub}}$, $2000R_{\text{sub}}$, and $3000R_{\text{sub}}$ for the sources where we detected the

¹³ The isophotal diameter of a galaxy is the decimal logarithm of the length of the projected major axis of a galaxy at isophotal level 25 mag arcsec⁻² in the B band. See <http://leda.univ-lyon1.fr/leda/param/logd25.html>.

[S IV] line emission at these scales. The solid line corresponds to the Dasyra et al. (2011) relation:

$$\log(M_{\text{BH}}) = 0.6 \times \log(L_{[\text{S IV}]}) + 3.32. \quad (2)$$

This relation is based on the best fit for their AGN sample using *Spitzer*/IRS spectra and considering that the [S IV] line emission only comes from the NLR. The rms scatter computed for this relation is 0.48 dex (shaded area in Figure 3). For a few sources without significant SF, the [S IV] line fluxes follow the Dasyra et al. (2011) relation at scales of $\sim 1000R_{\text{sub}}$. However, the sources move away from the relation with increasing distance from the nucleus. This result could be interpreted as H II regions, planetary nebulae, or blue compact dwarfs contributing to the sulfur excitation, along with the AGNs (Groves et al. 2008).

Even if the nuclear [S IV] line emission could arise from photoionization by the AGNs in some of our sources, it could be strongly suppressed by dust because it is inside the broad $9.7 \mu\text{m}$ silicate absorption feature (Pereira-Santaella et al. 2010). Therefore, it could not be an isotropic measurement of the AGN luminosity. Moreover, the obscuration of the internal parts of the AGN by the dusty torus could also play a major role in the [S IV] line emission attenuation. This could be the case for NGC 7172, showing a large value of the $9.7 \mu\text{m}$ optical depth ($\tau_{9.7 \mu\text{m}} = 1.9$; González-Martín et al. 2013). Indeed, a very weak detection of the [S IV] line emissions has been found for this object. We have considered the possibility that attenuation is affecting the [S IV] line emission in the inner parts. We found a deficit between nuclear and the first apertures in five sources (see the Appendix). We have compiled the nuclear $\tau_{9.7 \mu\text{m}}$ from González-Martín et al. (2013) and Alonso-Herrero et al. (2016), but we did not find any relation between the $\tau_{9.7 \mu\text{m}}$ and the deficit on the [S IV] line emission flux. Also, Dasyra et al. (2011) found that this obscuration does not significantly affect the relative flux of MIR lines. In summary, in 6 of the 13 sources we did not observe a common decrease in the radial profile, as we would expect if this line were caused by AGN photoionization.

4.1. The [S IV] Emission Line versus the $11.3 \mu\text{m}$ PAH Feature

The [S IV] emission line could be produced by star-forming regions. If this is the case, we would expect a close resemblance between the [S IV] and PAH radial profiles at these radii.

We compared nine sources where the radial profiles of both the PAH feature and the [S IV] line show more than one measurement at different distances from the nucleus. In all sources, the radial profile for both emissions shows a complex behavior. In six¹⁴ of these nine sources it is clear that the behaviors of the radial profiles of both emissions are not related to each other at any distance. Even with that, it could be the case that the star-forming regions traced by the $11.3 \mu\text{m}$ PAH feature are not the same as those that give origin to the [S IV] emission in the majority of the sources. A plausible explanation is that both emissions are tracing different stages of SF and thus different degrees of ionizing fluxes. Ideally, to distinguish the type of stars that contribute to the [S IV] line emission, high spatial resolution images of [S IV] line emission, together with

¹⁴ NGC 2992, NGC 3227, NGC 5135, NGC 5643, NGC 7172, NGC 7465.

other tracers of SF related to different stages of the SF activity, would be needed.

5. The Behavior of the PAH Emission Feature

In this section, we review the plausible dilution/destruction of PAHs in the innermost parts of the AGN (Section 5.1), and we use PAHs as tracers of SF to study the coevolution of the AGN and its host galaxy (Section 5.2).

5.1. On the Dilution/Destruction of the Nuclear PAHs

The relation between the strength of the PAHs and IR luminosity is weak or absent in galaxies with AGNs (Siebenmorgen et al. 2004; Weedman et al. 2005). An important implication of this is that PAHs might not be used as star-forming tracers in the surroundings of the nucleus because they can be destroyed by the AGN radiation field (Siebenmorgen et al. 2004). The AGN can directly modify PAH grain size distribution and even serve as the excitation source for some PAH emission (Genzel et al. 1998; Laurent et al. 2000; Smith et al. 2007). On the other hand, PAHs could survive because they are shielded from the AGN radiation (Goulding et al. 2012). Even more extremely, PAH could be induced by the AGN radiation field (Jensen et al. 2017). Diamond-Stanic & Rieke (2010) found that the 6.2, 7.7, and 8.6 μm PAH features are suppressed with respect to the 11.3 μm PAH feature in local Seyferts. They speculate that destruction of these features might be related to the fact that they are produced by the smallest aromatic molecules and, therefore, more easily destroyed. Following this argument, the molecules responsible for 11.3 μm PAH emission could survive because they are more difficult to destroy. Already from *IRAS* data, it was pointed out that the emission at the 12 μm band fits very well the predictions that follow from the emission modeling of transiently heated PAH molecules (Dultzin-Hacyan et al. 1990). More recently, Diamond-Stanic & Rieke (2012) found a correlation between the nuclear SF (<1 kpc) and SMBH accretion rate, where the nuclear SF is traced by the PAH at 11.3 μm aromatic feature.

We detected the PAH feature at 11.3 μm in 15 out of the 19 objects in our sample ($\sim 90\%$ of our sources), and 10 of these sources show nuclear PAHs ($\sim 58\%$ of our sample). The 11.3 μm PAH feature was measured in more than one aperture in 11 objects along the radial profiles.¹⁵ We found that in eight sources (except NGC 5643, NGC 7172, and NGC 7582) the nuclear EW of the PAH is larger than the one found in the first aperture.¹⁶

In Figure 4, we show the radial profiles of the $L_{11.3 \mu\text{m}} \text{PAH}$ as a function of R_{sub} (left) and $R_{25}/2000$ (right). This figure is similar to Figure 2 from the previous section. We observed a complex behavior. Increments and decrements at different distances were found.

Regarding the 11.3 μm PAH, nuclear fluxes are larger than those of the first aperture only in NGC 1808 and NGC 5135. The unresolved nucleus shows lower flux than the first-aperture PAH flux in most of our cases (7 out of 12, i.e., 60%). When observed, this decrement is seen within ~ 100 pc. Note that in

¹⁵ Another four objects of the sample show emission only in one aperture (NGC 1386, NGC 2992, NGC 3081, and IC 4518W). The other four sources do not show detection of the 11.3 μm PAH feature.

¹⁶ Note that we do not take into account IC 4518W because the measurements at distances < 400 pc are only upper limits.

many cases we do not see a decrease in the radial profile (as, e.g., in NGC 7582), but a drop between the nuclear and the first aperture (e.g., NGC 7172). Therefore, this decrement could be affecting even lower spatial scales. The explanations of this decrement are (1) PAH dilution by AGN continuum,¹⁷ (2) PAH destruction by the radiation field, (3) lack of the inner SF, and (4) the existence of a nuclear ring. In the following we discuss these four possibilities.

Alonso-Herrero et al. (2014) suggested that the apparent decrease in the EW of the PAH feature is an effect of the dilution of the PAH feature by the strong continuum of the AGN in the nuclear apertures. They indeed recovered an increase on the nuclear PAH flux toward the center in their sample of six local AGNs. Meanwhile, the EW of the PAH feature showed an apparent decrease. We have not found a similar behavior in any of our objects, but we only have one object in common with their analysis (MRK 1066). They computed the radial profile in isolated apertures at different distances from the nucleus. In our analysis, we have extracted spectra centered at the nucleus with different radii. Thus, each of our apertures includes the nuclear emission. In order to study the radial profile, we subtracted the previous inner aperture scaled to the area (see Section 3). This way, we avoided the dilution due to this effect. Thus, dilution cannot play a role in the lack of nuclear PAHs in the sources analyzed here.

Siebenmorgen et al. (2004) suggested that the suppression of PAH emission near the AGN may be due to the destruction of PAHs by the strong radiation field of the AGN. If this is the case, we would expect a relation between the PAH luminosity deficit and the X-ray luminosity as a tracer of the AGN bolometric luminosity. The stronger the AGN radiation field, the larger the nuclear PAH deficit. We have measured the PAH luminosity deficit from our radial profiles as the ratio between the expected and the observed one. We have estimated the expected nuclear PAH luminosity in two ways: (1) as the linear extrapolation of the radial profile within 200 pc, and (2) as the maximum of PAH emission within 200 pc. Figure 5 shows the deficit obtained by extrapolation versus the X-ray luminosity. We do not find a relation between the PAH deficit and the AGN X-ray luminosity. Thus, from our data we have not found observational support for the destruction of the PAH features due to the AGN radiation field. However, we cannot rule out this hypothesis since more sensitive and better-resolution observations are needed. For instance, higher spatial resolution spectra could help pinpoint the distance from the nucleus at which the PAH emission starts to show this deficit. In this sense it might be possible that the relation is missing owing to a poor estimate of the PAH luminosity deficit.

Of course, a natural explanation of this inner deficit in the PAH feature is that there is a lack in SF toward the center. This is supported by the scenario in which the high-velocity winds or AGN-driven massive molecular outflows could be able to quench the surrounding SF (Cicone et al. 2014; McAlpine et al. 2015; Wylezalek & Zakamska 2016). Another possible explanation for this deficit in PAHs in internal parts can be related to the dust/gas distribution, which is ring-like rather than disk-like at the center (e.g., Ohsuga & Umemura 1999; Yankulova 1999). In order to corroborate this, other measurements of the nuclear tracers of the SF must be compared with

¹⁷ We refer to dilution as a decrease in equivalent width from the PAH feature due to the strength of the AGN continuum.

our PAH nuclear fluxes, isolating nuclear and circumnuclear emission.

5.2. Hints on the Coevolution of the AGN and Its Host Galaxy

Hopkins & Quataert (2010) and Neistein & Netzer (2014) have explored the correlation between BH accretion rate and the SFR through hydrodynamic simulations and semianalytic models, respectively. Hopkins & Quataert (2010) predicted the relation between BH accretion rate and SFR at different galactic scales. Their simulations start with a major galaxy merger of isolated bar-(un)stable disk galaxies. They found that nuclear SF is more coupled to AGNs than the global SFR of the galaxy. Neistein & Netzer (2014) developed similar simulations including advection-dominated accreting flow to account for the accretion processing low-luminosity AGNs. They observed a lack of correlation between SFR and AGN luminosity (related to BH accretion rate) at $z < 1$ and $L_{\text{bol,AGN}} < 10^{44} \text{ erg s}^{-1}$ (see also Rosario et al. 2012). They justified this possible lack of correlation as follows: (1) secular SF is perhaps not associated with BH accretion, or (2) BH accretion rate and SFR could be delayed, removing any correlation (see also Hopkins 2012). They also found that AGNs with low or intermediate luminosity might be associated with minor merger events.

In this work we compare Hopkins & Quataert (2010) and Neistein & Netzer (2014) predictions with our results. We derived nuclear and circumnuclear SFRs using the PAH $11.3 \mu\text{m}$ feature luminosities ($L_{11.3 \mu\text{m}}$) and applying the relation derived in Shipley et al. (2016) (using *Spitzer* measurements of 105 galaxies):

$$\begin{aligned} \log \text{SFR} (M_{\odot} \text{ yr}^{-1}) = & (-44.14 \pm 0.08) \\ & + (1.06 \pm 0.03) \log L_{11.3 \mu\text{m}} (\text{erg s}^{-1}). \end{aligned} \quad (3)$$

The uncertainties in the derived SFRs using Equation (3) are typically 0.14 dex (see Shipley et al. 2016, for full details). As a caveat on the use of the PAH as a tracer of SF, Jensen et al. (2017) recently found that the slopes of the radial profile of the PAH emission are very similar, with a strength proportional to the AGN luminosity. They argue that this might imply that a compact emission source is required to explain the common slopes. Both an AGN and a nuclear star cluster are possible sources of PAH heating/excitation. Although we obtain in general a decrease of the PAH flux with the radius, a more complex behavior (with a deficit at the nuclear and peaks of emission on top of a general decrease) is observed in most of our sources, indicating in situ PAH heating.

This is not the first time such a comparison has been done. Esquej et al. (2014) used a sample of 29 nuclear spectra to explore the same relation between SFR and BH accretion rate. They compared their data with the relations obtained by Hopkins & Quataert (2010), and they concluded that predictions for distances (D) < 100 pc reproduce their data well. We have seven sources in common with their sample.¹⁸ Our measurements show slightly higher SFR compared to theirs (factor of 2), perhaps due to a different methodology for defining the continuum around the PAH feature. Ruschel-Dutra

et al. (2017) also analyzed the presence of circumnuclear SF in a sample of 15 AGNs using MIR images (with two filters centered at the $11.3 \mu\text{m}$ PAH features and at the adjacent continuum, respectively). They compared their data with the correlation presented by Neistein & Netzer (2014). They concluded that SFR is correlated with bolometric AGN luminosity ($L_{\text{bol,AGN}}$) for objects with $L_{\text{bol,AGN}} \geq 10^{42} \text{ erg s}^{-1}$, while the low-luminosity AGN has larger SFR for their $L_{\text{bol,AGN}}$.

Compared to previous works, our analysis has the advantage that it allows us to explore the SFR at different subkiloparsec scales from the nucleus. We calculate the $L_{\text{bol,AGN}}$ from X-ray luminosities (reported in Table 1, Column (4)) using the relation $L_{\text{bol,AGN}} = kL(2\text{--}10 \text{ keV})$, where the bolometric correction (k) depends on $L(2\text{--}10 \text{ keV})$ itself with a fourth-order polynomial (see Marconi et al. 2004). In Figure 6, we present the relation between $L_{\text{bol,AGN}}$ and SFR_{PAHs} integrated at different distances from the nucleus. Each panel corresponds to integrated SFR_{PAHs} for the 100, 200, 500, and 700 pc apertures, respectively. Note that this plot includes the 12 sources where we measure the $11.3 \mu\text{m}$ PAH feature (the integrated fluxes density are reported in Table 3). The number of sources varies for each plot depending on the resolution and spatial scale of the extended emission for each spectrum. Furthermore, Sy1 and Sy2 are shown as red and green circles, respectively. We also include the measurements for QSOs from Martinez-Paredes et al. (submitted; triangles), as well as Seyferts from Esquej et al. (2014; stars) and Ruschel-Dutra et al. (2017; diamonds).

Two of our objects (NGC 1808 and NGC 4569) are in the range of low luminosities ($L_{\text{bol,AGN}} < 10^{42} \text{ erg s}^{-1}$). Hopkins & Quataert (2010) predictions are not able to reproduce these low-efficiency objects. Ruschel-Dutra et al. (2017) suggest that the low-luminosity AGNs have high circumnuclear SF. However, our objects with high luminosity have similar or higher SFRs. Neistein & Netzer (2014) presented two correlations: (1) the average SFR value for a given $L_{\text{bol,AGN}}$ in their models, and (2) the average of $L_{\text{bol,AGN}}$ for a given value of total SFR. Indeed, the first relation flattens toward low luminosities, as seen by our two low-luminosity AGNs. In Figure 6, we show these relations shifted as predicted by Hopkins & Quataert (2010) for different apertures (dashed and solid lines with different colors in each panel):

$$\text{SFR}_{\text{PAHs}}(R < 100 \text{ pc}) = \text{SFR}_{\text{PAHs}}(< 10 \text{ pc}) - 1.0, \quad (4)$$

$$\text{SFR}_{\text{PAHs}}(R < 1 \text{ kpc}) = \text{SFR}_{\text{PAHs}}(< 10 \text{ pc}) - 1.52, \quad (5)$$

$$\text{SFR}_{\text{PAHs}}(\text{total}) = \text{SFR}_{\text{PAHs}}(< 10 \text{ pc}) - 2.52. \quad (6)$$

These relations have been computed using Equations (15)–(18) in Hopkins & Quataert (2010). Note that scatter in these relations is significant. In general terms, these relations have the form

$$\text{SFR}_{\text{PAHs}}(R < R_s) = \text{SFR}_{\text{PAHs}}(< 10 \text{ pc}) - B(R_s), \quad (7)$$

where $B(R_s)$ is a constant that depends on the physical scale. We have interpolated the given values to obtain the expected shifts on the physical scales derived from our analysis (reported in the second column of Table 4).

In order to compare predictions with models, we have computed the observed shift to this relation as the average and standard deviation of the relation predicted by Neistein & Netzer (2014) and our data points. These shifts are reported in

¹⁸ NGC 1808, NGC 3227, NGC 5135, NGC 5643, NGC 7130, NGC 7172, and NGC 7582.

the third and fourth columns of Table 4. This correlation and standard deviations are shown as the black solid line and shaded area in each panel, respectively.

Note that the results shown in Figure 6 could be affected by the following errors: (1) The systematic offset due to the use of different SFR tracers. The dispersion from the correlation used to calculate the SFR from the $11.3\text{ }\mu\text{m}$ PAH feature is similar to that obtained by other tracers. We have taken into account this dispersion in the error bars in Figure 6. (2) Timescale for the SF. According to Neistein & Netzer (2014), a necessary condition for agreement between data and model is that the correct timescale for both SF and AGN activity is adopted. The models are constrained to calculate the SFR average using only the SF in the last 150 Myr. We have calculated the SFR using the $11.3\text{ }\mu\text{m}$ PAH as a tracer. This feature is usually associated with B stars (Peeters et al. 2004). (3) Calculation errors in the $L_{\text{bol,AGN}}$. In the models the $L_{\text{bol,AGN}}$ depends on the accretion mass, while in our data it depends on the X-ray luminosity, which might vary up to one order of magnitude. In Figure 6, we have already included this uncertainty in the error bars.

We found a sensible agreement between the theoretical relations proposed by Neistein & Netzer (2014) shifted according to Hopkins & Quataert (2010) and our data, for most inner galaxy parts. This result is of interest, as, in the simulated objects, major mergers with tidal events have been deemed responsible for both the SF and BH feeding.

6. Summary and Conclusions

In this paper, we present a sample of 19 local AGNs observed with ground-based T-ReCS/Gemini and CanariCam/GTC spectra. We complemented these observations with available *Spitzer*/IRS spectra. We have studied the surface brightness radial profile of the $11.3\text{ }\mu\text{m}$ PAH feature and the [S IV] line emission. According to the results of this research, we tried to answer the following three questions:

- (1) What is the origin of the [S IV] line emission in the nuclear region?

The contribution to the [S IV] line emission is not circumnuclear. Instead, it often peaks at distances greater than $1000R_{\text{Sub}}$ from the nucleus. We have not found a relation between the surface brightness radial profiles of the [S IV] line and the PAH feature at different distances from the nucleus. If the PAH is a good tracer of SF, we speculate that the [S IV] line emission could be tracing SF with different ages than those traced by the PAH feature.

- (2) How good is the $11.3\text{ }\mu\text{m}$ PAH feature as a tracer of SF in the vicinity of the AGN?

We found a PAH flux deficit closer to the AGN as compared with larger apertures (toward the inner $\sim 100\text{ pc}$). This deficit cannot be related to dilution by the AGN continuum. We have not found observational support for the destruction of PAH features due to the AGN radiation field. Intrinsic lack of SF toward the center is also a plausible explanation.

- (3) What can we say about the connection between SF and AGN activity?

We found a sensible agreement between the expected shift in the $L_{\text{bol,AGN}}$ –SFR theoretical relation proposed by Neistein & Netzer (2014), Hopkins & Quataert (2010), and our observations, for most inner galaxy parts.

The authors thank the anonymous referee for careful reading and constructive suggestion that improved the paper. This scientific publication is based on observations made with the Gran Telescopio CANARIAS (GTC), installed at the Spanish Observatorio del Roque de los Muchachos of the Instituto de Astrofísica de Canarias on the island of La Palma. This work is based in part on observations made with the *Spitzer Space Telescope*, which is operated by the Jet Propulsion Laboratory, California Institute of Technology, under a contract with NASA. D.E.-A. and O.G.-M. acknowledge support from grant IA100516 and IA103118 PAPIIT DGAP UNAM. D.D. and D.E.-A. acknowledge support through grants IN108716 from PAPIIT, UNAM, and 221398 from CONACYT. D.E.-A. acknowledges support from a CONACYT scholarship. A.A.-H. acknowledges support from the Spanish Ministry of Economy and Competitiveness through the Plan Nacional de Astronomía y Astrofísica under grant AYA2015-64346-C2-1-P, which is partly funded by the FEDER program. C.R.-A. acknowledges the Ramón y Cajal Program of the Spanish Ministry of Economy and Competitiveness through project RYC-2014-15779 and the Spanish Plan Nacional de Astronomía y Astrofísica under grant AYA2016-76682-C3-2-P. T.D.-S. acknowledges support from ALMA-CONICYT project 31130005 and FONDECYT regular project 1151239.

Appendix Catalog of Spectra and Reported Nuclear Star-forming Regions

NGC 931 (Mrk 1040) is a barred galaxy (Sbc) with an Sy1 nucleus. Ward & Wilson (1978) found that this galaxy interacts with a satellite galaxy located 10 kpc from NGC 931. We did not find records of SF in other works at the scales traced with our observations.

Mrk 1066 is a starburst galaxy with an Sy2 nucleus. Ramos Almeida et al. (2014) found star-forming knots at $\sim 400\text{ pc}$ of the galaxy center, after subtracting the AGN component. Alonso-Herrero et al. (2014) suggest that close to the center ($\sim 125\text{ pc}$) the near-IR lines are dominated by the AGN processes.

NGC 1320 is an edge-on galaxy with an Sy2 nucleus. This source is a “warm galaxy” with a relatively high IR luminosity (De Robertis & Osterbrock 1986). We did not find records of SF in other works at the scales traced with our observations.

NGC 1386 is an edge-on spiral galaxy with an Sy2 nucleus. Ruschel-Dutra et al. (2014) found that the $11.3\text{ }\mu\text{m}$ PAH feature is more pronounced at distances $\sim 100\text{ pc}$ from the nucleus. They also found that the [S IV] line emission is only detected in the nucleus at distances $< 100\text{ pc}$. Our observations are in agreement with these results. Optical studies show evidence of heavy obscuration (Weaver et al. 1991; Storchi-Bergmann et al. 1996; Rossa et al. 2000).

NGC 1808 is an inclined spiral galaxy with an Sy2 nucleus and a prominent starburst (Veron-Cetty & Veron 1985; Krabbe et al. 1994). Yuan et al. (2010) considered the possibility that the nucleus is an H II region. Asmus et al. (2014) found that star-forming regions dominate the MIR emission within $\sim 200\text{ pc}$.

NGC 2992 is an inclined spiral galaxy (de Vaucouleurs et al. 1991) and located in the interacting system Arp 245. The nucleus of this source is classified as an Sy1.9 in the optical. However, in other works it is classified as Sy1.5 or Sy2 (Gilli et al. 2000; Trippe et al. 2008). Gilli et al. (2000) suggested that

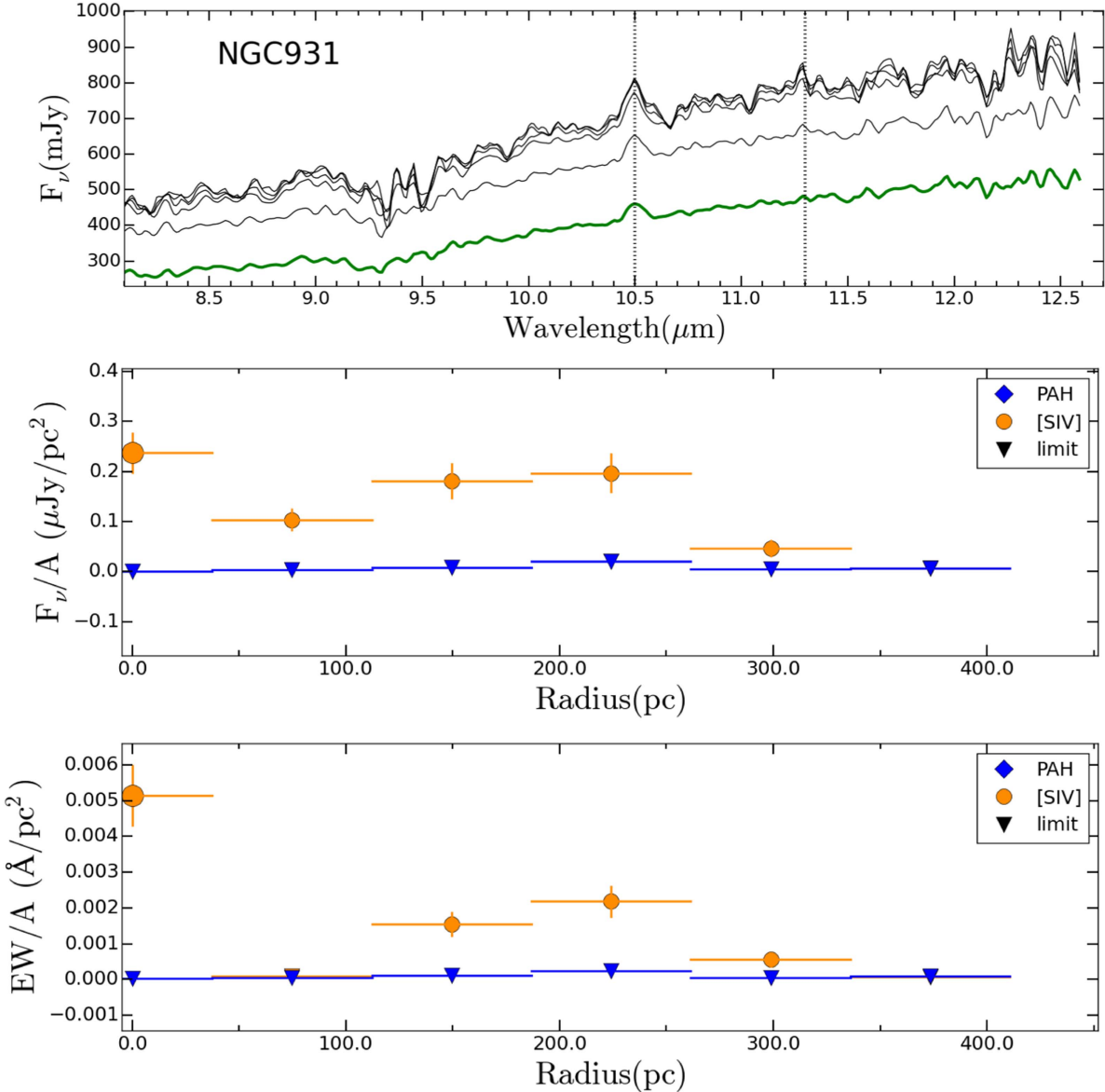


Figure 7. Top panel: extracted spectra at different scales for NGC 931. The green and black lines correspond to the nuclear spectrum and extended aperture spectra, respectively. The dotted lines show the PAH feature and [S IV] line emissions. Middle and bottom panels: surface brightness and EW radial profiles, respectively. The radial profiles for 11.3 μm PAH emission are presented with blue diamonds, while radial profiles for [S IV] line emission are shown with orange circles (the triangles are limit values). The larger circle corresponds to [S IV] emission in the nuclear spectrum. The vertical line marks the 200 pc distance from the center.

the IR variations were probably caused by a retriggered AGN. García-Bernete et al. (2015) found that the starburst component dominates the MIR emission, while the AGN component dominates at higher wavelengths ($\lambda > 15 \mu\text{m}$).

NGC 3081 is a low-inclination barred spiral galaxy with an Sy2 nucleus (Phillips et al. 1983; Asmus et al. 2014). However, Moran et al. (2000) reported a type 1 optical spectrum in polarized light. Weaver et al. (2010) found that the *Spitzer* spectrum exhibits a weak absorption by silicate at 10 μm , a weak PAH emission, and prominent forbidden emission lines. However, Asmus et al. (2014) concluded that the MIR emission is mostly due to the AGN.

NGC 3081: (see above).

NGC 3227 is a low-inclination barred spiral galaxy. This source is in interaction with NGC 3226. The nucleus is

classified as Sy1.5, and it is surrounded by circumnuclear starburst (Véron-Cetty & Véron 2010). Rodríguez-Ardila & Viegas (2003) and Davies et al. (2006) found star-forming regions at ~ 70 pc from the nucleus. Asmus et al. (2014) also found that the MIR emission is dominated by star-forming regions (at arcsecond scale).

NGC 3281 is a highly inclined spiral galaxy with an Sy2 nucleus (Véron-Cetty & Véron 2010). Ramos Almeida et al. (2009) and Sales et al. (2011) presented observations of this source with T-ReCS with the broad N and Qa bands. They found that the spectrum of NGC 3281 shows only a very deep silicate absorption at 9.7 μm and some forbidden emission lines (e.g., [S IV] at 10.5 μm). They conclude that NGC 3281 is a heavily obscured source, due to concentrated dust within a radius of 200 pc.

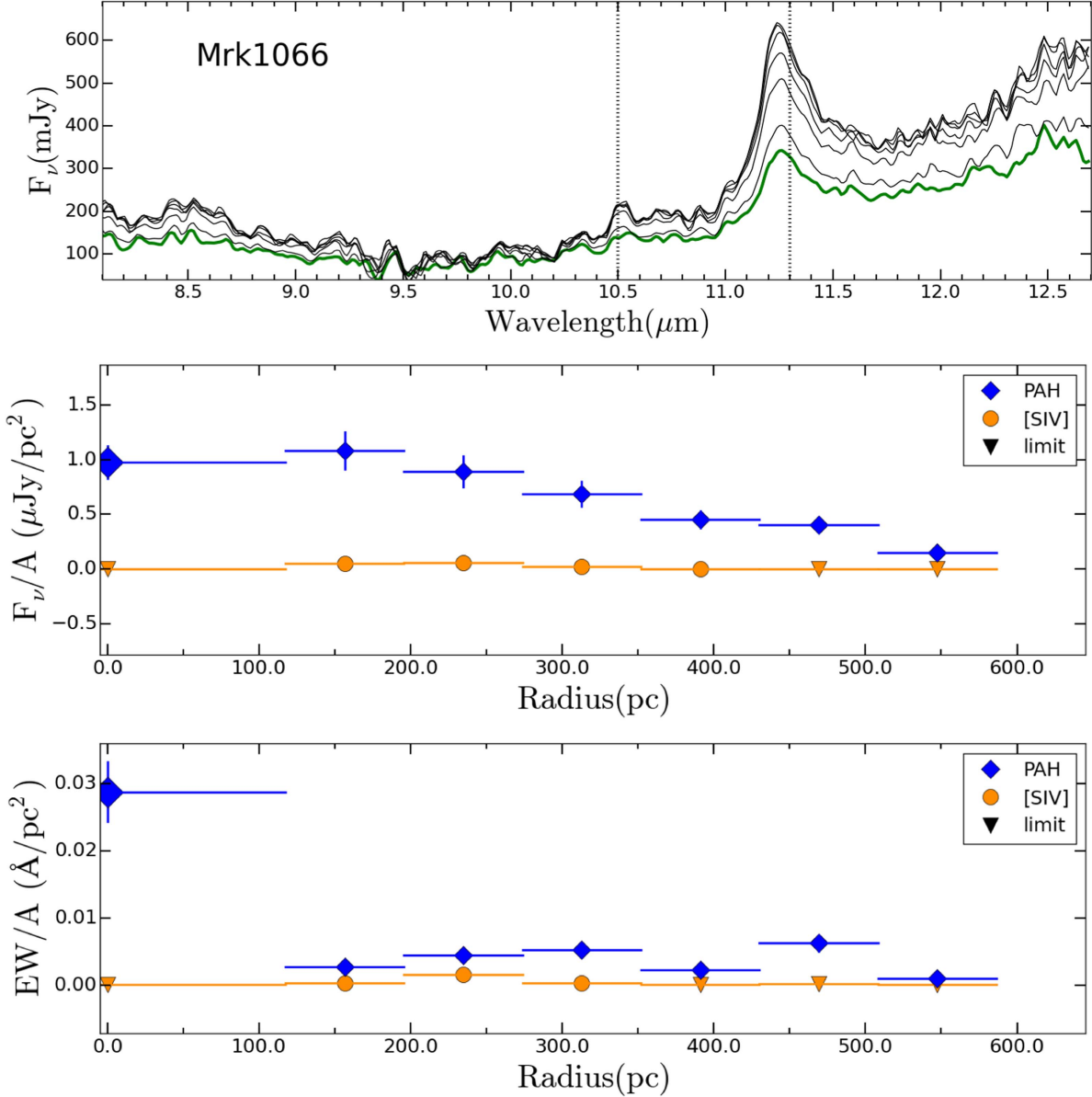


Figure 8. Extracted spectra and radial profiles for Mrk 1066; same description as in Figure 7.

NGC 4253 (Mrk 766) is a barred spiral galaxy (SBa) with an Sy1 nucleus. The *HST* images of this source show some irregular dust filaments around the nucleus (Malkan et al. 1998). Rodríguez-Ardila et al. (2005) studied the near-IR spectrum and found permitted, forbidden, and high-ionization lines. Furthermore, Rodríguez-Ardila & Viegas (2003) found emission in the $3.3 \mu\text{m}$ PAH feature located 150 pc from the nucleus. They considered that this emission is a signature of starburst activity.

NGC 4569 is the most massive, spiral, late-type, and gas-poor galaxy in the Virgo Cluster (van den Bergh 1976). This source shows strong Balmer absorption lines, which could be indicating SF in the last 1.5 Gyr (Ho et al. 2003). Dale et al. (2006) and Mason et al. (2015) also suggested recent and/or ongoing SF activity based on the detection of PAH emission at MIR.

NGC 5135 is an infrared-luminosity, face-on barred spiral galaxy. The nucleus is classified as an Sy2 (Véron-Cetty &

Véron 2010), and it is surrounded by a banana-shaped circumnuclear SF (González Delgado et al. 1998; Bedregal et al. 2009). The inner and outer radii of the SF emission are located at ~ 300 and ~ 750 pc from the nucleus, respectively.

NGC 5643 is a face-on barred spiral galaxy with an Sy2 nucleus (Véron-Cetty & Véron 2010). The IRAC and MIPS images show a compact MIR nucleus embedded within the spiral-like host emission (Asmus et al. 2014). Moreover, the arcsecond-scale MIR spectral energy distribution (SED) is significantly affected by SF (e.g., Shi et al. 2006; Goulding & Alexander 2009).

IC 4518W is a spiral galaxy with an Sy2 nucleus (Véron-Cetty & Véron 2010). Diaz-Santos et al. (2010) and Asmus et al. (2014) found that the SF contribution at subarcsecond resolution is probably minor in its nucleus. Diaz-Santos et al. (2010) found [S IV] line emission at ~ 265 pc toward the north of the nucleus. They suggested that this emission could be related to the NLR.

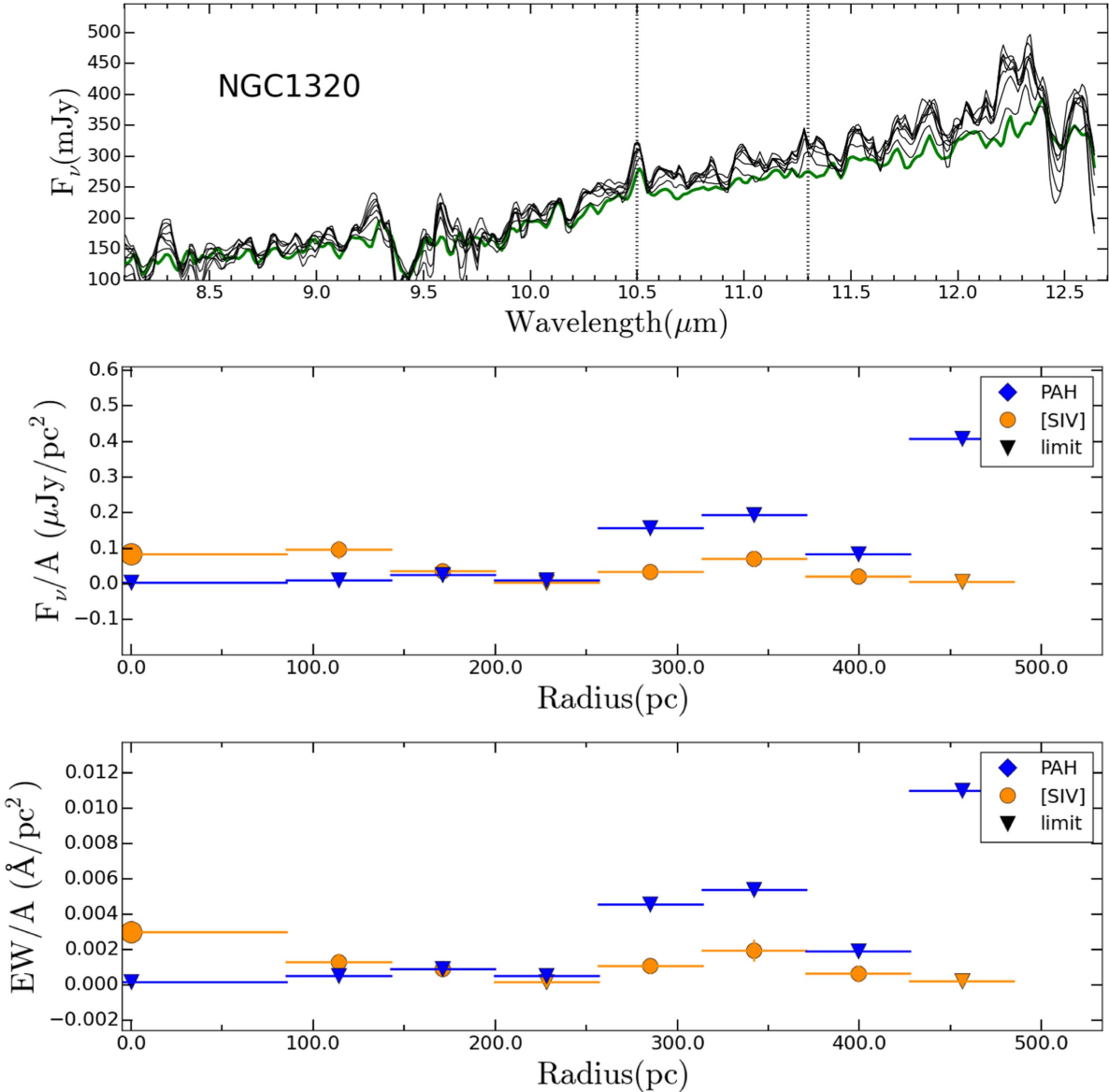


Figure 9. Extracted spectra and radial profiles for NGC 1320; same description as in Figure 7.

IC 5063 is a peculiar galaxy with both spiral and elliptical properties with an Sy2 nucleus (Kewley et al. 2001). Colina et al. (1991) proposed that IC 5063 is a remnant of a recent merger, while Martini et al. (2003) speculated that the nuclear obscuration might be caused by foreground dust lanes. We did not find records of SF in other works at the scales traced by our observations.

NGC 7130 is a peculiar low-inclination spiral galaxy with an Sy1.9 nucleus. A compact starburst is located at the center, and it is extended over ~ 300 pc (González Delgado et al. 1998; Levenson et al. 2005). Wu et al. (2009) and Alonso-Herrero et al. (2012) found that the arcsecond-scale MIR SED indicates obscured AGN emission with a high SF contribution. Asmus et al. (2014) also concluded that the nuclear MIR SED is presumably still affected by significant SF emission.

NGC 7172 is an edge-on lenticular galaxy with an Sy2 nucleus (Véron-Cetty & Véron 2010). Smajić et al. (2012) found a prominent dust lane projected along the nucleus. The

arcsecond-scale MIR SED might be affected by significant SF (Wu et al. 2009; Gallimore et al. 2010). However, Asmus et al. (2014) concluded that the nuclear MIR SED is free of SF contamination.

NGC 7465 is a spiral galaxy with an Sy2 nucleus. This source is part of a group of nine interacting galaxies (Haynes 1981). The dominant stellar population in the nuclear region of NGC 7465 corresponds to stars between K3 III and M3 III types, according to the relative absorption band measurements (Ramos Almeida et al. 2009).

NGC 7582 is a highly inclined barred spiral galaxy with an obscured nucleus. The nuclear spectrum has been studied as a composition between AGN and starburst (Veron et al. 1997). The AGN is surrounded by a powerful SF disk (major-axis diameter ~ 400 pc) and a dust lane crossing over the nucleus (Morris et al. 1985; Riffel et al. 2009). Asmus et al. (2014) concluded that the starburst dominates the total MIR emission.

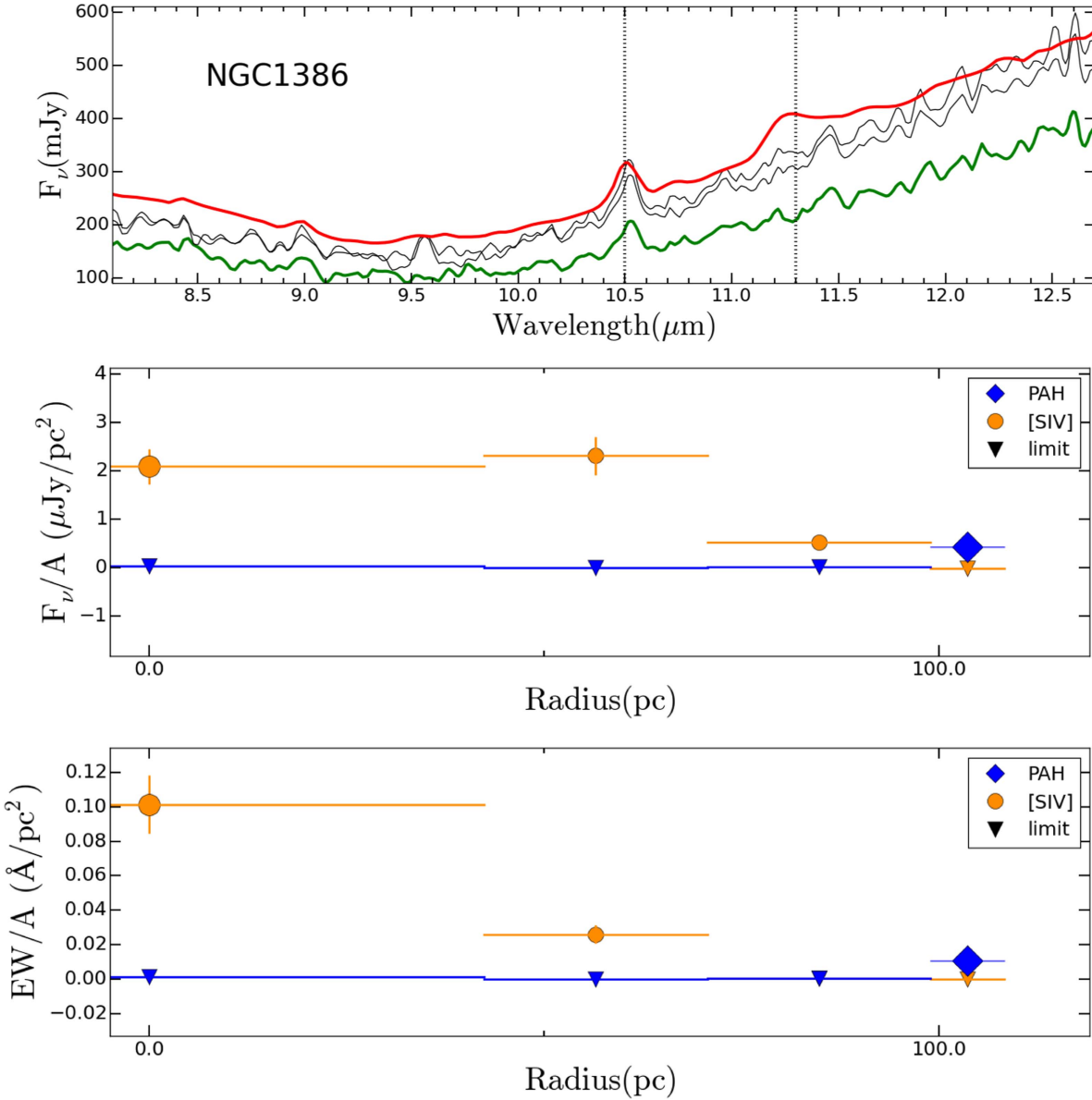


Figure 10. Extracted spectra and radial profiles for NGC 1386; same description as in Figure 7.

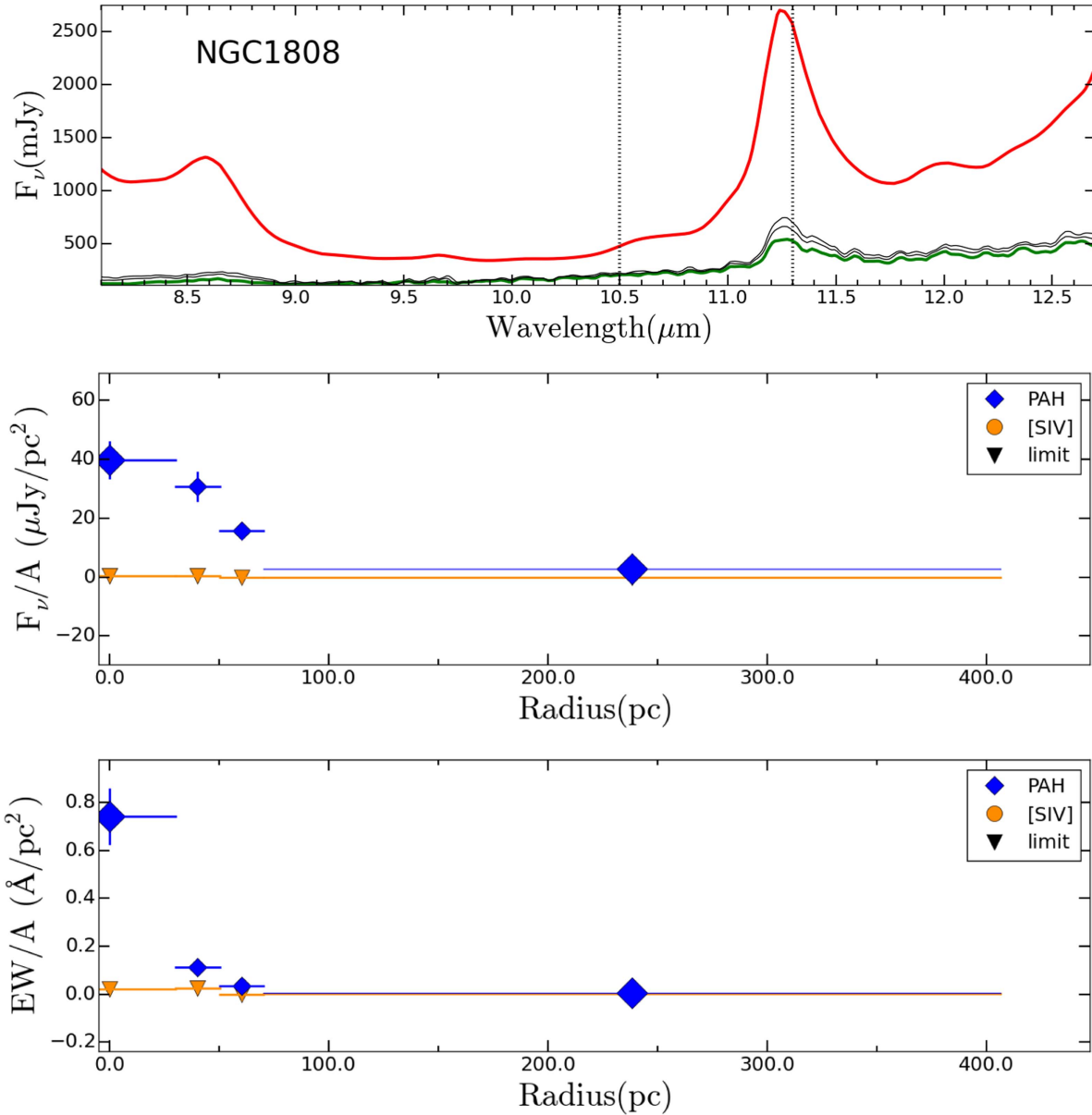


Figure 11. Extracted spectra and radial profiles for NGC 1808; same description as in Figure 7.

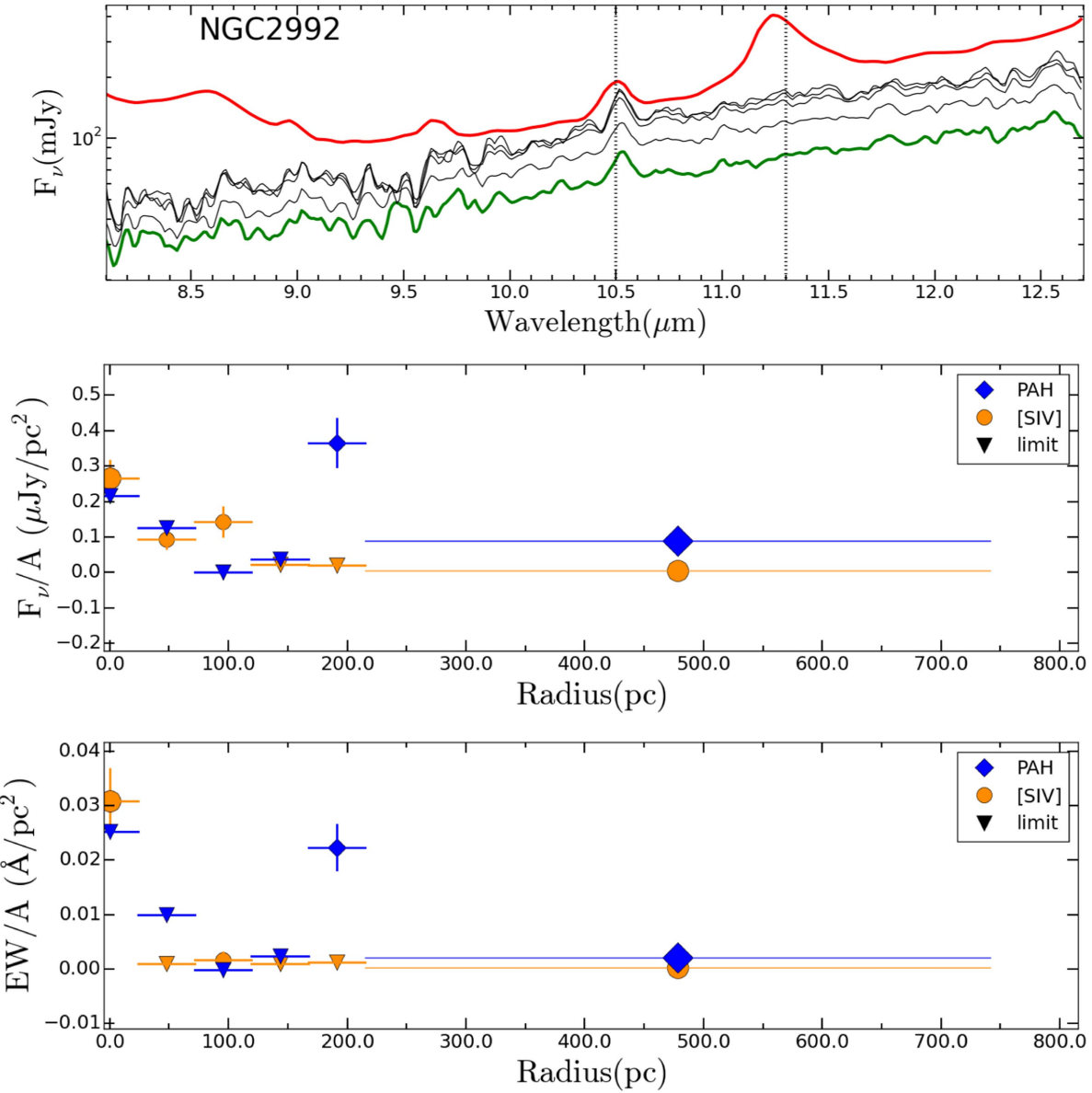


Figure 12. Extracted spectra and radial profiles for NGC 2992; same description as in Figure 7.

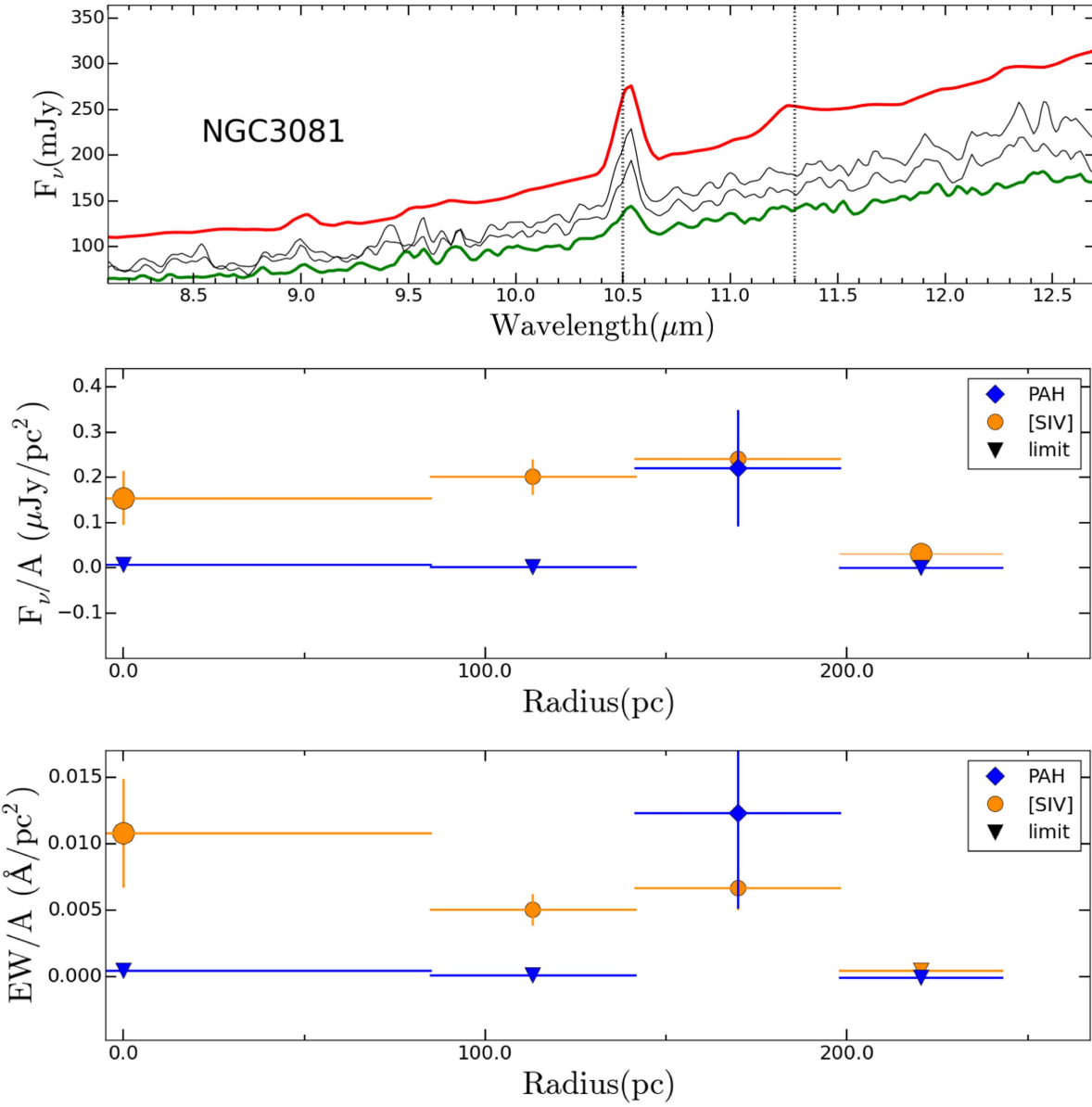


Figure 13. Extracted spectra and radial profiles for NGC 3081 with PA = 0°; same description as in Figure 7.

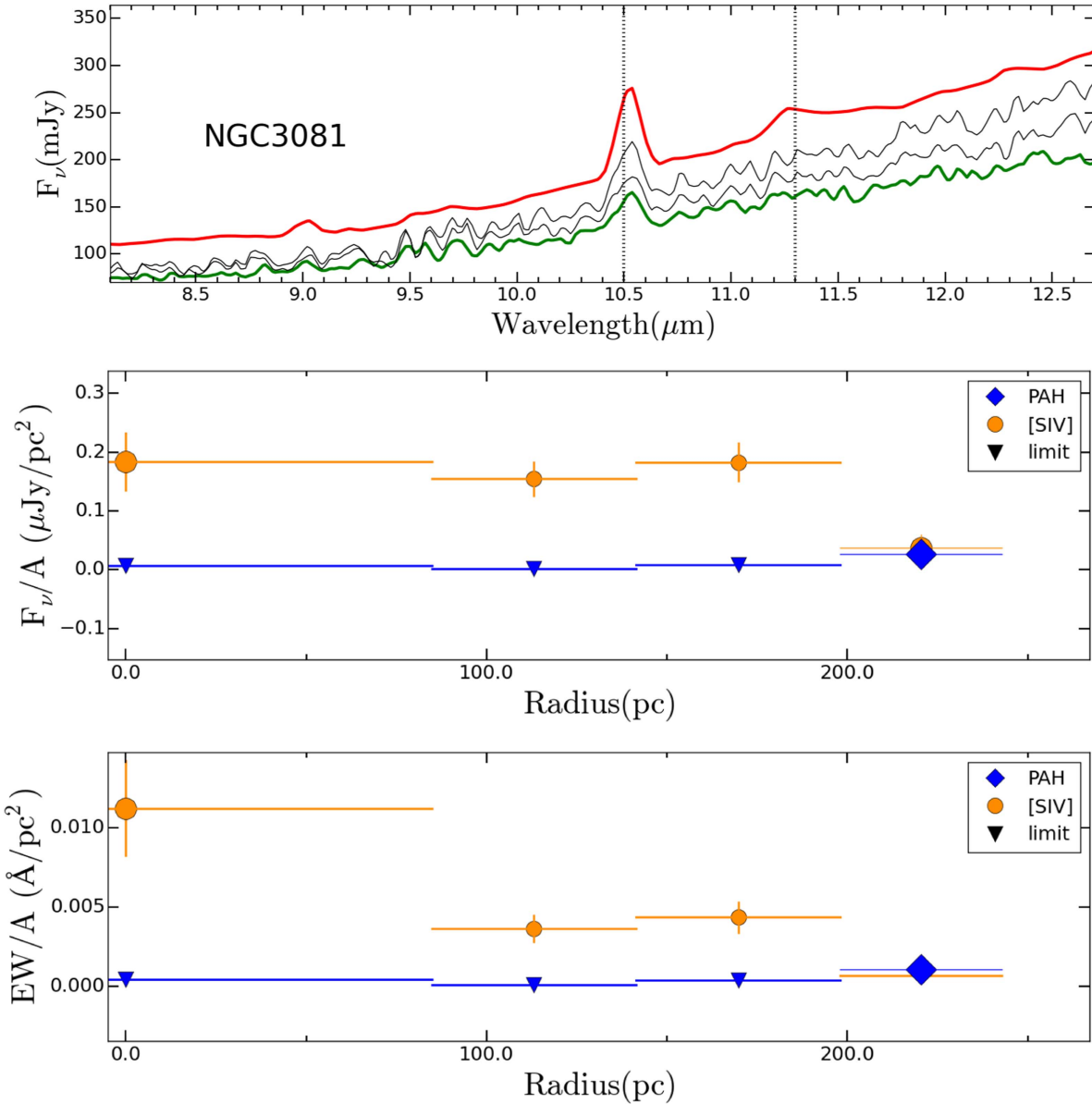


Figure 14. Extracted spectra and radial profiles for NGC 3081 with PA = 350°; same description as in Figure 7.

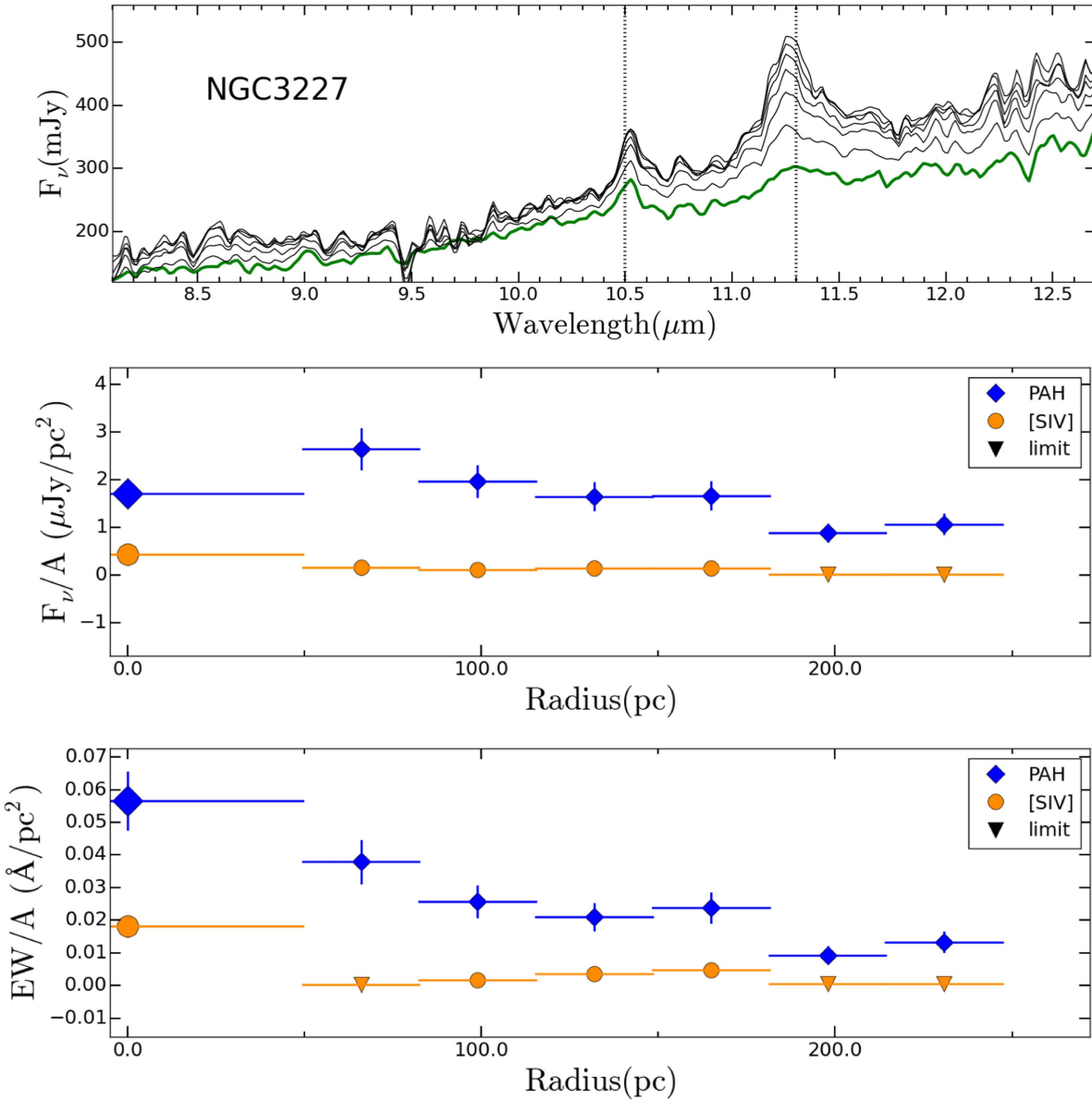


Figure 15. Extracted spectra and radial profiles for NGC 3227; same description as in Figure 7.

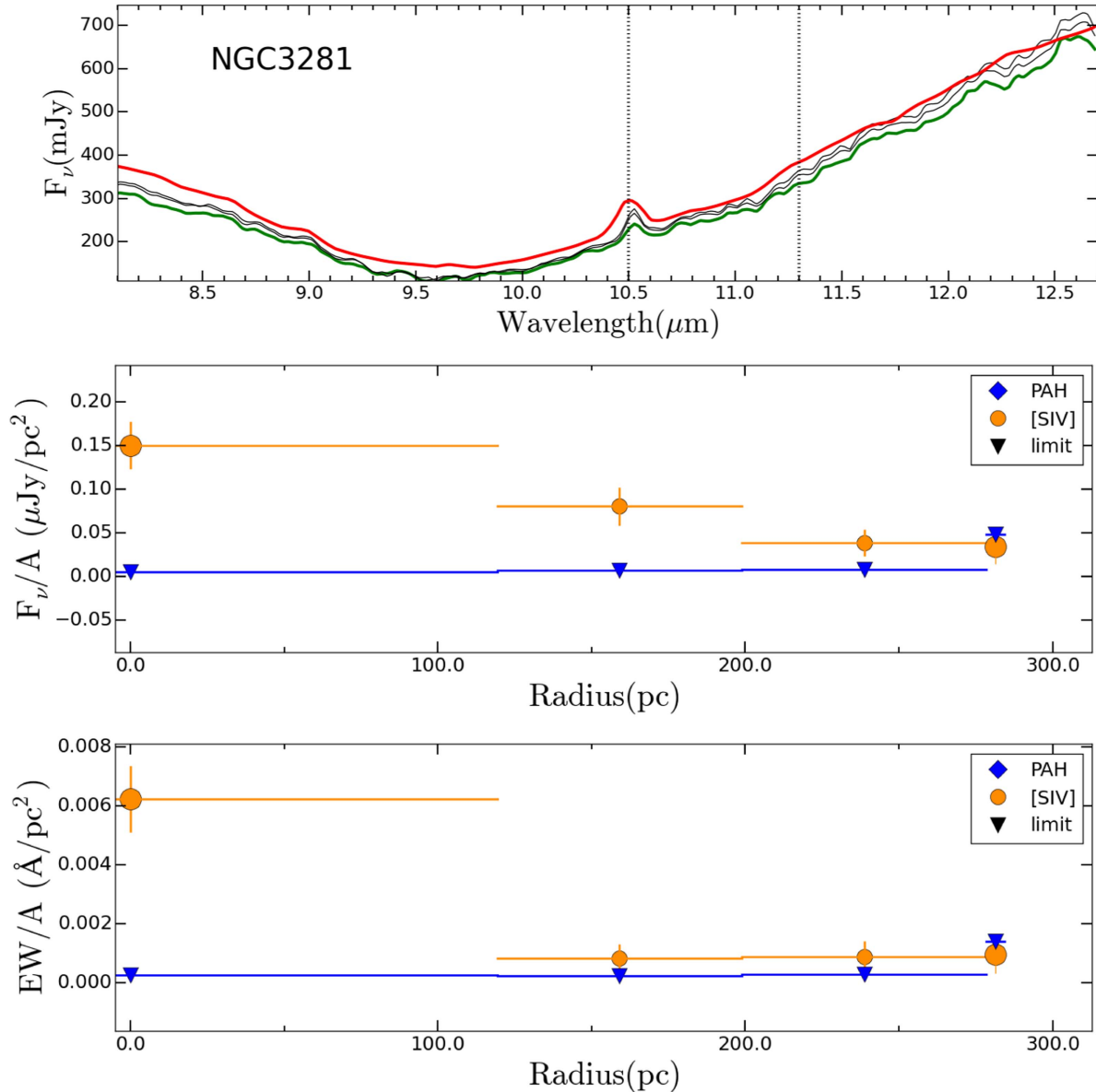


Figure 16. Extracted spectra and radial profiles for NGC 3281; same description as in Figure 7.

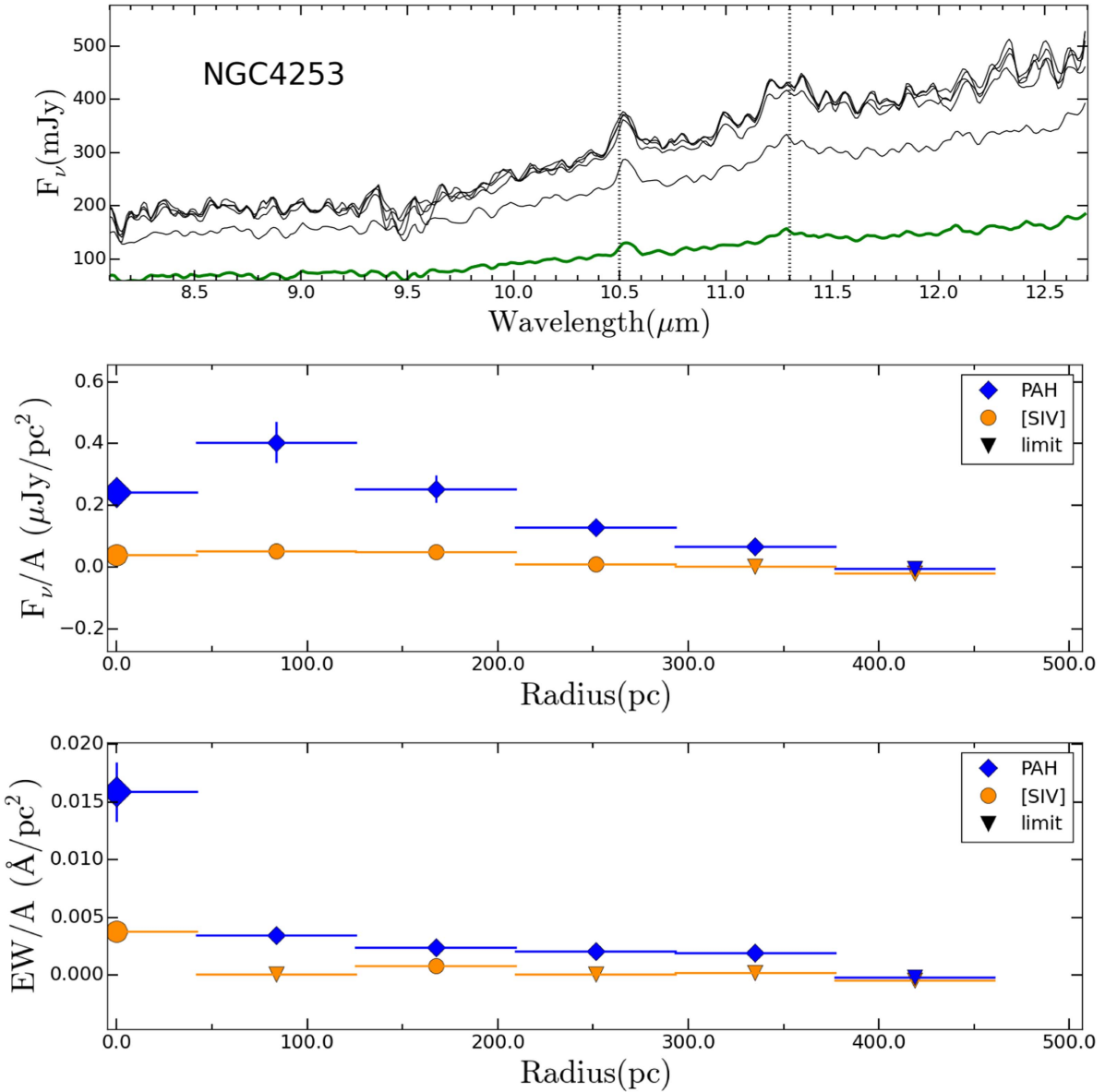


Figure 17. Extracted spectra and radial profiles for NGC 4253; same description as in Figure 7.

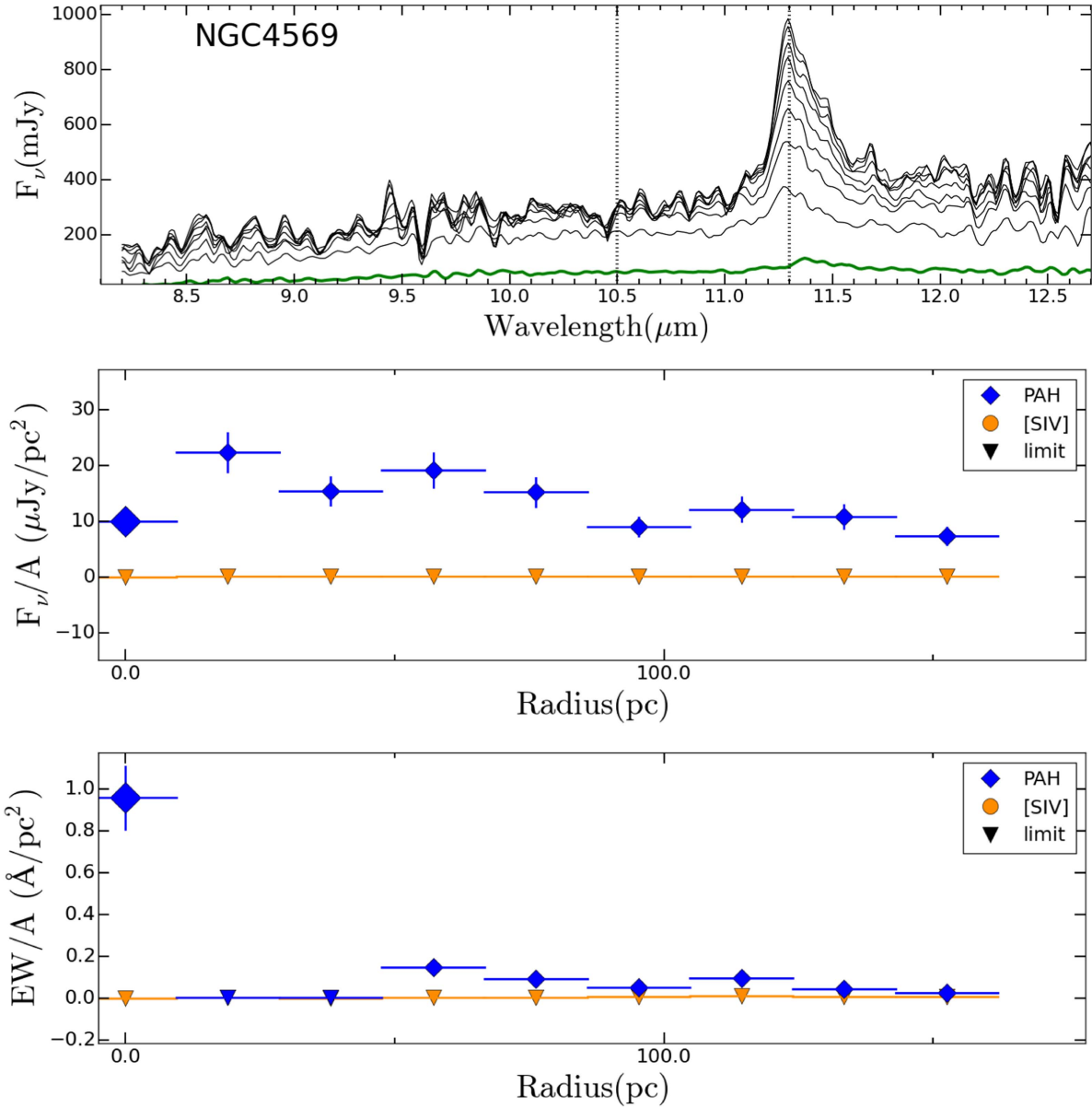


Figure 18. Extracted spectra and radial profiles for NGC 4569; same description as in Figure 7.

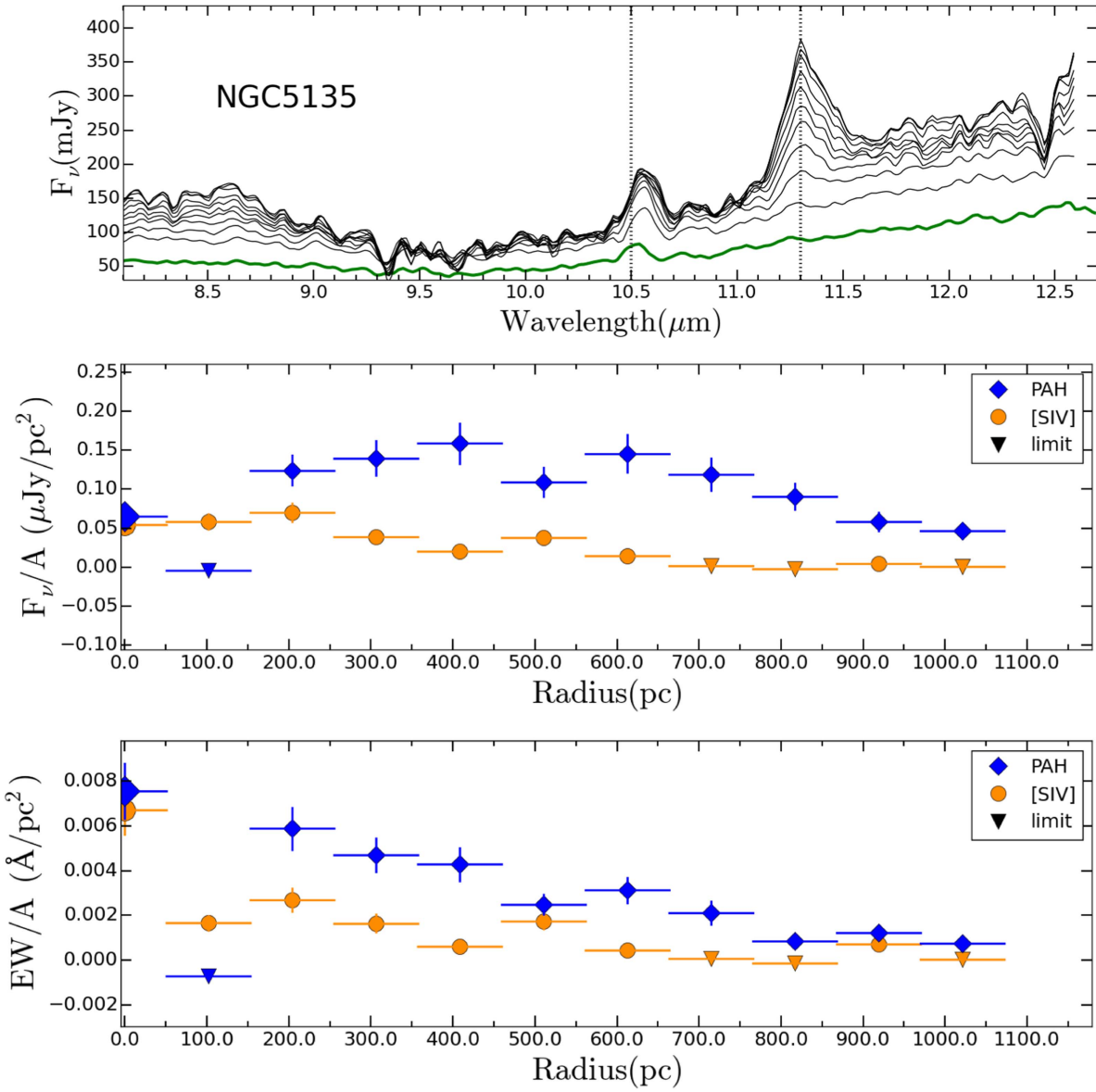


Figure 19. Extracted spectra and radial profiles for NGC 5135; same description as in Figure 7.

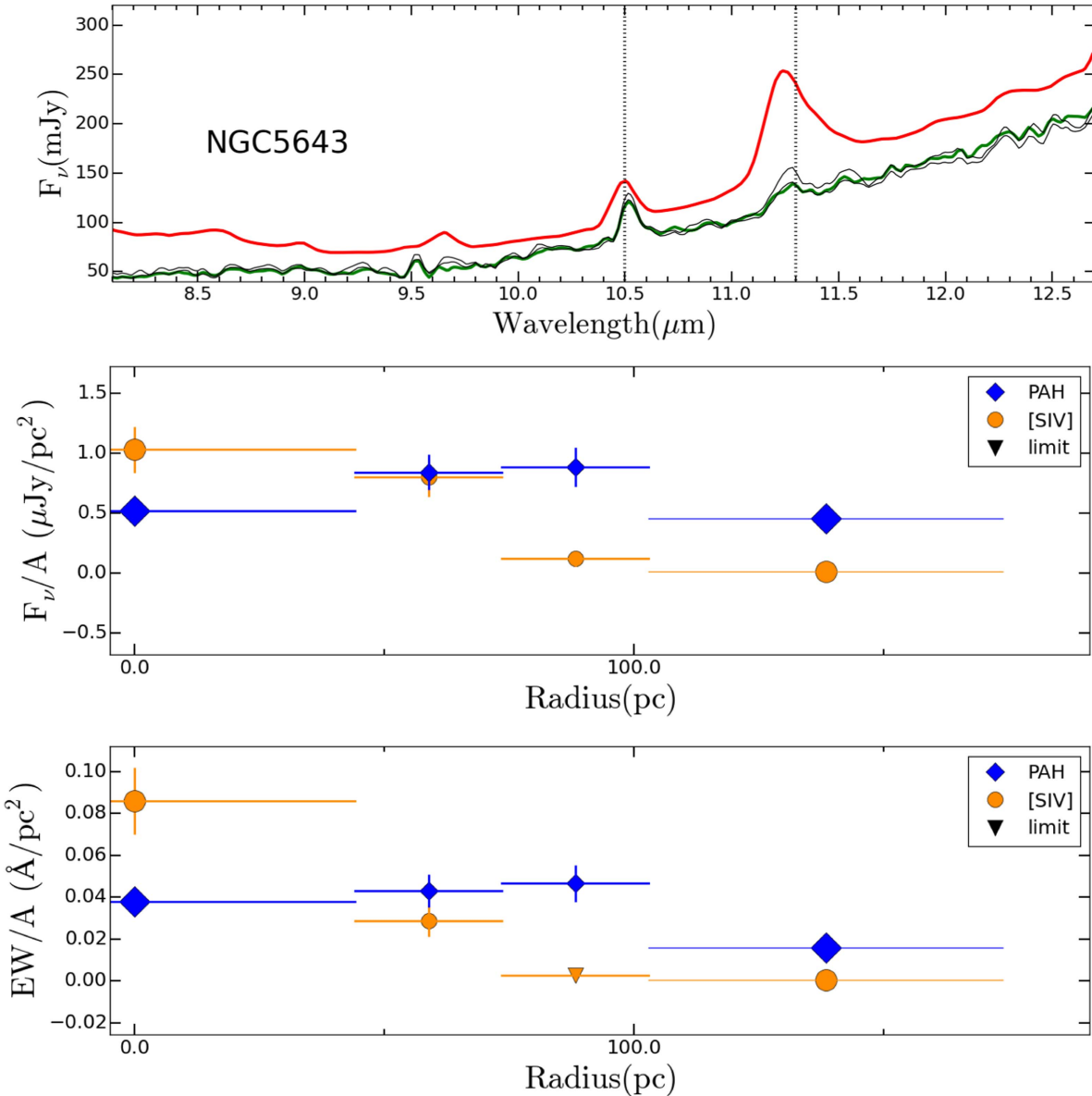


Figure 20. Extracted spectra and radial profiles for NGC 5643; same description as in Figure 7.

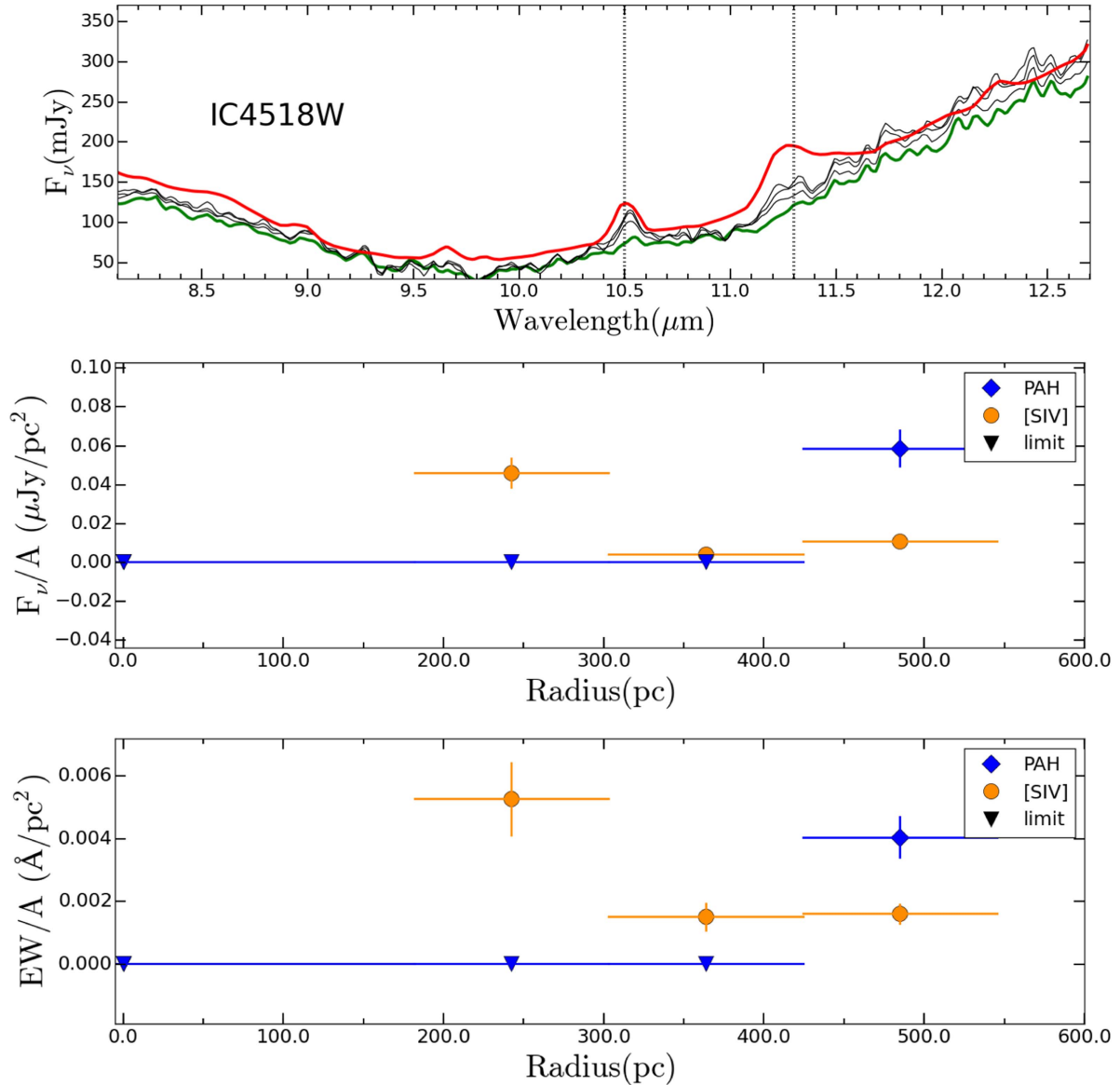


Figure 21. Extracted spectra and radial profiles for IC 4518W; same description as in Figure 7.

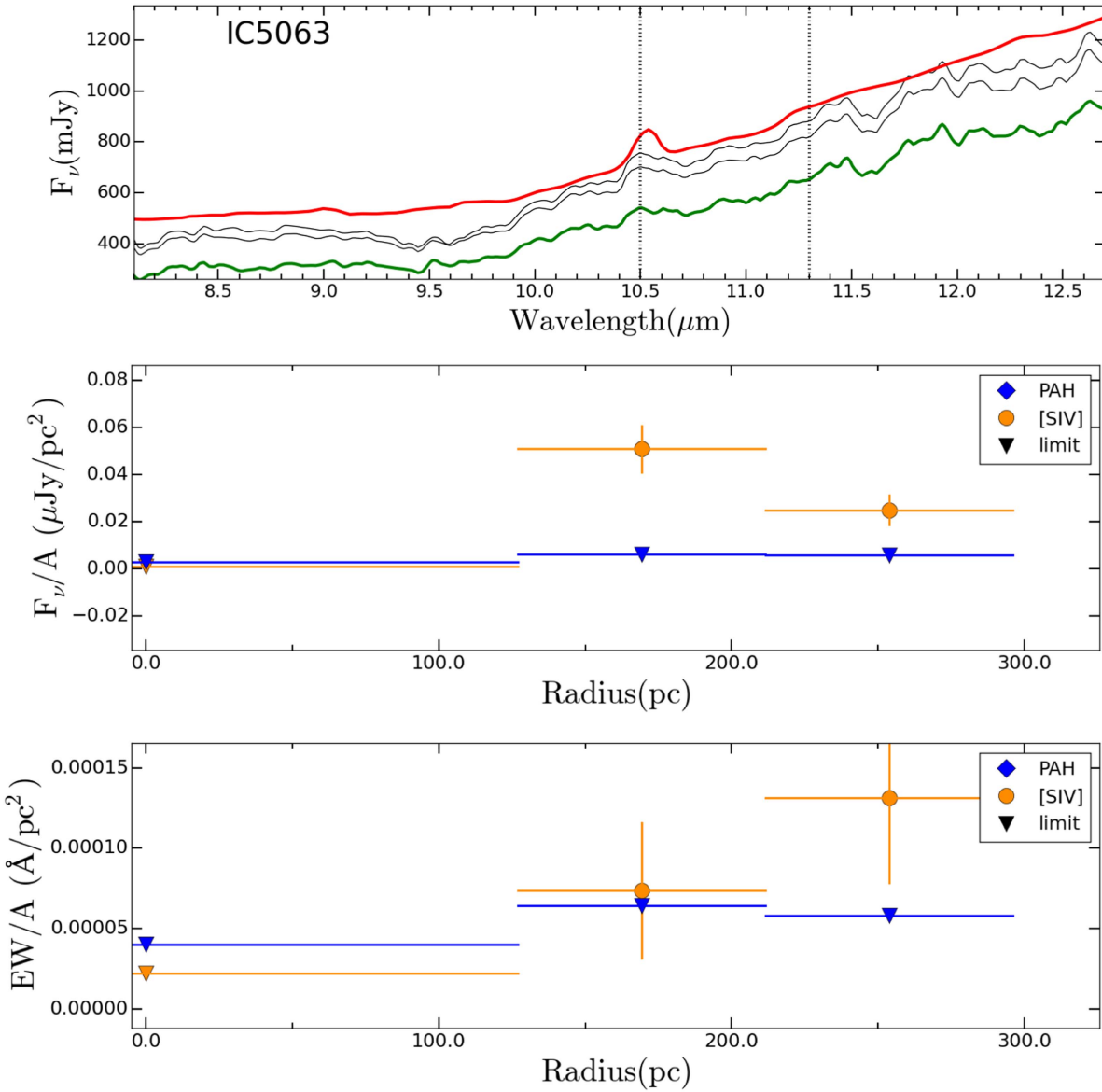


Figure 22. Extracted spectra and radial profiles for IC 5063; same description as in Figure 7.

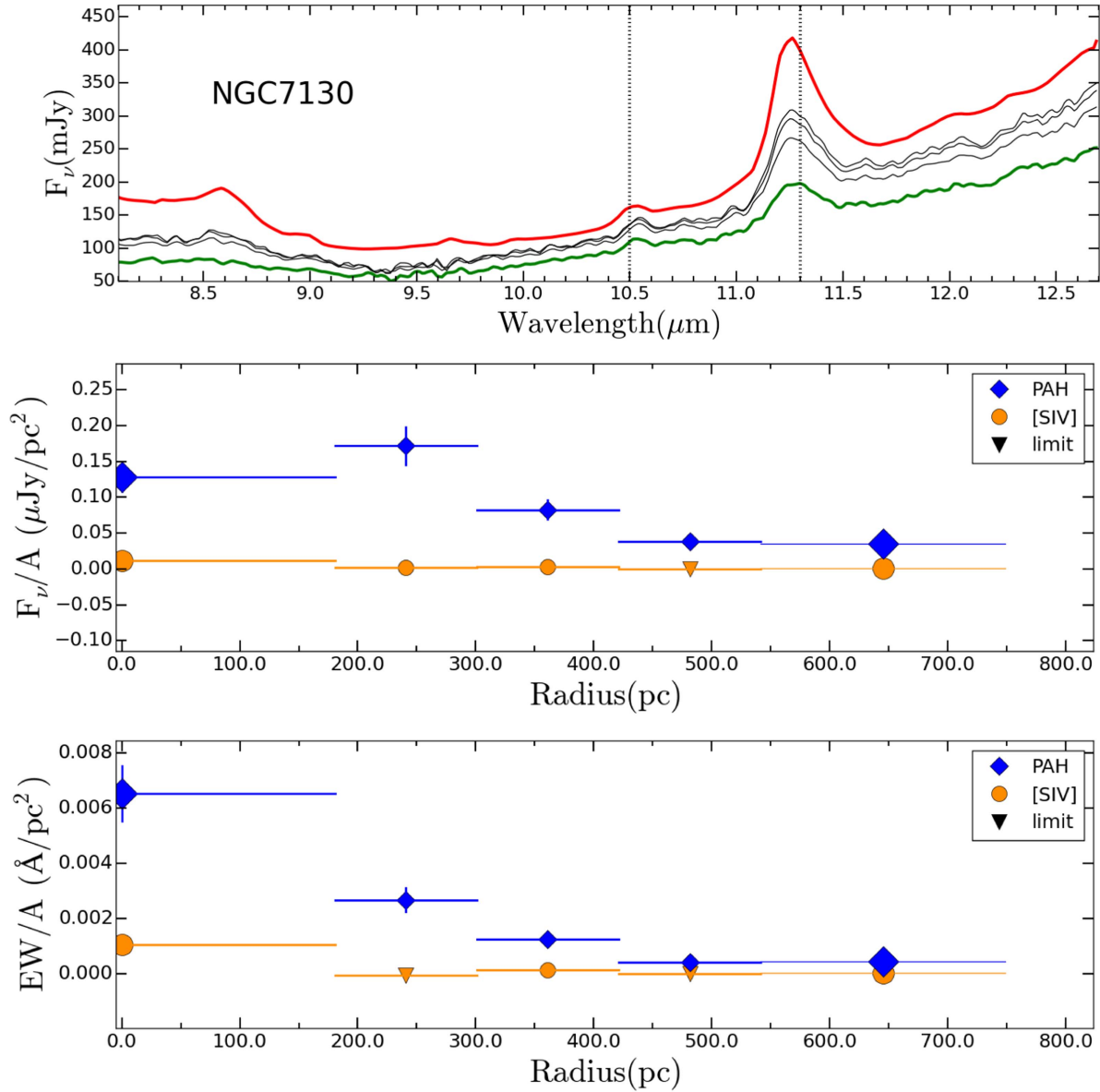


Figure 23. Extracted spectra and radial profiles for NGC 7130; same description as in Figure 7.

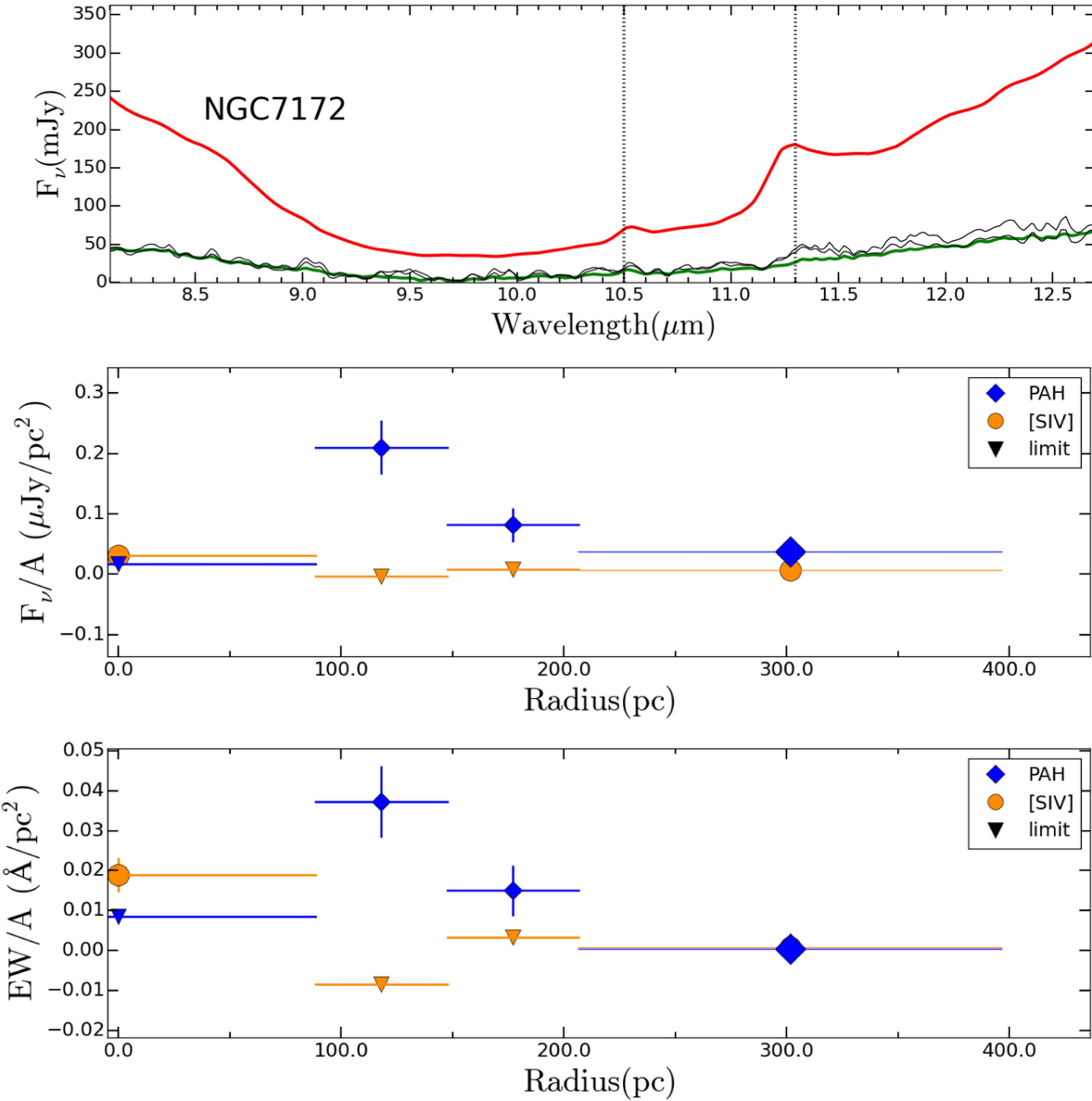


Figure 24. Extracted spectra and radial profiles for NGC 7172; same description as in Figure 7.

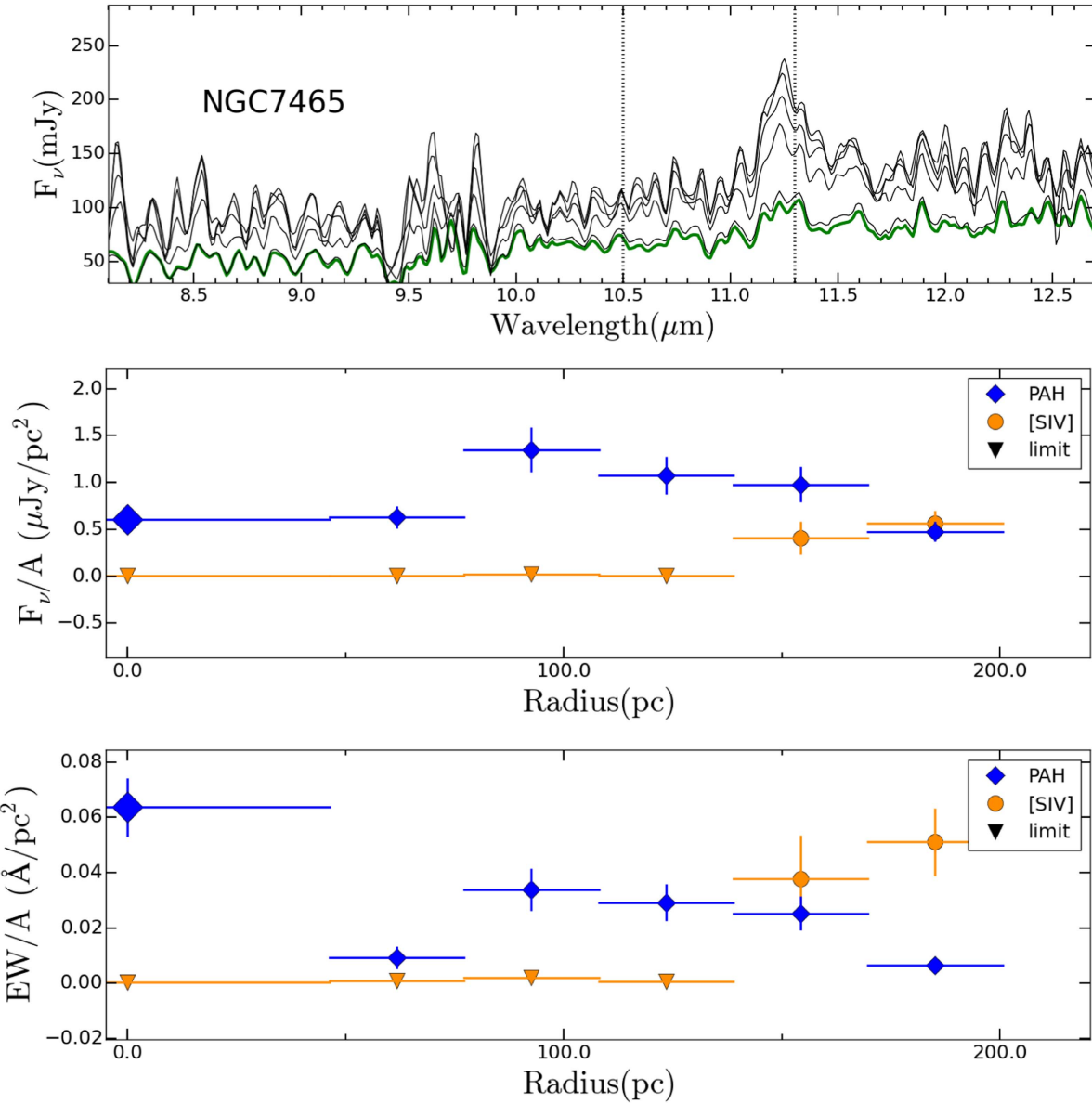


Figure 25. Extracted spectra and radial profiles for NGC 7465; same description as in Figure 7.

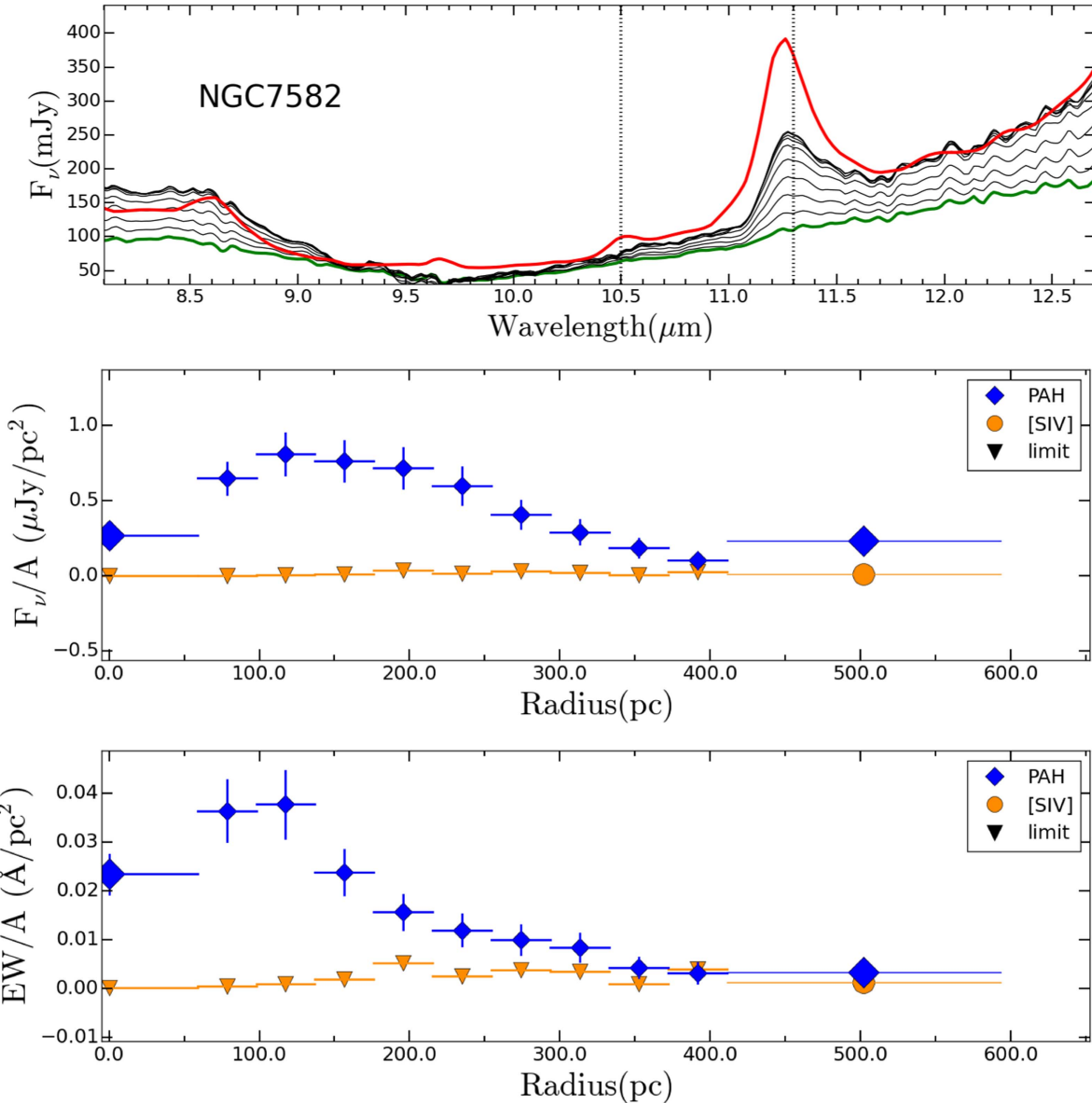


Figure 26. Extracted spectra and radial profiles for NGC 7582; same description as in Figure 7.

ORCID iDs

Donaji Esparza-Arredondo <https://orcid.org/0000-0001-8042-9867>
 Omaira González-Martín <https://orcid.org/0000-0002-2356-8358>
 Almudena Alonso-Herrero <https://orcid.org/0000-0001-6794-2519>
 Cristina Ramos Almeida <https://orcid.org/0000-0001-8353-649X>
 Tanio Díaz-Santos <https://orcid.org/0000-0003-0699-6083>
 Jose Miguel Rodríguez-Espinosa <https://orcid.org/0000-0002-0674-1470>

References

- Aitken, D. K., & Roche, P. F. 1984, *MNRAS*, 208, 751
 Alonso-Herrero, A., Esquej, P., Roche, P. F., et al. 2016, *MNRAS*, 455, 563
 Alonso-Herrero, A., Pereira-Santaella, M., Rieke, G. H., et al. 2013, *ApJ*, 765, 78
 Alonso-Herrero, A., Pereira-Santaella, M., Rieke, G. H., & Rigopoulou, D. 2012, *ApJ*, 744, 2
 Alonso-Herrero, A., Ramos Almeida, C., Esquej, P., et al. 2014, *MNRAS*, 443, 2766
 Asmus, D., Höning, S. F., Gandhi, P., Smette, A., & Duschl, W. J. 2014, *MNRAS*, 439, 1648
 Barnes, J. E., & Hernquist, L. E. 1991, *ApJL*, 370, L65
 Bedregal, A. G., Colina, L., Alonso-Herrero, A., & Arribas, S. 2009, *ApJ*, 698, 1852
 Brandl, B. R., Bernard-Salas, J., Spoon, H. W. W., et al. 2006, *ApJ*, 653, 1129
 Cicone, C., Maiolino, R., Sturm, E., et al. 2014, *A&A*, 562, A21
 Cohen, M., Allamandola, L., Tielens, A. G. G. M., et al. 1986, *ApJ*, 302, 737
 Colina, L., Sparks, W. B., & Macchetto, F. 1991, *ApJ*, 370, 102
 Dale, D. A., Smith, J. D. T., Armus, L., et al. 2006, *ApJ*, 646, 161
 Dasyra, K. M., Ho, L. C., Netzer, H., et al. 2011, *ApJ*, 740, 94
 Davies, R. I., Thomas, J., Genzel, R., et al. 2006, *ApJ*, 646, 754
 De Buizer, J., & Fisher, R. 2005, High Resolution Infrared Spectroscopy in Astronomy, 84
 De Robertis, M. M., & Osterbrock, D. E. 1986, *ApJ*, 301, 98

Appendix C: Physical parameters of the torus for the type 1.5 Seyfert NGC 3516 from the mid-infrared and X-ray simultaneous spectral fitting.

PAPER: Physical parameters of the torus for the type 1.5 Seyfert NGC 3516 from the mid-infrared and X-ray simultaneous spectral fitting.

PHYSICAL PARAMETERS OF THE TORUS FOR THE TYPE 1.5 SEYFERT NGC 3516 FROM THE MID-INFRARED AND X-RAY SIMULTANEOUS SPECTRAL FITTING

DONAJI ESPARZA ARREDONDO,¹ OMAIRA GONZÁLEZ-MARTÍN,¹ AND DEBORAH DULTZIN²

¹ Instituto de Radioastronomía y Astrofísica (IRyA-UNAM), 3-72 (Xangari), 8701, Morelia, Mexico

² Instituto de Astronomía (IA-UNAM), Mexico city, Mexico

(Received; Revised ; Accepted)

Submitted to ApJ

ABSTRACT

To understand the diversity of classes observed in active galactic nuclei (AGN) a geometrically and optically thick torus of gas and dust is required to obscure its inner parts from some lines of sight. However, this torus is not spatially resolved even for the closest AGN. Spectroscopic studies have been broadly used to characterize the main properties of the torus. However, the torus has a large number of parameters that have not been constrained yet. Here, we study if the combination of X-ray and mid-infrared spectra can better constraint the physical parameters of the torus because both show important signatures of obscuration. We used the nearby type-1.5 NGC 3516 as a test object. This object is ideal for the wealth of archival data, the closeness, and the relatively high AGN luminosity that seems to dominate both X-ray and mid-infrared frequencies. In particular, we included the high spectral resolution IRS/*Spitzer* spectra for mid-infrared observations and NuSTAR observations for X-rays. We used the Clumpy models described by Nenkova et al. (2008a,b) for mid-infrared spectra and the radiative transfer code Borus described by Baloković et al. (2018) for X-ray spectra. Borus model can be fitted within the X-ray spectral fitting software XSPEC. We develop a code able to convert Clumpy models and IRS/*Spitzer* spectra into XSPEC format to simultaneously fit mid-infrared and X-ray data. Mid-infrared data are able to constrain N_0 , σ , Y , θ_i , and τ parameters. Parameter q is degenerated. X-ray spectral alone are able to constrain Γ , $\log N H_{tor}$, θ_{tor} parameters. Parameter θ_i and n_H are degenerated. The simultaneous fit is able to better constrain Γ , τ ($\log N H$), θ_i , and $\sigma(\theta_{tor})$, and q parameters, as demonstrated by the test perform on the degeneration of the parameters. Thus, this technique can be used to infer the physical properties of the torus. NGC 3516 shows a torus with $\Gamma \sim 1.5$, $\tau \sim 42.3$, $\theta_i < 10^\circ$, and $\sigma \sim 35^\circ$, and $q \sim 0.03$.

Keywords: active — nuclei — mid-infrared — X-rays

1. INTRODUCTION

According to the simple unification model of active galactic nuclei (AGN), a toroidal structure (broadly referred as a torus) provides the anisotropic obscuration needed to explain the diversity of AGN observed across the electromagnetic spectrum (Antonucci 1993; Urry & Padovani 1995). More recent works suggest that this torus actually changes for different luminosities and accretion rates (Shlosman 2005; Elitzur & Netzer 2016). Thus, line of sight of the observer compared to the torus, its geometry, chemical composition, and distribution are key to understand AGN diversity, perhaps linked to fundamental changes for different AGN classes.

This torus absorbs optical/UV accretion disc radiation and re-emit at infrared wavelengths (see Netzer 2015, for a review). Radiative transfer models based on toroidal geometry have proven successful in reproducing the infrared spectral energy distribution (SED) of AGNs (e.g. Fritz et al. 2006; Ramos Almeida et al. 2009; Alonso-Herrero et al. 2011; Höning & Kishimoto 2017). Initially, most authors used smooth dust distributions with different radial and vertical density profiles (e.g. Pier & Krolik 1993; Granato & Danese 1994; Efstathiou & Rowan-Robinson 1995; Schartmann et al. 2005; Fritz et al. 2006). It was, however, proposed early that the dust is most probably arranged in clouds instead of being smoothly distributed (e.g. Krolik & Begelman 1988; Tacconi et al. 1994). The dust torus has been the subject of several kinds of models that aimed to extract physical properties from SED and, in some cases, interferometric observations. We can divide them into four kinds: smooth (Fritz et al. 2006; Feltre et al. 2012), clumpy (Nenkova et al. 2008a,b; Höning et al. 2010; Höning & Kishimoto 2010), smooth + clumpy (Stalevski et al. 2012; Siebenmorgen et al. 2015), and windy (Höning & Kishimoto 2017). Thus, modeling AGN infrared spectra provide evidence of the dust geometry, composition and distribution.

Furthermore, signatures of reprocessing emission by the torus in the X-ray band arise primarily from interaction of X-ray photons with the surrounding gas (Ghisellini et al. 1994; Krolik et al. 1994). The main two features are the neutral iron lines around 6.4 keV and the Compton hump peaking at \sim 10-30 keV. These features have been observed in all X-ray spectra of AGNs. Reprocessed continua are known to vary as a function of geometry of the reprocessing material (Nandra & George 1994). It has been suggested that the narrow cores of the FeK α emission lines in AGNs are likely produced in the torus. Indeed, recently significant FeK α line variability of several tens of percent was detected with timescales larger by a factor of 10-100 than the inner radius of the torus, consistent with the view that X-ray reflection by a torus is a main origin for a narrow FeK α line (Fukazawa et al. 2016). Furthermore, the FeK α line has been claimed to show anisotropic emission, consistent with the origin on the torus (Liu & Wang 2010). Narrow neutral iron lines (FeK α) are confirmed to be an ubiquitous component in Seyfert spectra (Bianchi et al. 2004). Under the scenario in which this narrow line is produced in the inner parts of the torus, it is a positive test for the unification Model, suggesting the presence of the torus in (almost) all sources, even if unobsured. Therefore, X-ray spectral fitting to the high energy continuum emission (above 10 keV) and the FeK α line might provide important information about the torus geometry, cloud distribution and opacity.

The 100-fold increase in sensitivity in the hard X-ray band (>10 keV) brought by *NuSTAR* (Harrison et al. 2013) made possible to study the spectral signatures of the torus for the first time. Empirically motivated spectral models with approximately toroidal geometry have been calculated by Murphy & Yaqoob (2009) (motors), Ikeda et al. (2009), Brightman & Nandra (2011) (BNtorus), Liu & Li (2015) (ctorus) and Furui et al. (2016) (MONACO). Several of them were made available to the community. Recently, Baloković et al. (2018) present a new grid of X-ray spectral templates based on radiative transfer calculations in neutral gas in an approximately toroidal geometry. The main advantage of this model is that the main parameters are closely linked to the Clumpy torus models.

We present in this paper a new technique to combine X-ray and mid-infrared spectral information to make a simultaneous fit to torus models. We demonstrate that this paper is successful to constrain the torus parameters, that are not accesible using only X-ray or mid-infrared spectra. The paper is organized as follows.

2. DATA

2.1. *X-ray data*

There are several X-ray observations available in the archives with different satellites for NGC 3516. However, since we would like to constrain the reflection component associated with the torus we need to cover energies above 10 keV. Moreover, low energies are fully dominated by the absorbers in NGC 3516. Since it is out of the scope of this paper to study these absorbers we will be focused our analysis at energies above 2-3 keV.

There are eight *Suzaku* and two *NuSTAR* observations able to cover the \sim 2-50 keV band. *NuSTAR* has the advantage that observe with a single mode from 2-79 keV, which make this satellite perfect to study the reflection component of

AGN. *Suzaku* has two instruments (XIS and HXD) that need to be scaled to correct from cross-calibration issues. The advantage of *Suzaku* data is that it covers energies below 2 keV. However, as explained before, this range is not useful for our study.

Therefore, we use the hard band 2-50 keV spectrum observed with *NuSTAR* (Harrison et al. 2013). *NuSTAR* has observed NGC 3516 two times (ObsIDs 60002042002 and 60002042004, P.I. Harrison) observed in 2014 (24th of June and 11th of July, respectively). *NuSTAR* launched in June 2012, is the first focusing hard X-ray telescope¹. It has a field of view 13 x 13 arcsec. It consists of two co-aligned X-ray detector pairs with corresponding focal plane modules FPMA and FPMB. The availability of two *NuSTAR* observations will allow us to use absorption variations to constrain the torus properties, as suggested by Baloković et al. (2018).

Reduction of the *NuSTAR* data was done using the data analysis software *NuSTARDAS* v.1.4.4 distributed by the High Energy Astrophysics Archive Research Center (HEASARC). The calibrated, cleaned and screened event files were generated using the NUPipeline task (CALDB 20160502). A circular region of 2 arcmin radius was taken to extract the source and background spectrum on the same detector and to compute the response files (RMF and ARF files) using the NUPRODUCTS package available in *NuSTARDAS*. Finally, we used the GRPPHA task within the FTOOLS to group the spectra with at least 60 counts per bin. The net exposures are 51 and 72 ksec for ObsIDs 60002042002 and 60002042004, respectively. We have found some cross-calibration issues between the FPMA and FPMB modules, larger below ~ 3 keV. Thus, we *NuSTAR* data above 3 keV.

2.2. Mid-infrared data

We have used the high-resolution *Spitzer*/IRS spectrum downloaded from the CASSIS² catalog (the Cornell Atlas of *Spitzer*/IRS Sources, Lebouteiller et al. 2011). The resolution of *Spitzer*/IRS ($R \sim 60 - 130$) is similar to that obtained by ground based observations. Note that the mid-infrared spectrum do not show any signs of strong nuclear starburst. Indeed, according to Gonzalez-Martin et al. (2015) it includes more than 90% of torus component, with 10% stellar component that affects to the $5-8\mu\text{m}$ and a few relatively weak emission lines along the mid-infrared spectrum. Note that this stellar component will be properly accounted for using a stellar library (see Section 3.2). This lack of strong stellar or Starburst components makes the *Spitzer*/IRS spectrum of NGC 3516 ideal to study the torus parametrization throughout spectral fitting.

Note that, in order to perform spectral fitting to the data, we converted the mid-infrared *Spitzer*/IRS spectrum into XSPEC format using FLX2XSP task within HEASOFT. This tool reads a text file containing one or more spectra and errors and writes out a standard XSPEC pulse height amplitude (PHA³) file and response file. This will allow us to perform X-ray and mid-infrared simultaneous fit too.

3. SPECTRAL FITTING

Spectral fitting is performed using XSPEC fitting package. XSPEC is a command-driven, interactive, spectral-fitting program within the HEASOFT⁴ software. XSPEC has been used to analyze X-ray data like *ROSAT*, *ASCA*, *Chandra*, *XMM-Newton*, *Suzaku*, *NuSTAR*, or *Hitomi*. XSPEC allows users to fit data with models constructed from individual components. XSPEC already includes a large number of incorporated models but new models can be uploaded using the ATABLE task. To assess for the goodness-of-fit XSPEC performs a test to reject the null hypothesis that the observed data are drawn from the model (by including χ^2/dof and null hypothesis probability). The parameter confidence regions are found by surfaces of constant delta statistic from the best-fit value (ERROR task). XSPEC also finds simultaneous confidence regions of multiple parameters to study the degeneracy among parameters. Thus, XSPEC provides a wide range of tools to perform spectral fitting to data, being able to parallel processes in order to speed up them.

X-ray data and models used in this analysis are already formatted to be used within XSPEC. To use these capabilities for the mid-infrared (and simultaneous X-ray and mid-infrared fitting), we convert model and data to XSPEC format (see also previous section).

3.1. X-ray model

¹ <https://heasarc.gsfc.nasa.gov/docs/nustar/>

² <http://cassis.astro.cornell.edu/atlas/>

³ Engineering unit describing the integrated charge per pixel from an event recorded in a detector.

⁴ <https://heasarc.gsfc.nasa.gov>

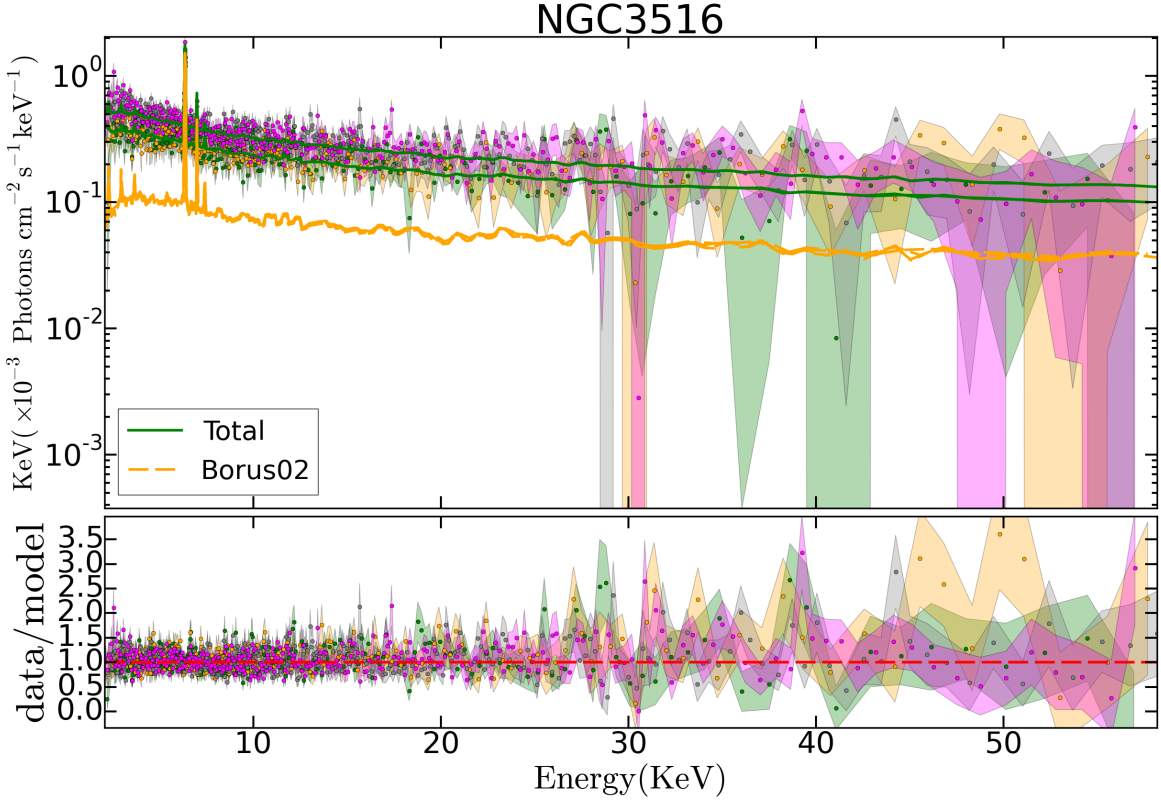


Figure 1. NGC 3516 fit spectra using Borus model. The green lines show the total fit, while the yellow lines show our model (using Borus02).

The majority of the AGN emission is produced in the accretion disk and emitted in the optical and ultraviolet (UV) wavelengths. A portion of this emission is reprocessed by a corona of a plasma of hot electrons close to the accretion disk that scatters the energy in the X-ray bands due to inverse Compton (Netzer 2015; Ramos Almeida & Ricci 2017, and references therein). This Comptonization produces one of three main components of X-ray spectra which is known as the intrinsic continuum and is modelled through a power-law with a photon index (Γ) typically around 1.8-2.3. This feature dominates the spectral emission above 2 keV and it is a distinctive signature of AGN emission. The power-law emission is a function of the plasma temperature (kT_e), optical depth (τ) and the cutoff energy (Haardt & Maraschi 1991; Marinucci et al. 2015). One part of this primary emission is absorbed by the torus or the broad line region. Another portion is reprocessed to give place to other two other components that depend on the material (Ricci et al. 2011): The Compton hump component that peaks at 30 KeV and is associated with reprocessing due to Compton-thick material ($N_H > 10^{24} \text{ cm}^{-2}$ Zdziarski et al. 1995; Magdziarz & Zdziarski 1995). The most obvious reprocessing material es the dusty structure and the shape of the reflection component depends on the geometry and chemical composition of this reflector (Ghisellini et al. 1994). Therefore, this component depends only on the geometrical covering factor (C_{factor}) of the torus and its average column density. The iron k_α (Fe k_α) emission line at 6.4keV is due to the reflection of X-ray photons in Compton thin material. The origin of the narrow Fe K_α line is also associated to the torus, while the broad Fe k_α line is thought to be originated in the inner parts of the accretion disk (Fabian 1998; Laor 1991). The most accepted case is found in MCG-6-30-15, where a red wing of the Fe k_α line is attributed to reflection in the accretion disk at only a few Schwarzschild radii from the black hole (Vaughan & Fabian 2004). This analysis is based on the idea that the re-processor is the torus, which seems to be the case for the bast majority of the sources (Matt et al. 1991)

Different models for this reprocessed emission have been developed recently, with the aim of reproducing the X-ray spectrum using a torus-like morphology. The most popular models are MYtorus (Murphy & Yaqoob 2009), etorus (Ikeda et al. 2009), BNtorus (Brightman & Nandra 2011), and cotorus (Liu & Li 2015). These models use a Monte

Carlo method to derive approximations to green functions for a toroidal reprocessor. The main difference between them is the geometry of the torus considered and the treatment of the different components. Brightman & Nandra (2011) shows a comparison between these models. Our work follows a recent work done by Baloković et al. (2018). They use a grid of X-ray spectral templates (borus02) based on a radiative transfer code BORUS (M. Baloković et al. 2018 in preparation). The geometry of borus02 is a uniform-density sphere with polar cutouts (currently more accepted), which is similar to etorus and cotorus. The free parameters of borus02 are: spectral index of the incident radiation Γ , the high energy cutoff E_{cut} of the incident radiation, the average column density $\log(NH_{tor})$, angular size of the torus $thTor$, inclination angle of the torus compared to the observer $thInc$. Unlike other models, borus02 has the high energy cutoff (E_{cut}) and the relative abundance of iron (A_{Fe}) as free parameters. The variation range of Γ parameter is larger compared with cotorus and etorus and the angular size of the torus has a larger range than etorus. However, the main advantage of this model for our analysis is that it allows us to constrain several parameters closely linked to the mid-infrared models. $thTor$ and $thInc$ are directly linked to mid-infrared models. Furthermore, $\log(NH_{tor})$ can be associated to the opacity of the clouds τ_ν used within mid-infrared Clumpy models.

Following Baloković et al. (2018), the model used in this work to fit NGC 3516 is the command sequence in XSPEC:

$$m = phabs * (atableborus02_v170323c.fits + zphabs * cabs * cutoffpl) \quad (1)$$

The component *phabs* is the galactic absorption foreground. In case of NGC 3516 is 0.0305 cm^{-2} . The *zphabs*cabs* represents the line-of-sight absorption at the redshift of the X-ray source. We linked the hydrogen column density N_H component to the *zphabs* to take into account the total extinction along the line-of-sight Baloković et al. (2018) added an extra component in their model that is related to the scattered emission of the intrinsic continuum. This component only affects at energies below 2 keV. Thus, we discarded this component because our data only cover the range between 2-50 keV. The *atableborus02_v170323c.fits*⁵ component is the table that contains 8 parameters arising from reprocessing in the torus.

Table 1. Borus02 model parameters

Parameter	Table C
Γ	$1.46 \pm^{0.03}_{0.02}$
$\log(NH_{tor})$	$22.3 \pm^{0.3}_{0.2}$
$thTor$	$72.4 \pm^{9.3}_{5.6}$
$thInc$	87.1^*
nH (zphabs)	$0.5 (\times 10^{22})^*$
$norm_{obs1}$ (borus02)	$4.1 \pm^{6}_{3} (\times 10^{-2})$
$norm_{obs1}$ (cutoffpl)	$4.8 \pm^{0.4}_{0.3} (\times 10^{-4})$
$norm_{obs2}$ (borus02)	$3.9 \pm^{2}_{1} (\times 10^{-2})$
$norm_{obs2}$ (cutoffpl)	$7.6 \pm^{0.9}_{0.5} (\times 10^{-4})$

3.2. Mid-infrared model

The dust torus has been the subject of several kinds of models at mid-infrared wavelengths that aimed to extract physical properties from SED and, in some cases, interferometric observations. We can divide them into four kinds: smooth (Fritz et al. 2006; Feltre et al. 2012), clumpy (Nenkova et al. 2008a,b; Hönig et al. 2010; Hönig & Kishimoto 2010), smooth + clumpy (Stalevski et al. 2012; Siebenmorgen et al. 2015), and windy (Hönig & Kishimoto 2017). Among them the most extensively used one is the Clumpy model by Nenkova et al. (2008b) due to their large number of SEDs and probed ability to explain the mid-infrared emission of low luminous (González-Martín et al. 2017), intermediate luminous (Ramos Almeida et al. 2009), and high luminous (Martínez-Paredes et al. 2017) AGNs. It is a

⁵ This table is available in the web: <http://www.astro.caltech.edu/mislavb/download/index.html>

radiative transfer code that models the AGN clumpy dust torus emission⁶ (Nenkova et al. 2008a,b), developed based on those proposed by Nenkova et al. (2002); Elitzur et al. (2004); Elitzur (2006). They developed a formalism that takes proper account of the concentration of dust in clumps or clouds, referred to as clumpy, nature of the AGN torus. The models part of the idea of a clumpy dust torus (i.e. not homogeneous) whose parameters are the inclination angle (i), the number of clouds in the equatorial plane of the torus (N_0), the width of the angular distribution (σ), the relation between inner and outer radius ($Y = R_{\text{out}}/R_{\text{in}}$), index for a power law (q), and the optical depth of each cloud (τ). This models include 1,247,400 SEDs in the 0.001-1,000 μm wavelength range. These models are capable of explaining some observed features in the IR spectra of AGNs as the observed behavior of the 10 μm silicate feature in any type.

We converted the Clumpy models SED libraries to multi-parametric models within the spectral fitting tool XSPEC as an additive table. The basic concept of a table model in XSPEC format is that the file contains an N -dimensional grid of model spectra with each point on the grid having been calculated for particular values of the N parameters in the model. XSPEC will interpolate on the grid to get the spectrum for the parameter values required at that point in the fit. Firstly, we created a one parameters table (in fits format) associated to all the SEDs using the FLX2TAB task within HEASOFT. Note that each of the SEDs have been interpolated using 5,000 steps between the minimum and maximum wavelengths due to the need of equally spaces SEDs. We then, wrote a python routine to change the headers associating each SED to a set of parameters. This model has a number of free parameters, including those described at the beginning of this section plus redshift and normalization. Note that we were not able to obtain a XSPEC model using the entire SED library due to unpractical size of the final model (over 100 GB). Instead, we slightly restricted the number of clouds and the angular width to the torus to the ranges $N_0 = [1, 3, 5, 7, 9, 11, 13, 15]$ and $\sigma = [15, 25, 35, 45, 55, 65, 70]$, respectively, to recover a more transferable model (~ 6 GB). Note that this do not affect our results since XSPEC interpolate between models to find the best solution when comparing with the data.

The mid-infrared can be partially contaminated by stellar emission from the host. This is, indeed the case of NGC 3516 where 10% contribution of stellar component has been found by performing spectral decomposition to the data. In order to be able to include this component, we include...

4. FITTING RESULTS FOR THE MID-INFRARED SPECTRUM

We used two main components to fit the the mid-infrared *Spitzer*/IRS spectrum of NGC 3516; the clumpy model and the stellar component. We added this stellar component to accounts for a small contribution to the mid-infrared emission (5% in the 5-30 μm range, mainly to the continuum at short wavelength (below 30 μm). To improve our fit we added 16 narrow emission lines which are registered in previous works and show in the interactive spectrum in CASSIS. We used the *addline* tool available in XSPEC to identify and model each emission line through Gaussian profiles⁷. Error were calculated using the error tool within XSPEC. This tool determines the error ranges by sorting

Table 2. Clumpy model parameters.

Parameter	Value
Inclination	< 10. ^o
N_0	>14.8
σ	$34.8^{\circ} \pm^{0.3}_{0.4}$
Y ($R_{\text{out}}/R_{\text{in}}$)	$11.5 \pm^{0.1}_{0.1}$
q	0.14*
τ	$44.1 \pm^{1.7}_{2.1}$
norm (Clumpy)	$7.1 \pm^{0.08}_{0.03} (\times 10^{-12})$
norm (Stellar)	$3.5 \pm^{0.06}_{0.05} (\times 10^{-10})$

⁶ All data are available on the website: <https://www.clumpy.org/>

⁷ [FeIII], [NeV], [NeII], [SIII], [H19 – 7], [OIV], [SiII], [SIV]

the Monte Carlo chain values and taking a central percentage of the values corresponding to the confidence level as indicated by delta fit statistic. We computed the errors corresponding to $1-\sigma$.

Table 2 shows the best-fit parameters and Figure 1 shows the best fit to the data. We restricted the N_0 , σ , $Y(R_{\text{out}}/R_{\text{in}})$, and τ_ν . We were not able to constrain the observer viewing angle toward the torus i . The difficulty to restrict the viewing angle using only mid-infrared spectra was already noticed by Ramos Almeida et al. (2014). Our fit has a reduced chi-squared of 2.71 with 1471 degrees of freedom (null hypothesis probability zero).

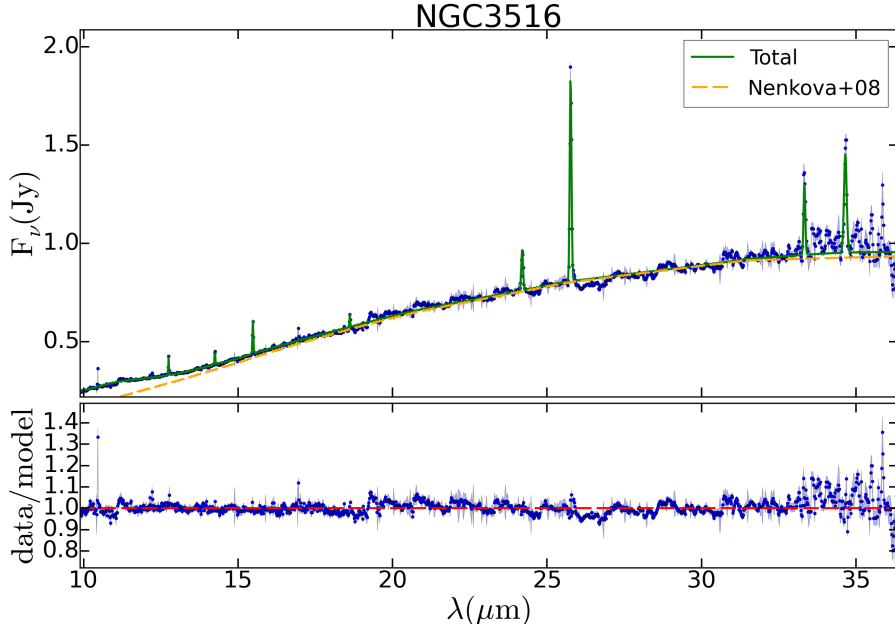


Figure 2. NGC 3516 fit spectra. Top: The green line shows the total model (Nenkova model + Stellar component + lines). The yellow line shows the Nenkova model. Bottom: The blue line shows the residuals between the data and model.

5. FITTING RESULTS FOR THE X-RAY SPECTRUM

We assumed values of $E_{\text{cut}} = 300 \text{ KeV}^8$, and $A_{Fe} = A_{Fe,\odot}$. Also, we linked the Γ and the E_{cut} from the intrinsic continuum (*cutoffpl*) to the borus02 components. Once that we had frozen these parameters and run the model, we used multi-epoch data in order to take into account the variability of the source. To find the best fit, we did four tests that consisted in freeing or freezing the normalization parameters in the borus02 and/or cutoffpl components in a data group or both. We compared the χ^2 and degrees of freedom of each one through the f-test. We found that the best fit was when we considered four normalizations - i.e., when the normalizations from borus02 and cutoffpl from each group data are free parameters (test 4 in Table 3). The resulting values of parameters from test 4 are shown in table 1.

⁸ <https://ned.ipac.caltech.edu/>

Table 3. F-test

Test	Degrees of freedom	χ^2	Comment
1	1271	2159.1	1 normalization (borus02)
2	1270	1533.2	2 normalizations (borus02 to two groups)
3	1270	2114.6	2 normalizations (borus02 and cutoffpl)
4	1268	1369.4	4 normalizations (2 borus and 2 cutoffpl)

6. MID-INFRARED AND X-RAY SIMULTANEOUS FIT

We fitted the mid-IR and X-ray spectra separately and later simultaneously. First, we fitted the *Spitzer* spectrum using the CLUMPY model. Then, we fitted the *NuStar* data using the X-ray model borus02. From these settings, we were able to constrain the N_0 , σ , Y , τ , Γ , $\log\text{NH}$, θ_{tor} , θ_i , parameters. Regarding the obtained parameters, we found that the inclination angle is consistent with an AGN type 1, as is the case of NGC 3516. For the case of the simultaneous fit we linked the following parameters: τ (CLUMPY) with $\log\text{NH}$ (Borus02) and σ (Clumpy) with θ_{tor} (Borus02). The simultaneous fit is capable of better constraining Γ , τ ($\log\text{NH}$), θ_{inc} , σ (θ_{tor}), and q parameters, as demonstrated by the test performed on the degeneration of the parameters. In table 4 we show the resulting values of this fitting.

Table 4. Borus02 and Clumpy models parameters

Parameter	Values
Γ	1.48 ± 0.01
$\log(\text{NH}_{\text{tor}})$	22.88 ± 0.03
nH (zphabs)	$< 0.4 \times 10^{22} \text{ cm}^{-2}$
Inclination	9.98°
N_0	> 14.95
σ	$35.00^\circ \pm 0.2$
$Y(\text{Rout}/\text{Rin})$	11.35 ± 0.06
q	0.03 ± 0.03

7. CONCLUSIONS AND DISCUSSION

REFERENCES

- Alonso-Herrero, A., Ramos Almeida, C., Mason, R., et al. 2011, ApJ, 736, 82
- Antonucci, R. 1993, ARA&A, 31, 473
- Baloković, M., Brightman, M., Harrison, F. A., et al. 2018, ApJ, 854, 42
- Bianchi, S., Matt, G., Balestra, I., Guainazzi, M., & Perola, G. C. 2004, A&A, 422, 65
- Brightman, M., & Nandra, K. 2011, MNRAS, 413, 1206
- Efstathiou, A., & Rowan-Robinson, M. 1995, MNRAS, 273, 649
- Elitzur, M., Nenkova, M., & Ivezić, Z. 2004, The Neutral ISM in Starburst Galaxies, 320, 242
- Elitzur, M. 2006, NewAR, 50, 728
- Elitzur, M., & Netzer, H. 2016, MNRAS, 459, 585
- Emmanoulopoulos, D., Papadakis, I. E., Epitropakis, A., et al. 2016, MNRAS, 461, 1642

Appendix D: PhD project

Original Phd project

Universidad Nacional Autónoma de México



Doctorado en Ciencias (Astrofísica)
Instituto de Radioastronomía y Astrofísica

Proyecto Doctoral

EL ENTORNO DE LOS NÚCLEOS ACTIVOS DE GALAXIAS

Presentado por
Donaji Catalina Alejandra Esparza Arredondo

Asesorada por
Dra. Omaira González Martín
&
Dra. Deborah Dultzin Kessler



8 de mayo de 2017

Índice general

1. Introducción	1
1.1. Clasificación de los AGNs	1
1.1.1. Componentes y modelos del AGN	1
1.1.2. Tipos de AGNs	2
1.2. Relación entre el AGN y la galaxia anfitriona.	2
1.3. Los AGNs en el Infrarrojo	3
1.4. Los AGNs en rayos X	3
2. Trabajo previo	5
3. Objetivos	6
3.1. Coevolución entre el AGN y la formación estelar de la galaxia anfitriona	6
3.1.1. El campo de radiación del AGN	6
3.1.2. Estudiar la formación estelar en el entorno del AGN	6
3.2. Las propiedades del toro mediante el ajuste simultáneo de espectros en rayos X y el MIR	6
4. Metodología	7
4.1. El campo de radiación del AGN	7
4.2. Estudiar la formación estelar en el entorno del AGN	7
4.3. Las propiedades del toro mediante el ajuste simultáneo de espectros en rayos X y MIR	7
5. Índice tentativo para la tesis	9
6. Cronograma	10
Bibliografía	11

Introducción

Los agujeros negros (BHs, por sus siglas en inglés) son objetos con densidades extremas cuya atracción gravitacional es tan grande que ni siquiera la luz puede escapar de ellos. La existencia de estos objetos fue propuesta desde el siglo XVIII por Laplace, y fue confirmada por Einstein a principios del siglo pasado. Pero fue en 1969 cuando se le dio el nombre de “agujero negro” por primera vez, y varios años después se dieron las pruebas observacionales de su existencia. Actualmente se han encontrado BHs de diferentes tamaños que abarcan un gran rango de masas, desde $3 - 30 M_{\odot}$, remanentes del colapso de un núcleo estelar en supernovas tipo II, hasta los conocidos como agujero negros supermasivos (SMBHs, por sus siglas en inglés) cuyas masas son del orden de $10^6 - 10^9 M_{\odot}$ y se encuentran en el centro de las galaxias. Los SMBH que tienen alrededor de ellos un disco acreciendo material hacia el mismo son conocidos como “Núcleos Activos de Galaxias” (AGNs, por sus siglas en inglés). En el Universo local ($z < 0.1$), alrededor de una de cada 50 galaxias contiene un SMBH con acreción eficiente, mientras que una de cada tres contienen un SMBH de acreción ineficiente. La energía liberada por un AGN está en el rango de $10^{38} - 10^{48} \text{ erg s}^{-1}$ y emite en todas las longitudes de onda.

La teoría sobre los AGNs explica que en la parte más interna del disco de acreción se emite radiación no térmica. Esta emisión no térmica es producida en su mayor parte por la conversión de masa (en reposo) en energía y en menor porcentaje por emisión de electrones ultra-relativistas, efecto Compton inverso, aniquilación de pares y procesos de radiación coherente de plasma [e.g. Blandford & Rees, 1992]

1.1. Clasificación de los AGNs

1.1.1. Componentes y modelos del AGN

Debido a que los AGNs son fuentes compactas no resueltas ($\sim 1 \text{ kpc}$) y en muchos casos variables, su estudio es complejo. Hoy en día pensamos que la mayoría de los AGNs tienen las siguientes componentes:

- **Disco de acreción.** Un flujo de acrecimiento dominado por rotación, el cual forma un disco ópticamente grueso que puede ser geométricamente delgado o grueso.
- **Región de líneas anchas (BLR).** Nubes de gas con alta densidad ($\sim 10^{10} \text{ cm}^{-3}$) rotando a velocidades típicas del orden de $\sim 2500 \text{ km s}^{-1}$ alrededor del disco de acreción.
- **Toro de Polvo.** Una estructura polvoriento axisimétrica con un radio entre $\sim 0.1 - 10 \text{ pc}$.
- **Región de líneas Delgadas (NLR).** Nubes de gas ionizado con baja densidad ($\sim 10^4 \text{ cm}^{-3}$). Las velocidades de dispersión típicas de las nubes son $\sim 500 \text{ km s}^{-1}$. El gas se extiende desde afuera del toro hasta cientos de kilómetros a lo largo de la dirección de apertura del toro.
- **Chorros relativistas** Chorros de material en forma de plasma eyectado desde el disco de acreción en dirección perpendicular a este.

La localización de cada parte de la estructura mencionada ha dado lugar a una serie de modelos para explicar las diferentes propiedades observacionales en los AGNs. El esquema más aceptado se conoce como modelo unificado [*Unified Model*, UM Antonucci, 1993; Urry & Padovani, 1995]. El UM propone que las diversas propiedades observacionales en los diferentes AGNs dependen sólo de algunos parámetros físicos como: 1) La posición del toro respecto a la línea de visión del observador, 2) La luminosidad de la fuente, o 3) la presencia de chorros relativistas. La Fig.1.1 muestra un esquema incluyendo las componentes del AGN de acuerdo con el UM. Sin embargo, otros modelos proponen una conexión entre los diferentes AGNs por medio de una evolución inducida por las perturbaciones del entorno más próximo por la caída del gas al núcleo [e.g. Krongold et al., 2003; Koulouridis, 2014]. Finalmente, algunos autores apuntan a que estas componentes pueden verse modificadas. Por ejemplo, el disco de acrecimiento a veces puede no existir y ser sustituido por una corona ineficiente. Otro ejemplo clásico es la desaparición del toro de polvo en AGNs de baja luminosidad [e.g. Elitzur & Netzer, 2016; González-Martín et al., 2017].

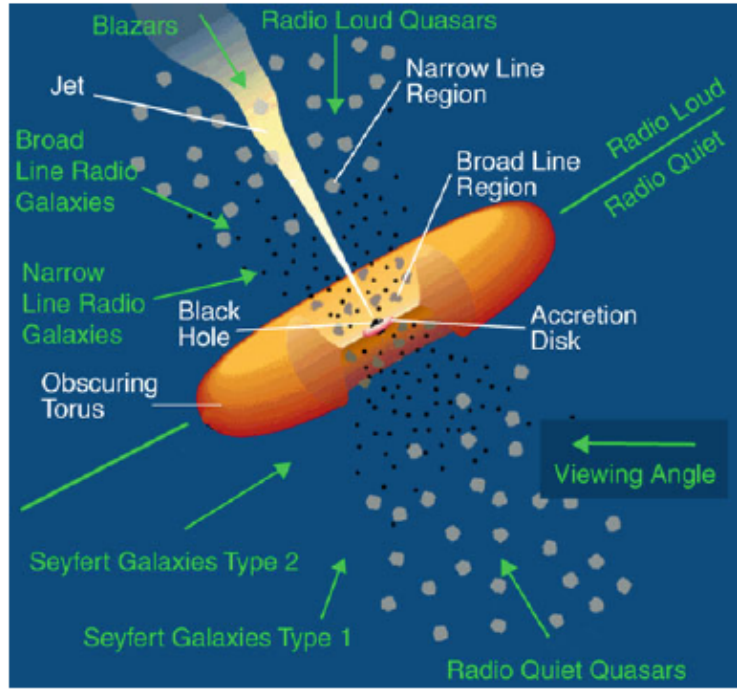


Figura 1.1: Esquema del UM presentado por Urry & Padovani [1995]. La clave de esta unificación entre AGN tipo 1 y tipo 2 reside en la existencia del toro de polvo ópticamente grueso alrededor de la fuente combinado con la orientación. Para ciertos ángulos de visión la BLR es bloqueada, escondiendo así las líneas de emisión anchas en el espectro y permitiendo tan sólo ver las propiedades físicas de la región más alejada del AGN como es la NLR. En este caso, observationalmente el objeto se clasifica como un AGN de tipo 2. Si el toro de polvo no obstaculiza la línea de visión entre fuente y observador se puede apreciar la NLR y BLR, clasificando así el AGN como tipo 1. Credito: NASA.

1.1.2. Tipos de AGNs

Hoy en día, sabemos que existen muchos tipos de AGNs, pero este trabajo se centrará solamente en los siguientes dos grupos:

- **AGN tipo I** Estas fuentes muestran líneas de emisión anchas ($1,000 - 20,000 \text{ km s}^{-1}$) permitidas y semiprohibidas. Casi todos los AGNs tipo I de baja e intermedia luminosidad, muestran fuertes líneas de emisión angostas ($300 - 1,000 \text{ km s}^{-1}$) de alta ionización muchas de las cuales son prohibidas. Estos AGNs son conocidos como Seyfert tipo I (Sy1) o QSOs.
- **AGNs tipo II** Estas fuentes contienen fuertes líneas de emisión angostas ($300 - 1,000 \text{ km s}^{-1}$) en el cercano infrarrojo-óptico-UV. Dichas líneas son más amplias que las observadas en galaxias con líneas de emisión. Las líneas muestran claras indicaciones de fotoionización por una fuente no estelar. Estos AGNs son conocidos como Seyfert tipo II (Sy2).

1.2. Relación entre el AGN y la galaxia anfitriona.

El estudio de la relación entre el AGN y la galaxia anfitriona ha sido un campo muy activo en las últimas décadas [Magorrian et al., 1998; Ferrarese & Merritt, 2000; Kormendy & Ho, 2013]. Algunos estudios han encontrado, por ejemplo, una correlación entre las masas del SMBH y el bulbo de la galaxia. Para explicar estas y otras relaciones se han propuestos diversos escenarios. Algunos autores han propuesto que el gas alrededor del centro de la galaxia es el responsable del crecimiento del SMBH y del enriquecimiento de la formación estelar [Sanders & Mirabel, 1996] También se ha sugerido que el apagado de la formación estelar (SF) podría estar relacionado con la retroalimentación del SMBH [Silk & Rees, 1998]. Las simulaciones numéricas proponen un escenario donde los procesos a gran escala pueden estar relacionados con los fenómenos a menor escala [Hopkins and Quataert , 2010; Netzer, 2013]. De acuerdo con estos estudios, las fusiones mayores o las mareas producen perturbaciones que puede estar relacionadas con la acreción del SMBH y la SF. Otros autores proponen un escenario donde el campo radiación de la fuente central es capaz de detener la SF, imponiendo un balance entre ambos [e.g. Wu et al. , 2009].

Estudiar la SF circunuclear en los AGNs es importante pues puede darnos importantes pistas sobre la relación entre la actividad del núcleo y la galaxia anfitriona. Sin embargo, no es trivial porque los trazadores clásicos de SF pueden estar contaminados por la propia emisión del AGN. En este trabajo de tesis ahondaremos en el estudio de estos trazadores con el objetivo de profundizar en los mecanismos de coevolución entre AGN y la SF de las galaxias anfitrionas.

1.3. Los AGNs en el Infrarrojo

En longitudes de onda del mediano infrarrojo (MIR, por sus siglas en inglés) se pueden analizar líneas de emisión que proceden tanto del AGN como de la SF nuclear de la galaxia anfitriona. Particularmente, para el caso de trazar la SF se utilizan las emisiones debidas a los Hidrocarburos Aromáticos Policíclicos (PAHs, por sus siglas en inglés). Los PAHs son moléculas, de entre 20-100 átomos de carbono e hidrógeno, calentadas a altas temperaturas debido a estrellas jóvenes tipo B.

La emisión de PAHs ha sido observada en la región nuclear y circunuclear de los AGNs [González-Martín et al., 2013; Alonso-Herrero et al., 2014]. Diamond-Stanic et al. [2010] encontraron una fuerte correlación de la SF nuclear en escala de kpc usando el PAH de $11.3\mu\text{m}$ y el continuo a $24\mu\text{m}$ para galaxias Seyfert. La emisión de PAHs es débil o ausente en fuentes tipo Sy1 [e.g. Mason et al., 2007]. Estos autores han relacionado la ausencia de PAHs con la destrucción o ionización de las moléculas responsables de esta emisión por el campo de radiación del AGN.

La mayor parte de estos trabajos se basan en la comparación de SF nuclear y circunuclear, utilizando el espectro nuclear de telescopios terrestres (es decir, con la mejor resolución espacial posible) y el espectro circunuclear de satélites [es decir, con menor resolución espacial, e.g. Esquej et al., 2014]. Sólo algunos estudios hacen un análisis detallado de la emisión circunuclear utilizando distintas aperturas radiales centradas en el núcleo activo para unos pocos objetos [e.g. Alonso-Herrero et al., 2014].

Otra línea observada en el rango del MIR es el [SIV] a $10.5\mu\text{m}$, esta emisión surge de iones con un potencial de excitación de 35 eV. Ésta ha sido observada en un gran número de objetos como son las nebulosas planetarias, regiones HII galácticas y ULIRGs [Gillett et al., 1972].

El origen de la línea de [SIV] en los núcleos activos es controvertido, apuntando a que puede producirse por regiones de SF y/o fotoionización por el AGN [Pereira-Santalla et al., 2010; Groves et al., 2008]. Además, la emisión en continuo en el mediano MIR está dominada por el polvo calentado por el AGN. Así, se puede estudiar las propiedades del toroide de polvo de los AGNs modelando este continuo con códigos de transferencia radiativa [Nenkova et al., 2008; Hönig, 2008; Ramos Almeida et al., 2009, 2014]. Estos modelos asumen un toro grumoso (es decir, no homogéneo) cuyos parámetros son el grosor, el número de nubes en el plano ecuatorial del toro, el perfil de densidad dependiente del radio, el radio externo, la profundidad óptica de las nubes, ángulo de inclinación, etc.

1.4. Los AGNs en rayos X

Los rayos X son también un rangopectral donde hay importantes pistas de las componentes de los AGNs. Específicamente, en estas longitudes de onda existen ciertas características que pueden ayudar a diagnosticar las propiedades del toroide [Bassani et al., 1999; Panessa et al., 2006; González-Martín et al., 2009], que serán de especial interés para este trabajo. Estas particularidades son las siguientes:

- Una componente cuyo pico se encuentra aproximadamente a 20 KeV debido a la baja dispersión de los fotones en rayos X duros. En concreto, esta componente se produce por el reprocesado de emisión del disco en una corona íntimamente ligada al mismo y que emite por Compton inverso en rayos X duros. Esta componente es conocida como **la joroba Compton** (en inglés *Compton hump*) o componente intrínseca.
- La segunda característica es debida a la reflexión de los electrones en el gas altamente ionizado. La radiación reflejada es una imagen del continuo intrínseco, que depende únicamente del factor de cobertura geométrico ($f_c = \Omega/4\pi$, donde Ω es el ángulo sólido subtendido por el material reflector). En cuanto al origen del material reflector existen dos hipótesis. En la primera este material reflector es el propio disco de acrecimiento. En este caso se espera que la componente de reflexión obedezca a cambios en el continuo del AGN rápidamente. En el segundo caso este material reflector es el toro. Debido a la lejanía del toroide en estos casos no esperamos cambios a corto plazo en la componente de reflexión.
- La tercera componente es la emisión de la línea de hierro neutra a 6.4 KeV (F_{K_α}). Esta emisión está asociada a la componente reflejada. De este modo estas líneas son anchas y de alta ionización si se originan en la superficie del disco de acreción central, o serán delgadas y ocasionalmente de baja ionización si se originan debido a la iluminación de rayos X del gas frío en el toro. Sólo se han detectado unos pocos

casos de líneas de hierro neutro anchas. En el caso donde el continuo en rayos X no es oscurecido el ancho equivalente (EW, por sus siglas en inglés) de la línea angosta de K_{α} depende del número de fotones absorbidos. El $EW(K_{\alpha})$ depende del factor de cobertura y la densidad columnal de hidrógeno. Por lo tanto, el EW de esta emisión es una firma clara de la existencia o no del toro central en los AGNs [Guainazzi et al., 2005]. En una fuente muy oscurecida se esperan anchos EW grandes, pues la línea llega al observador, pero la mayor parte de la radiación del continuo central es bloqueada por el toro [Ghisellini et al., 1994].

Actualmente, existen diferentes modelos para poder reproducir las componentes de toro en rayos X [por ejemplo, ComPS y mytorus incluidos en el software de ajuste espectral Xspec Jordan et al., 1994]. Estos modelos consideran diferentes parámetros como: temperaturas, profundidad óptica, ángulo de inclinación, etc. En la figura 1.2 se muestra el espectro de un AGN en rayos X y se especifica la contribución de cada una de estas características.

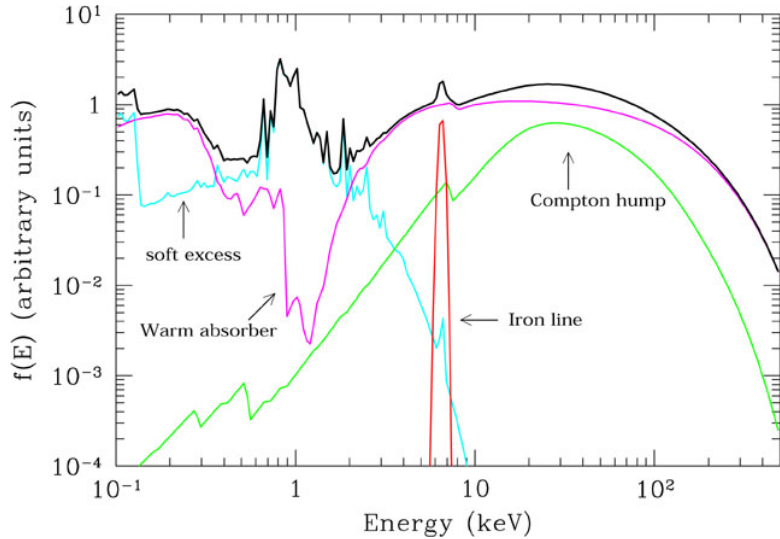


Figura 1.2: Espectro con las componentes en rayos X de un AGN.

Trabajo previo

Durante la maestría se exploró la relación entre la SF circunuclear y la actividad del AGN. Para esto utilizamos una muestra de 19 AGNs locales con alta resolución espacial usando espectros de rendija larga de T-ReCS, CanariCam y *Spitzer*. En este trabajo se usó el PAH en $11.3 \mu\text{m}$ como trazador de SF y la línea de [SIV] a $10.5 \mu\text{m}$ como trazador del campo de radiación del AGN. En este trabajo se exploraron las emisiones de ambas líneas a diferentes distancias del núcleo, usando distintas aperturas (véase Fig.2.1).

Especificamente, encontramos que la línea de [SIV] puede ser un buen trazador de la luminosidad del AGN en los casos donde el núcleo se encuentra aislado de la galaxia anfitriona. A escala mayores consideramos la posibilidad de que la emisión de [SIV] puede estar contaminada por SF. Descartamos que la SF trazada por el PAH en $11.3 \mu\text{m}$ fuera la misma que contamina al [SIV] a estas escalas. Por otro lado, exploramos la relación propuesta por los diferentes modelos teóricos entre tasa de formación estelar (SFR, por sus siglas en inglés) y la luminosidad del AGN a diferentes distancias del núcleo [Ruschel-Dutra et al., 2017]. Utilizamos la luminosidad del PAH en $11.3 \mu\text{m}$ para calcular SFR siguiendo la relación propuesta por Shipley et al. [2016]. Encontramos que nuestros datos y los modelos de coevolución están en un buen acuerdo para distancias $\geq 50 \text{ pc}$. Sin embargo, a escalas menores encontramos que existe un déficit de PAHs, que podría estar relacionado con la posible destrucción de las moléculas por el campo de radiación del AGN [Diaz-Santos et al., 2010]. Estos resultados están próximos a enviarse para su publicación.

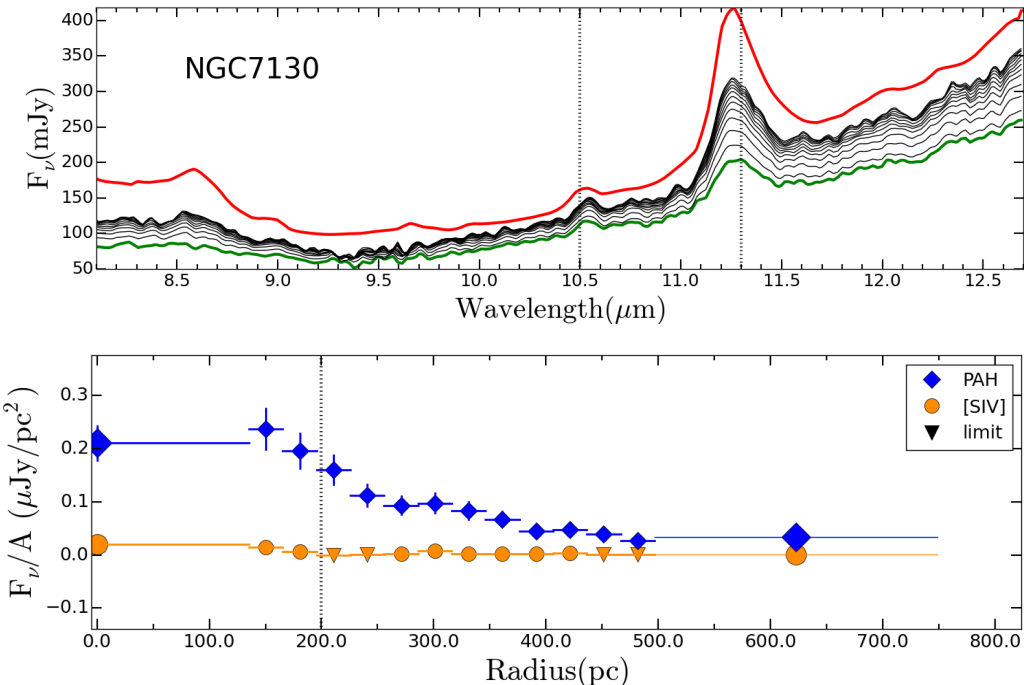


Figura 2.1: (Superior): Espectros extraídos a diferentes distancias del núcleo para NGC 7130. La línea roja representa al espectro obtenido por *Spitzer*, la línea verde es el espectro nuclear y las líneas en negro corresponden a los espectros extraídos a diferentes aperturas por T-ReCs/Gemini. Las líneas punteadas muestran la localización del PAH estudiado y la línea de [SIV]. (Inferior): Perfiles de brillo superficial para NGC 7130. Los perfiles radiales del PAH y el [SIV] se muestran con diamantes azules y círculos naranjas, respectivamente. Los símbolos más grandes (diamantes o círculos) corresponden a las mediciones en los espectros nucleares y de *Spitzer*, respectivamente. El resto de los símbolos representan las mediciones en los espectros a diferentes aperturas. La línea punteada señala una distancia de 200 pc del núcleo. Los triángulos representan valores límite.

Objetivos

Esta tesis estará dividida en dos grandes bloques. Para la primera parte del trabajo continuaremos con la investigación acerca de la coevolución entre la SF y la actividad nuclear, que hemos presentado en el trabajo previo. La ventaja del trabajo que proponemos consiste en que podremos explorar la distribución de brotes de SF y/o fotoionización nuclear usando imágenes de alta resolución espacial. Actualmente, solamente disponemos de espectros de rendija larga. El segundo bloque de este trabajo consistirá en estudiar el toro del AGN a través de códigos para generar modelos de SED haciendo ajustes simultáneos de espectros en el MIR y rayos X.

3.1. Coevolución entre el AGN y la formación estelar de la galaxia anfitriona

3.1.1. El campo de radiación del AGN

En el trabajo previo encontramos que la línea de [SIV] puede utilizarse como trazadora de fotoionización del AGN hasta ciertas escalas. Sin embargo, no es claro el grado de contaminación por SF. Por lo tanto, nuestro primer objetivo será estudiar el comportamiento de esta línea junto al de otras líneas que sabemos trazan fotoionización nuclear (por ejemplo, [OIII] a 5700 Å). Nótese que para esto contamos con imágenes de alta resolución en los archivos de CanariCam, T-ReCS y *Spitzer* para el MIR. Además, existen datos disponibles del telescopio espacial Hubble (HST, por sus siglas en inglés).

3.1.2. Estudiar la formación estelar en el entorno del AGN

En nuestro trabajo anterior estudiamos la coevolución entre AGN y SFR circunuclear por medio del PAH en $11.3\ \mu\text{m}$. Sin embargo, no logramos clarificar si los PAHs eran buenos trazadores de SF cerca del AGN ($< 50\ \text{pc}$). Además, en muchas de nuestras fuentes no existen registros de SF por medio de otros trazadores. Por lo tanto, nuestro segundo objetivo es explorar que tan buen trazador de formación estelar puede ser el PAH en $11.3\ \mu\text{m}$ ante la presencia de un AGN. Para esto combinaremos imágenes de alta resolución de MIR y óptico. Las imágenes se encuentran disponibles en archivo de los mismos telescopios mencionados para el [SIV].

3.2. Las propiedades del toro mediante el ajuste simultáneo de espectros en rayos X y el MIR

En trabajos previos se han presentado modelos de toros usando códigos de transferencia radiativa para estimar las propiedades en el MIR [Nenkova et al., 2008; Höning & Kishimoto, 2010] y rayos X [e.g. mytorus¹ Murphy & Yaqoob, 2009]. Sin embargo, no se han logrado restringir correctamente los parámetros del toro [Ramos Almeida et al., 2014]. Por lo tanto, nuestro último objetivo consistirá en obtener por primera vez una buena estimación de los parámetros para modelar las componentes del toro de polvo. Para ello combinaremos por primera vez los espectros en rayos X con los espectros en el MIR, con lo cual realizaremos un ajuste simultáneo. Esto nos permitirá a estudiar si el toro tiene propiedades distintas dependiendo del tipo de actividad del AGN.

¹<http://mytorus.com/>

Metodología

4.1. El campo de radiación del AGN

Para analizar la emisión de [SIV] crearemos una muestra de AGNs locales. Nuestra selección se basará en las observaciones disponibles en archivo de CanariCam, T-ReCS y el catálogo de [Asmus et al., 2014]. Este catálogo contiene observaciones en diferentes filtros e instrumentos de telescopios terrestres en el MIR. Una vez seleccionada la muestra, desarrollaremos un método capaz de aislar la línea de [SIV] usando imágenes del continuo para su sustracción. Para esto utilizaremos algunas rutinas de python como lo son astropy, scipy, numpy, entre otras. Con las imágenes resultantes se creará un catálogo. Las imágenes de este catálogo serán analizadas e interpretadas como trazadores de fotoionización nuclear, siguiendo los resultados propuestos por Groves et al. [2008].

Para continuar el estudio del [SIV], descargaremos las imágenes disponibles en óptico del HST de las fuentes del catálogo. Buscaremos que las imágenes seleccionadas contengan algún trazador de fotoionización nuclear (e.g. [OIII] a 5007 Å). Es importante mencionar, que hemos hecho una búsqueda preliminar en el archivo del HST y consideramos que la mayoría de los datos están disponibles. Después de reducir las imágenes en óptico, graficaremos sobre cada imagen los contornos en MIR correspondientes a cada fuente. Debido a que los rayos X pueden ser un buen trazador del campo de radiación del AGN, también consideramos la posibilidad de combinar las imágenes en óptico y/o MIR con las disponibles para esta longitud de onda. Es decir, podemos tener imágenes en el óptico que compararemos tanto con los rayos X como con el MIR. Este proceso nos permitirá saber si el [SIV] es tan buen trazador del campo de radiación como el [OIII] y los rayos X. En caso de que el [SIV] se encuentre trazando SF, esperamos que la combinación con imágenes en óptico y/o UV nos clarifique la edad de las estrellas que traza.

4.2. Estudiar la formación estelar en el entorno del AGN

Esta parte del trabajo comenzará con la selección de una muestra de AGNs con observaciones disponibles en archivo en la banda del PAH en $11.3\text{ }\mu\text{m}$. La instrumentación de esta parte del trabajo es esencialmente la misma que en el apartado anterior. Igualmente emplearemos el método desarrollado en el análisis del [SIV] para crear imágenes de PAHs descontaminadas del continuo subyacente. Este tipo de metodología ha sido ya probada para el caso de los PAHs en el trabajo de Ruschel-Dutra et al. [2017] para unos pocos AGNs locales. Dicho trabajo se centra en estimar la SFR nuclear a través de imágenes. Nosotros extenderemos el método a una muestra mucho más grande y explotaremos la morfología extendida. Crearemos un catálogo con las imágenes resultantes después de aplicar este método.

Buscaremos las imágenes de las fuentes de nuestro catálogo entre los archivos del HST (óptico y UV), pues en esta longitud de onda existen diferentes trazadores de formación estelar (e.g. $\text{H}\alpha$). Reduciendo estos datos, procesaremos nuestras imágenes de MIR y UV para crear mapas de contorno que graficaremos sobre las imágenes en óptico de cada fuente. Estos nos permitirán confirmar si las emisiones del PAH corresponden a regiones de formación estelar. Incluso podría ayudarnos a ubicar regiones de SF circunucleares no consideradas en trabajos previos.

4.3. Las propiedades del toro mediante el ajuste simultáneo de espectros en rayos X y MIR

El trabajo partirá creando un código a partir de los disponibles (e.g. mytorus, Xspec), para hacer un ajuste simultáneo de los parámetros del toro en MIR y rayos X. Como se mencionó en la introducción en el MIR y en rayos X existen modelos que permiten estimar las propiedades del toro en ambas longitudes. Utilizaremos el software Xspec el cual permite ajustar datos de múltiples satélites de rayos X a una gran variedad de modelos.

Los datos en rayos X deben ajustarse con este software (a uno similar conocido como Sherpa), porque se necesita incluir en el ajuste las matrices de respuesta de los instrumentos. Para este trabajo pretendemos hacer un ajuste simultáneo de datos en MIR y rayos X. Para esto necesitamos convertir el espectro del MIR y el modelo de toro de polvo del código de transferencia radiativa a un lenguaje que pueda ser manipulado por Xspec.

La ventaja de unir rayos X y MIR es que existen parámetros en cada modelo que coinciden (e.g. absorción en la línea de visión, ángulo de inclinación del toro y los flujos integrados). Por lo tanto, esperamos que este código nos ayude a mejorar la degeneración entre los parámetros del toro. Una vez finalizado dicho código seleccionaremos un objeto prueba con suficientes observaciones en tanto de MIR como rayos X. Los archivos de *Chandra*, *XMM-Newton*, *NuSTAR*, CanariCam/GTC y *Spitzer* disponen de muchas observaciones para un gran número (miles) de AGNs. Existen observaciones simultáneas al menos para 100 objetos publicados recientemente por [Gonzalez-Martin et al., 2015b]. Así las observaciones están garantizadas para esta parte del proyecto. Para comprobar la funcionalidad de nuestro código realizaremos tres pruebas: 1) Ajustaremos los datos y el modelo obtenido a partir de usar solamente el código en rayos X, 2) Ajustaremos los datos y el modelo obtenido solo para el caso de considerar MIR, y 3) Ajustaremos datos y nuestro modelo (el cual hace un ajuste simultáneo de ambas longitudes de onda). Con estas tres pruebas concluiremos si el ajuste simultáneo mejora nuestra estimación de los parámetros, cuantificar cuales mejoran y cuanta es la mejoría usando técnicas estadísticas como ftest, chi2, cstat, etc.

La siguiente fase de nuestro trabajo consistirá en crear una muestra de AGNs locales, cuyos datos de MIR se encuentren disponibles en el catálogo de CASSIS/*Spitzer* y del grupo Piratas (CanariCam/GTC y T-ReCS). Conjuntamente también se buscarán que los datos estén disponibles para rayos X en los telescopios mencionados en el párrafo anterior. Utilizaremos la muestra para hacer una estimación de los parámetros para modelar las componentes del toro de polvo a partir de introducir las fuentes en nuestro código. El objetivo final es estudiar si el toro cambia con los parámetros del AGN, tales como la dureza de la SED, la tasa de acrecimiento, la masa del agujero negro, o la luminosidad bolométrica.

Índice tentativo para la tesis

* Capítulo 1: Introducción

- Los AGNs y sus propiedades a diferentes longitudes de onda
- El AGN y su galaxia anfitriona
- Justificación

* Capítulo 2: Coevolución usando espectros desde tierra en el MIR.

* Capítulo 3: Coevolución usando imágenes de alta resolución

- Selección de la muestra
- Reducción de datos
- Análisis de los datos
- Resultados
- Discusión

* Capítulo 4: Propiedades del toro en MIR y rayos X.

- Selección de la muestra
- Reducción de datos
- Código de ajuste simultáneo para imágenes en rayos X y MIR.
- Análisis de datos
- Resultados
- Discusión

* Capítulo 5: Conclusiones

* Capítulo 6: Trabajo a futuro

Cronograma

A continuación, presentamos un cronograma con el trabajo a realizar en cada semestre del doctorado. Como se puede observar hemos especificado al final de cada línea el objetivo involucrado: 1) Estudiar el campo de radiación del AGN a través del [SIV], 2) Estudiar la SF circunuclear o 3) Estudiar las propiedades del toro en MIR y rayos X.

■ Primer semestre

- ★ Definir los temas a tratar durante el doctorado. Para esto se hará un repaso de la literatura reciente en el campo de los AGNs a diferentes longitudes de onda.
- ★ Seleccionar una muestra de AGNs locales para estudiar la emisión de [SIV], basándonos en los datos disponibles de los archivos de CanariCam, T-ReCs y el catálogo de Asmus et al. [2014] (*Objetivo 1*).
- ★ Buscar una colaboración con investigadores expertos en la emisión de [SIV] como lo son: 1) Dr. Michael Dopita, 2) Dr. Brent Groves y la Dra. Elisabete da Cunha (*Objetivo 1*).
- ★ Corregir y enviar el artículo con el trabajo previo mencionado en la sección 2. El texto se encontraba totalmente redactado, pero falta añadir los comentarios de los coautores antes de enviar a la revista.
- ★ Presentar trabajo previo en congreso: Multi-scale star formation.
- ★ Preparar el proyecto para el doctorado.

■ Segundo semestre

- ★ Desarrollar un código capaz de aislar la línea de [SIV] y la emisión de PAH usando imágenes del continuo (*Objetivo 1 y 2*).
- ★ Crear un catálogo a partir de la muestra seleccionada de AGNs para el [SIV] y procesadas con el código de sustracción del continuo (*Objetivo 1*).
- ★ Analizar e interpretar las imágenes de [SIV] de nuestro catálogo siguiendo los resultados propuestos por Groves et al. [2008] (*Objetivo 1*).
- ★ Descargar las imágenes en óptico del HST de las fuentes de nuestro catálogo (*Objetivo 1*).
- ★ Combinar imágenes en óptico con las disponibles en MIR y rayos X (*Objetivo 1*).
- ★ Analizar los resultados obtenidos y redactar artículo sobre el campo de radiación del AGN (*Objetivo 1*).
- ★ Crear un código para integrar los espectros en MIR en el código Xspec de rayos X. Con esto se podrán hacer ajustes simultáneos de parámetros en rayos X y MIR para el toro de polvo en AGNs (*Objetivo 3*).
- ★ Responder el arbitraje del artículo enviado el semestre anterior.

■ Tercer semestre

- ★ Revisar y enviar el artículo sobre los resultados del campo de radiación del AGN (*Objetivo 1*).
- ★ Seleccionar una muestra de AGNs con imágenes disponibles en el óptico y MIR (*Objetivo 2*).
- ★ Descargar y reducir los datos de la muestra (*Objetivo 2*).
- ★ Aislar la emisión del PAH en $11.3 \mu\text{m}$ usando el mismo código que para el [SIV] (*Objetivo 2*).
- ★ Combinar imágenes en óptico con las disponibles en MIR y rayos X para el PAH (*Objetivo 2*).
- ★ Analizar los resultados obtenidos y redactar artículo sobre la SF usando como trazador el PAH (*Objetivo 2*).
- ★ Hacer el estudio piloto del código de ajuste simultáneo creado el semestre anterior (*Objetivo 3*).

- ★ Presentar la candidatura.

■ Cuarto semestre

- ★ Responder el arbitraje sobre los resultados del campo de radiación del AGN (*Objetivo 1*).
- ★ Revisar y enviar artículo sobre la SF usando como trazador el PAH (*Objetivo 2*).
- ★ Crear una muestra con datos en MIR y rayos X para el análisis del toro (*Objetivo 3*).
- ★ Descargar y reducir los datos en MIR y rayos X para la muestra seleccionada (*Objetivo 3*).
- ★ Presentar en un congreso internacional los resultados obtenidos hasta el momento.

■ Quinto semestre

- ★ Utilizar la muestra creada el semestre anterior para parametrizar las propiedades del toro utilizando el código desarrollado de ajuste simultáneo (*Objetivo 3*).
- ★ Estancia en el IAC con la Dra. Cristina Ramos Almeida. La estancia servirá para aprender sobre la física detrás del toro de polvo en los AGNs (*Objetivo 3*).
- ★ Responder el arbitraje del artículo sobre la SF usando como trazador el PAH (*Objetivo 2*).
- ★ Comenzar a redactar la tesis doctoral.

Nótese que llegado a este punto esperamos que gran parte de la tesis esté ya escrita en publicaciones científicas, de manera que la redacción de la tesis tomará poco tiempo.

■ Sexto semestre

- ★ Análisis de resultados obtenidos sobre las componentes del toro (*Objetivo 3*).
- ★ Redactar y revisar el artículo correspondiente donde presentemos los resultados sobre las propiedades del toro (*Objetivo 3*).
- ★ Añadir los resultados obtenidos a la tesis doctoral.

■ Séptimo semestre

- ★ Redacción final de la tesis doctoral.
- ★ Asistir a un congreso internacional para mostrar los resultados obtenidos sobre el toro del polvo en AGNs.
- ★ Revisar y enviar tercer artículo sobre propiedades del toro de polvo en rayos X y MIR (*Objetivo 3*).

■ Octavo semestre

- ★ Responder arbitraje del artículo sobre propiedades del toro de polvo en rayos X y MIR (*Objetivo 3*).
- ★ Resolver trámites burocráticos.
- ★ Defensa correspondiente del grado.

Guía de tiempos del proyecto

En la tabla 6.1 se muestra una estimación del tiempo dedicado a cada uno de los objetivos propuestos: 1) Estudiar el campo de radiación del AGN, 2) Estudiar la SF circunuclear o 3) Estudiar las propiedades del toro en MIR y rayos X. Además, en la fila llamada **otros** consideramos los tiempos invertidos para preparar trabajos en congresos, preparar candidatura, escritura de tesis, resolver burocracia, etc. Las estrellas en naranja representan el tiempo dedicado a preparar el proyecto de doctorado (1 semestre) o la candidatura (3 semestre) y las estrellas en rojo representan los tiempos dedicados a preparar y presentar la tesis (7 y 8 semestre).

	S1	S2	S3	S4	S5	S6	S7	S8
Objetivo 1	★★★	★★★	*	*				
Objetivo 2	*	*	★★★	★★	★★			
Objetivo 3		*	*	★★	★★★	★★★	★★	*
Otros	★*	*	*	*	*	★*	★★★	★★★★

Tabla 6.1: Guía de tiempos del proyecto. Cada estrella representa un mes.

Bibliography

- Alonso-Herrero, A., Ramos Almeida, C., Esquej, P., et al. 2014, MNRAS, 443, 2766
- Antonucci, R. 1993, ARA&A, 31, 473
- Asmus, D., Höning, S. F., Gandhi, P., Smette, A., & Duschl, W. J. 2014, MNRAS, 439, 1648
- Baldwin, J. A., Phillips, M. M., & Terlevich, R. 1981, PASP, 93, 5
- Baloković, M., Brightman, M., Harrison, F. A., et al. 2018, ApJ, 854, 42
- Bassani, L., Dadina, M., Maiolino, R., et al. 1999, ApJS, 121, 473
- Brightman, M., & Nandra, K. 2011, MNRAS, 413, 1206
- Brightman, M., Baloković, M., Stern, D., et al. 2015, ApJ, 805, 41
- Diamond-Stanic, A.M., Rieke, G.H. 2010, ApJ, 724, 140
- Dopita, M. A., Shastri, P., Davies, R., et al. 2015, ApJS, 217, 12
- Elitzur, M., Nenkova, M., & Ivezić, Z. 2004, The Neutral ISM in Starburst Galaxies, 320, 242
- Elitzur, M., & Shlosman, I. 2006, ApJ, 648, L101
- Elitzur, M., & Netzer, H. 2016, MNRAS, 459, 585
- Esparza-Arredondo, D., González-Martín, O., Dultzin, D., et al. 2018, ApJ, 859, 124
- Esquej, P., Alonso-Herrero, A., González-Martín, O., et al. 2014, ApJ, 780, 86
- Ferrarese, L., & Merritt, D. 2000, ApJ, 539, L9
- Feltre, A., Hatziminaoglou, E., Fritz, J., & Franceschini, A. 2012, MNRAS, 426, 120
- Fritz, J., Franceschini, A., & Hatziminaoglou, E. 2006, MNRAS, 366, 767
- Ghisellini, G., Haardt, F., & Matt, G. 1994, MNRAS, 267, 743
- Gillett, F. C., Merrill, K. M., & Stein, W. A. 1972, ApJ, 172, 367
- González-Martín, O., Masegosa, J., Márquez, I., Guainazzi, M., & Jiménez-Bailón, E. 2009, A&A, 506, 1107
- González-Martín, O., Rodríguez-Espinosa, J. M., Díaz-Santos, T., et al. 2013, A&A, 553, A35
- Gonzalez-Martin, O., Masegosa, J., Marquez, I., et al. 2015, VizieR Online Data Catalog, 357,
- González-Martín, O., Masegosa, J., Hernán-Caballero, A., et al. 2017, arXiv:1704.06739
- Groves, B., Nefs, B., & Brandl, B. 2008, MNRAS, 391, L113
- Guainazzi, M., Matt, G., & Perola, G. C. 2005, A&A, 444, 119
- Haardt, F., & Maraschi, L. 1991, ApJ, 380, L51
- Holtz, J. Z., Geballe, T. R., & Rank, D. M. 1971, ApJ, 164, L29
- Höning, S. F. 2008, Ph.D. Thesis,
- Höning, S. F., Kishimoto, M., Gandhi, P., et al. 2010, A&A, 515, A23

- Hönig, S. F., & Kishimoto, M. 2010, A&A, 523, A27
- Hönig, S. F., & Kishimoto, M. 2017, ApJ, 838, L20
- Hopkins, P. F. and Quataert, E., 2010 , MNRAS, 407, 1529
- Ikeda, S., Awaki, H., & Terashima, Y. 2009, ApJ, 692, 608
- Jensen, J. J., Hönig, S. F., Rakshit, S., et al. 2017, MNRAS, 470, 3071
- Kauffmann, G., Heckman, T. M., Tremonti, C., et al. 2003, MNRAS, 346, 1055
- Kewley, L. J., Dopita, M. A., Sutherland, R. S., Heisler, C. A., & Trevena, J. 2001, ApJ, 556, 121
- Kewley, L. J., & Dopita, M. A. 2002, ApJS, 142, 35
- Kewley, L. J., Groves, B., Kauffmann, G., & Heckman, T. 2006, MNRAS, 372, 961
- Kewley, L. J., Maier, C., Yabe, K., et al. 2013, ApJ, 774, L10
- Kormendy, J., & Ho, L. C. 2013, ARA&A, 51, 511
- Krongold, Y., Dultzin-Hacyan, D., & Marziani, P. 2003, Active Galactic Nuclei: From Central Engine to Host Galaxy, 290, 523
- Koulouridis, E. 2014, A&A, 570, A72
- Magorrian, J., Tremaine, S., Richstone, D., et al. 1998, AJ, 115, 2285
- Liu, Y., & Li, X. 2015, MNRAS, 448, L53
- Marinucci, A., Matt, G., Bianchi, S., et al. 2015, MNRAS, 447, 160
- Mason, R. E., Levenson, N. A., Packham, C., et al. 2007, The Central Engine of Active Galactic Nuclei, 373, 493
- Martínez-Paredes, M., Arétxaga, I., Alonso-Herrero, A., et al. 2017, MNRAS, 468, 2
- Murphy, K. D., & Yaqoob, T. 2009, MNRAS, 397, 1549
- Nenkova, M., Ivezić, Ž., & Elitzur, M. 2002, ApJ, 570, L9
- Nenkova, M., Sirocky, M. M., Ivezić, Ž., & Elitzur, M. 2008, ApJ, 685, 147-159
- Nenkova, M., Sirocky, M. M., Nikutta, R., Ivezić, Ž., & Elitzur, M. 2008, ApJ, 685, 160-180
- Netzer, H. 2013, The Physics and Evolution of Active Galactic Nuclei, by Hagai Netzer, Cambridge, UK: Cambridge University Press, 2013
- Panessa, F., Bassani, L., Cappi, M., et al. 2006, A&A, 455, 173
- Peeters, E., Spoon, H. W. W., & Tielens, A. G. G. M. 2004, ApJ, 613, 986
- Pereira-Santaella, M., Alonso-Herrero, A., Rieke, G. H., et al. 2010, ApJS, 188, 447
- Prieto, M. A., Pérez García, A. M., & Rodríguez Espinosa, J. M. 2001, A&A, 377, 60
- Ramos Almeida, C., Levenson, N. A., Rodríguez Espinosa, J. M., et al. 2009, ApJ, 702, 1127
- Ramos Almeida, C., Alonso-Herrero, A., Levenson, N. A., et al. 2014, MNRAS, 439, 3847
- Rank, D. M., Holtz, J. Z., Geballe, T. R., & Townes, C. H. 1970, ApJ, 161, L185
- Thomas, A. D., Dopita, M. A., Shastri, P., et al. 2017, ApJS, 232, 11
- Sanders, D. B., & Mirabel, I. F. 1996, ARA&A, 34, 749
- Siebenmorgen, R., Heymann, F., & Efstathiou, A. 2015, A&A, 583, A120
- Silk, J., & Rees, M. J. 1998, A&A, 331, L1
- Stalevski, M., Fritz, J., Baes, M., Nakos, T., & Popović, L. Č. 2012, MNRAS, 420, 2756
- Veilleux, S., & Osterbrock, D. E. 1987, ApJS, 63, 295
- Urry, C. M., & Padovani, P. 1995, PASP, 107, 803
- Wu, Y., Charmandaris, V., Huang, J., et al. 2009 , ApJ, 701, 658